Assessment and Improvement of Zonal Grey Area Mitigation Methods

Towards a faster RANS-to-LES transition

Elrawy Soliman

Assessment and Improvement of Zonal Grey Area Mitigation Methods

Towards a faster RANS-to-LES transition

by

Elrawy Soliman

to obtain the degree of Master of Science
at the Delft University of Technology,
to be defended publicly on Monday March 13, 2023 at 12:30 PM.

Student number:	4684443	
Project duration:	July 15, 2022 – March 13, 2023	
Thesis committee:	Dr. S. J. Hulshoff,	TU Delft, supervisor
	Dr. A. Probst,	DLR, supervisor
	Prof. Dr. S. Hickel,	TU Delft
	Dr. D. Allaerts,	TU Delft

TU Delft

Acknowledgements

I would like to convey my appreciation to Dr.Axel Probst and Dr.Steven Hulshoff for their commitment and assistance during this thesis project. I am thrilled that I was able to collaborate with them on a graduation project while working under their supervision. I have certainly enjoyed our discussions that guided me yet allowed to pursue my interest. The insightful feedback and comments provided throughout our meetings significantly assisted the progress of the thesis. I would like to express my gratitude for having the opportunity to do my thesis at DLR, where it is encouraged to ask questions and the colleagues are very friendly. Lastly, without the ongoing assistance and encouragement of my friends, family, and my girlfriend, this thesis would not have been achievable. I appreciate you supporting me and helping to make my degree a memory I will cherish forever.

Elrawy Soliman
Göttingen, March 2023

Abstract

Hybrid RANS-LES methods have become a popular numerical approach for a wide variety of flows. This is due to dissatisfaction with the RANS modelling paradigm in separated flows along with the prohibitive computational cost of pure LES, especially in wall-bounded flows at high Reynolds numbers. However, these methods are susceptible to the grey area problem, where the modeling approach is neither RANS nor LES: rather it is a region with an ambiguous modeling approach. In zonal approaches that function as embedded wall-modeled LES (WMLES), the transition from RANS to LES can be accelerated by improving the synthetic turbulence and its injection into the flow. In this work, a systemic assessment of the two aspects of zonal grey area mitigation methods was carried out. The synthetic turbulence was generated by the synthetic turbulence generator (STG) and injected into the flow using two different forcing terms. To ensure accurate second-order statistics of synthetic turbulence, a priori estimations of the bias error associated with a specific realization of a random number set were implemented and used. This resulted in smaller deviations between the statistics of the synthetic turbulence and the target Reynolds stresses. Furthermore, a modified synthetic turbulence forcing that ensures more accurate estimation of the total shear stress in close proximity to the RANS-LES interface was proposed. Moreover, a dynamic forcing that selectively enhances the production of underestimated Reynolds stresses was implemented and evaluated. These aspects resulted in a faster transition from RANS to LES in terms of both skin friction coefficients and Reynolds stresses. In addition, the WMLES capabilities of the subgrid length scale $\tilde{\Delta}_{\omega}$ together with the subgrid-scale σ-model were explored. This work revealed that this combination is troublesome when used as embedded WMLES with synthetic turbulence, especially in stable flows. This is due to excessively decreased levels of eddy viscosity in the near-wall RANS region.

Contents

Acknowledgements **i**

Abstract **ii**

Nomenclature **vii**

1 Introduction **1**

2 Modelling Approach **3**
2.1 DES Shortcomings . . . 3
2.2 Delayed Detached-eddy Simulation (DDES) . . . 4
2.3 Improved Delayed Detach Eddy Simulation (IDDES) . . . 5

3 Non-zonal Approaches: A Brief Study **7**
3.1 The Subgrid Length Scale: $\tilde{\Delta}_{\omega}$ . . . 7
3.2 The Subgrid-scale Model: σ-model . . . 8
3.3 Results . . . 9
3.3.1 Non-zonal use of σ-DDES with $\tilde{\Delta}_{\omega}$ . . . 9
3.3.2 Semi non-zonal use of σ-DDES with $\tilde{\Delta}_{\omega}$ . . . 11

4 Zonal Approaches: Research Focus and Activities **16**
4.1 Research objectives and Activities . . . 16
4.2 Test Cases . . . 18
4.2.1 Flat plat test case . . . 18
4.2.2 Rounded step test case . . . 19
4.2.3 Channel flow test case . . . 20
4.3 Numerical Setup . . . 20

5 Synthetic Turbulence Generation **22**
5.1 The Macro-scale Velocity . . . 23
5.2 The Cut-off Frequency . . . 25

6 The Input of the Synthetic Turbulence Generator: A Sensitivity Analysis **29**
6.1 Results . . . 31
6.1.1 Influence of the random number set: the flat plate test case . . . 31
6.1.2 Influence of the random number set and target Reynolds stresses: the rounded step test case . . . 33

7 Synthetic Turbulence Forcing: Assessment and Sensitivity **39**
7.1 The DLR Source Term . . . 39
7.2 The VSTG Source Term . . . 40
7.3 Results . . . 40
7.3.1 Interface forcing with the DLR source term . . . 41
7.3.2 Volumetric forcing: the volumetric DLR source term and the VSTG . . . 43
7.3.3 Effect of the forcing region in VSTG . . . 45

8 Improved Synthetic Turbulence Forcing **48**
8.1 Constrained Forcing . . . 48
8.2 Dynamic Forcing . . . 49
8.3 Results . . . 51
8.3.1 Results of the constrained forcing . . . 51
8.3.2 Results of dynamic forcing . . . 55

9 WMLES capabilities of $\sigma-$DDES and $\tilde{\Delta}_{\omega}$ **59**
9.1 WMLES capabilities of $\sigma-$DDES with $\tilde{\Delta}_{\omega}$ 59
9.2 Embedded WMLES use of $\sigma-$DDES with $\tilde{\Delta}_{\omega}$ 60

10 Conclusion and Recommendations **66**

References **68**

A Additional Results **70**

List of Figures

3.1 Rounded step test setups used in this brief study 9
3.2 Shielding/ delay function used in DDES f_d (left) and ν_t/ν computed using $\sigma-$DDES with $\tilde{\Delta}_\omega$ (right) 10
3.3 Results of using σ-DDES with $\tilde{\Delta}_\omega$ in a non-zonal manner in the upstream region 11
3.4 Results of using σ-DDES with $\tilde{\Delta}_\omega$ in a non-zonal manner in the rounded step region . . 12
3.5 Iso-surfaces of Q-criterion ($Q = 2U^2/H^2$), colored by the streamwise velocity for the rounded step case 13
3.6 Skin friction and pressure coefficient using σ-DDES with $\tilde{\Delta}_\omega$ in a non-zonal manner . . 13
3.7 Results of using σ-DDES with $\tilde{\Delta}_\omega$ in a non-zonal and "semi non-zonal" manner in the rounded step region 14
3.8 Skin friction and pressure coefficient using σ-DDES with $\tilde{\Delta}_\omega$ in a non-zonal and "semi non-zonal" manner 14

4.1 Research activities focused on the synthetic turbulence generation and its injection methods 17
4.2 Flat plate test case grid 18
4.3 Standard rounded step test case setup 19
4.4 Rounded step test case grid 20
4.5 Channel flow test case grid 20

5.1 Skin friction coefficient of the flat plate case time-averaged for different time periods. Results were obtained using the original STG with instantaneous U_0 and the DLR source term. 24
5.2 Iso-surfaces of Q-criterion (Q = $1U^2/\delta_0^2$), colored by the streamwise velocity, at increasing computation time from left to right. Results were obtained using the original STG with instantaneous U_0 and the DLR source term. 24
5.3 Synthetic streamwise velocity with mean U_0 and instantaneous U_0 25
5.4 Auto-correlation of synthetic streamwise velocity using mean U_0 and instantaneous U_0 25
5.5 Skin friction coefficient of the flat plate case time-averaged for 10 CTU. The results were obtained using the original STG and NTS-STG with the mean U_0 and the DLR source term. 26
5.6 Comparison between the erroneous and the correct f_{cut} for the flat plate test case 26
5.7 Comparison between the normalized amplitude distribution using the erroneous and the correct f_{cut} for the flat plate test case 27
5.8 The normalized amplitude distribution for the flat plate test case at $y \approx 15\%\ \delta_0$ 27
5.9 Skin friction with the correct f_{cut} for the flat plate test case. Results were obtained using the original STG and NTS-STG with the mean U_0 and the DLR source term. 27

6.1 Schematic showing the area of focus in this chapter 29
6.2 Statistics of the synthetic turbulence using two different random number set realizations for the flat plate test case 32
6.3 Statistics of the synthetic turbulence and the resolved velocities for the flat plate. Solid lines: random realization, dashed lines: with the selection procedures 33
6.4 Skin friction coefficient and pressure fluctuations for the flat plate case using the DLR source term 33
6.5 Statistics of the synthetic turbulence and the resolved velocities with RANS target Reynolds stress for the rounded step. Solid lines: random realization, dashed lines: with the selection procedures 34
6.6 Skin friction and pressure coefficient using RANS target Reynolds stresses 35

6.7 Statistics of the synthetic turbulence and the resolved velocities with DNS target Reynolds stress for the rounded step. Solid lines: random realization, dashed lines: with the selection procedures 35
6.8 Skin friction and pressure coefficient using DNS target Reynolds stresses 36
6.9 Comparison between using DNS and RANS as target Reynolds stresses with (dashed lines) and without (solid lines) the selection procedures upstream the curved section . . 37
6.10 Comparison between using DNS and RANS as target Reynolds stresses with (dashed lines) and without (solid lines) the selection procedures at the curved step 38

7.1 Results of interface forcing using the DLR source term for the flat plate case at the interface ($x = 0$) 41
7.2 Results of interface forcing using the DLR source term for the flat plate case at $x = 3\delta_0$. 42
7.3 ν_t/ν for the flat plate case, using SA and SST as the underlying RANS models. The synthetic turbulence was injected using the DLR source term. 42
7.4 Skin friction coefficient and pressure fluctuations for the flat plate case using interface forcing of the DLR source term 43
7.5 Skin friction coefficient and pressure fluctuations for the flat plate case using interface forcing of the DLR source term and a different random number set in SST-IDDES computation. 43
7.6 Results of volumetric forcing for the flat plate case at $x = 0.25\delta_0$. The forcing region size is 0.5 δ_0. 44
7.7 Results of volumetric forcing for the flat plate case at $x = 3\delta_0$. The forcing region size is 0.5 δ_0. 45
7.8 Skin friction coefficient and pressure fluctuations for the flat plate case using volumetric source terms. The forcing region size is 0.5 δ_0. 45
7.9 Results of the VSTG forcing with different forcing region sizes for the flat plate case at $x = 3\delta_0$. The forcing region sizes are $1\delta_0$and$2\delta_0$. 46
7.10 Skin friction coefficient and pressure fluctuations for the flat plate case using VSTG forcing with different forcing region sizes. The forcing region sizes are $1, 2$ δ_0. 47

8.1 f_b and $1 - f_b$ functions used in the constrained forcing 49
8.2 Results of the DLR source term and constrained forcing for the flat plate case at the interface (x = 0) 51
8.3 Results of the DLR source term and constrained forcing for the flat plate case at $x = 3\delta_0$ 52
8.4 Friction coefficient and pressure fluctuations for the flat plate case using The DLR source term and constrained forcing 53
8.5 Velocity gradients for the flat plate at $x = 0.25$ δ_0 using the DLR source term and constrained forcing 53
8.6 Results of the constrained forcing combined with both the interface and the volumetric forcing of the DLR source term for the rounded step case. The results are shown at the upstream region. 54
8.7 Results of the constrained forcing combined with both the interface and the volumetric forcing of the DLR source term for the rounded step case. The results are shown at the curved step region 55
8.8 Skin friction and pressure coefficients using the constrained forcing combined with both the interface and the volumetric forcing of the DLR source term for the rounded step case. 56
8.9 Results of the volumetric DLR source term combined with the dynamic forcing for the flat plate case at $x = 0.25$. The forcing region size = $0.5\delta_0$ 56
8.10 Results of dynamic forcing for the flat plate case at $x = 3\delta_0$ 57
8.11 Skin friction coefficient and pressure fluctuations for the flat plate case using the volumetric DLR source term combined with dynamic forcing 58

9.1 Results comparing IDDES and $\sigma-$DDES with $\tilde{\Delta}_\omega$ for the channel flow case 60
9.2 Iso-surfaces of Q-criterion ($Q = 0.5U^2/\delta$), colored by the streamwise velocity for the channel flow 60
9.3 Results of using σ-DDES with $\tilde{\Delta}_\omega$ in an embedded WMLES manner for the flat plate case at $x = 3\delta_0$ 61

9.3 Results of using σ-DDES with $\tilde{\Delta}_\omega$ in an embedded WMLES manner for the flat plate case at $x = 3\delta_0$ (continued from previous page) 62
9.4 Results of using σ-DDES with $\tilde{\Delta}_\omega$ in an embedded WMLES manner for the flat plate case at $x = 3\delta_0$ 62
9.5 Results of using σ-DDES with $\tilde{\Delta}_\omega$ in an embedded WMLES manner for the rounded step 63
9.6 Results of using σ-DDES with $\tilde{\Delta}_\omega$ in an embedded WMLES manner for the rounded step 64
9.7 Skin friction and pressure coefficient using σ-DDES with $\tilde{\Delta}_\omega$ in an embedded WMLES manner. 65

A.1 Results of the VSTG forcing with different forcing region sizes for the flat plate case at $x = 1\delta_0$. The forcing region sizes are $1\delta_0$ and $2\delta_0$. 71
A.2 Results of using σ-DDES with $\tilde{\Delta}_\omega$ in an embedded WMLES manner for the flat plate case at the interface ($x = 0$) 72

Nomenclature

	Abbreviations
APG	Adverse Pressure Gradient
CTU	Convective Time Unit
DDES	Delayed Detached-Eddy Simulations
DES	Detached-Eddy Simulations
DLR	Deutsches Zentrum für Luft- und Raumfahrt
GA	Grey Area
HRLM	Hybrid RANS-LES Methods
Hyb	Hybrid
IDDES	Improved Detached-Eddy Simulations
IDL	Internal Damping Layer
LES	Large Eddy Simulations
LLM	Loglayer Mismatch
MSD	Modeled Stress Depletion
NTS-STG	A New variant of the STG
RANS	Reynolds-Averaged Navier-Stokes
SEM	Synthetic-Eddy Methods
SGS	Subgrid Scale
ST	Synthetic Turbulence
STG	Synthetic Turbulence Generator
URANS	Unsteady RANS
WMLES	Wall-modeled Large Eddy Simulations
ZPG	Zero Pressure Gradient
	Greek Symbols
ρ	Air density

δ	Boundary layer thickness
ε	Dissipation rate
ν	Kinematic viscosity
Ψ	Low-Re correction function
Γ	Parameter determines the intensity of dynamic forcing
ω	specific dissipation rate
Δ	Subgrid length scale
ν_t	Turbulent viscosity
$\boldsymbol{\omega}$	Vorticity
κ	Wave number
	Roman Symbols
$\mathcal{D}$	Differential operator
C	Modeling constant
d_w	Wall distance
f_d	Delay/shielding function
F_i	Source term
k	Turbulence kinetic energy
l	Length scale
N	Number of Fourier modes
P	Freestream Pressure
q	Normalized Fourier modes amplitudes in STG
S	Strain rate
t	Time
U	Freestream velocity
u	Streamwise velocity
U_0	Macro-scale velocity
v	Wall-normal velocity
w	Spanwise velocity
	Subscripts

cut	cut-off frequancy/length scale
η	Kolmogorov frequancy/length scale
σ	Sigma model
Smag	Smagorinsky model
s	Synthetic velcocity

1
Introduction

There has been an increasing interest in hybrid RANS-LES methods (HRLM), motivated by several reasons. Firstly, there is dissatisfaction with the RANS modeling approach, particularly for separated flows, where its accuracy suffers despite years of development efforts [1]. Secondly, pure LES methods, while more accurate than RANS, are computationally prohibitive, especially for wall-bounded flows at high Reynolds numbers. Additionally, there is a growing interest in unsteady flow characteristics, most notably in aeroacoustics research. Furthermore, there is a need for more precise flow predictions near the limits of the design envelope, where separation and unsteadiness are characteristic. As a result, several new hybrid methods have emerged, the most widely used being Detached-Eddy Simulations (DES) [2].

In DES, attached boundary layers are treated entirely by RANS, whereas separated flows are treated by LES. When switching from RANS to LES, an area of undefined modeling approach may exist, where the modeling approach is neither RANS nor a proper LES. This is referred to as the Grey Area (GA) problem and is extensively studied in the literature (see [3] and [4]). The grey area is the result of switching the modeling approach from RANS to LES without sufficient resolved turbulent content. The severity of the grey area problem depends on the flow, where flows with shallow separation are more severely affected as opposed to massively separated flows with their strong natural instabilities. As a result, flows with shallow separation typically require the injection of synthetic turbulence to stimulate the development of turbulent content.

Based on the definition of the RANS-LES interface, whether defined manually by the user or automatically by the HRLM itself, two modeling approaches are distinguished, zonal and non-zonal. Non-zonal approaches rely on intrinsic flow instabilities, such as the ones in separated shear layers, as the source of resolved turbulent content. In these approaches, the delay in transitioning from modeled to resolved turbulence is due to the high levels of subgrid-scale (SGS) viscosity in the initial regions of the shear layers. Such high levels of SGS viscosity dampen the intrinsic flow instabilities of free shear layers, hindering their development into resolved turbulence. These large magnitudes of SGS viscosity are due to one of the following reasons. The first is the anisotropic grids (large spanwise spacing), typically used in the initial shear layers region, combined with using Smagorinsky-like models that are calibrated for isotropic cells. The second reason is the Smagorinsky-like model itself, which is unable to recognize quasi-2D flows and decrease its viscosity level accordingly [3].

To mitigate the grey area problem in non-zonal approaches, a considerable decrease in the SGS viscosity in the early shear layer regions is required. This can be achieved by modifying the subgrid length scale or the SGS model. Chauvet et al. [5] introduced the concept of sensitizing the subgrid length scale to the orientation of the vorticity vector in the grid. The formulation was later generalized to be used for unstructured grids by Deck [6]. Shur et al. [3] improved the formulation by decreasing the influence of the smallest grid spacing and proposed $\tilde{\Delta}_{\omega}$. On the other hand, Mockett et al. [4] proposed using the $\sigma-$model of [7] as the SGS model.

In contrast, zonal approaches when used as embedded wall-modeled LES (WMLES) rely on the injection of synthetic turbulence into the flow field as the source of turbulence content. These zonal approaches should be distinguished from the zonal DES (ZDES) by Deck [8], which may not always involve the injection of synthetic turbulence. The former is the focus of this work and is referred to as zonal approaches for short. In such zonal approaches, the delay in the transition from fully modeled to resolved turbulence is determined by the quality of the injected synthetic turbulence and how it is introduced into the flow. It is believed that a good approximation of the low-order statistics of wall-bounded flows can be obtained when injecting turbulent structures whose shapes are representative of physically coherent structures in the boundary layer [9]. Thus, shortening the RANS-LES transition in zonal approaches requires improving the quality of the synthetic turbulence itself as well as its injection methods [10]. Examples of synthetic turbulence generators include the Synthetic Eddy Method (SEM) and the Synthetic turbulent generator (STG), proposed by Jarrin et al. [11] and Adamian et al. [12], respectively.

Even though non-zonal methods may seem more attractive, as they do not require injecting synthetic turbulence, their effectiveness highly depends on the flow problem. In the literature, non-zonal grey area mitigation methods are extensively applied in flow cases with strong natural instabilities, typically free shear layers resulting from abrupt separation. Examples of such flow cases include a spatially developing plane mixing layer, a backward-facing step, and an unheated jet, studied by Mockett et al. [4] and Shur et al. [3]. There is a consensus that non-zonal grey area mitigation methods will struggle in more challenging flow cases, such as adverse-pressure gradient (APG) separations. In this work, non-zonal grey area mitigation methods, specifically σ-DDES and $\tilde{\Delta}_{\omega}$, are applied to such challenging flow cases, where their inadequacy is illustrated.

In this work, zonal grey area mitigation methods are assessed, some of which are improved. Zonal approaches have two main aspects: the first is the synthetic turbulence itself, and the second is the forcing term used to inject it into the flow. This work analyzes the STG of [12] and the modified variant NTS-STG of [13]. Furthermore, the source term proposed by Probst [14] as well as that by Shur et al. [15] are evaluated. In the literature, synthetic turbulence generation methods are often treated as a black box, where their direct output is rarely analyzed. This work presents a systematic assessment of the quality of the synthetic turbulence and its injection methods. First, the statistics of synthetic turbulence are evaluated when varying two input parameters, the target Reynolds stress and the random number set used in both variants of the STG. The aim of the latter is to reduce the bias errors associated with a specific realization of random numbers [16]. Then, the two source terms are evaluated, where the advantages and limitations of each are discussed. Two modifications to the source terms are proposed to address the encountered shortcomings.

This thesis starts with the description of the modeling framework by presenting DES and its different versions in chapter 2. Thereafter, a brief study, highlighting the limitations of non-zonal grey area mitigation methods, is carried out in chapter 3. This is followed by a presentation of the different aspects of the research activities in chapter 4. The main research activities of this thesis start with discussing the synthetic turbulence generation and analyzing two main parameters that affect its quality in chapter 5. With the ensured quality of the synthetic turbulence, its sensitivity to two input parameters, the random number set and the target Reynolds stresses, is evaluated and discussed in chapter 6. Then, chapter 7 assesses different synthetic forcing methods, with a focus on the resolved stresses in close proximity to the forcing region. Based on the shortcomings encountered with the assessed source terms, two modifications are proposed in chapter 8. In chapter 9, σ-DDES and $\tilde{\Delta}_{\omega}$ are used to perform WMLES and embedded WMLES to assess their WMLES capabilities. In chapter 10, conclusions of the research are highlighted and recommendations for future work are presented.

2

Modelling Approach

Detached Eddy Simulation (DES) is a popular hybrid RANS-LES method (HRLM) in the industrial CFD community. The principle of this method is to treat the entire attached turbulent boundary layer with RANS and apply LES to regions with large flow separations. Therefore, having the RANS-LES interface inside the boundary layer is not the intended use of the method, which Mockett [17] refers to as extended uses of DES. Extended use of DES includes using DES as (embedded) wall-modeled LES, where only the near-wall region is modeled with RANS and the rest of the boundary layer is treated by LES. This is possible, in principle, through grid design in a manner that the modeling paradigm switches in the boundary layer. However, this does not provide the desired behavior in stable flows because the upstream region RANS lacks resolved turbulent content, leading to the grey area problem discussed in section 2.1.

The original formulation of DES was proposed by Spalart [2] and is commonly referred to as DES97. Since it is aimed to use the same model for both the RANS and LES regions, the RANS model with wall distance in its formulation is a natural choice for DES97. In DES97 formulation, a DES length scale was introduced to replace the Spalart–Allmaras (SA) wall distance (d_w). The length scale in DES97 is as follows:

$$l_{\mathrm{DES97}} = \min\left(d_w; l_{\mathrm{LES}}\right), \quad l_{\mathrm{LES}} = C_{\mathrm{DES}}\Delta, \quad \Delta = \max\left(\Delta x; \Delta y; \Delta z\right). \tag{2.1}$$

In the near-wall region, where $d_w < l_{\mathrm{LES},}$, the DES length scale is set to the RANS model length scale, and the model formulation is identical to the SA RANS model. Far from the wall, $d_w > l_{\mathrm{LES}}$, and hence the LES length scale (l_{LES}) is used. l_{LES} is a function of only the local grid cell size, Δ, multiplied by a model constant C_{DES}. This non-zonal switching between RANS and LES modes is theoretically a valuable feature of DES97, but it turned out to be problematic. Undesired switching between RANS and LES can occur on ambiguous grids. This problematic behavior along with other shortcomings of DES97 are discussed in section 2.1.

2.1. DES Shortcomings

Several shortcomings have been identified with DES97. While some of them were expected from the beginning, others have been revealed in subsequent studies [17]. The first issue with DES97 is the erroneous activation of near-wall damping terms in the LES mode. Some RANS models, including the SA model, have dampening terms in their formulation to ensure correct near-wall behavior. When these RANS models are applied in DES97, the activation of the LES length scale could erroneously activate these damping terms, which will in turn decrease the subgrid-scale (SGS) viscosity to near-zero levels.

Another issue with DES97 is the activation of the LES mode inside the boundary layer, which is a result of the length scale definition. DES97 formulation assumes that tangential grid spacings near the wall are much larger than the boundary layer thickness (δ), more specifically $\Delta x,\ \Delta z \gg \delta / C_{\mathrm{DES}}$. If this is the case, the switching from RANS to LES, where $d_w = C_{\mathrm{DES}}\Delta$, will be located outside the boundary layer, as intended. Otherwise, the switching from RANS to LES will take place in the boundary layer, resulting in excessively reduced levels of eddy viscosity in the LES region due to the activation of the LES mode. In the latter case, the grid is too fine for the correct functioning of DES97, but too coarse for LES to resolve the turbulent boundary layer structures. This ambiguous grid resolution leads to a decrease in modeled Reynolds stresses and is therefore referred to as modeled stress depletion (MSD).

MSD is one of the most serious problems encountered in DES97, especially in industrial applications. This is because obtaining such large tangential grid spacing (e.g. in the streamwise direction) is not always practical in terms of an accurate representation of the geometry. Furthermore, the fact that the results deteriorate as the mesh is refined is not only undesirable but also paradoxical.

The Grey Area problem is another shortcoming of DES97. It is a region where the modeling mode is neither RANS nor a fully developed LES; rather, it is a region with an undetermined modeling mode. To demonstrate this problem, consider a boundary layer flow that separates from a surface and transforms into a free shear layer. In the initial part of the separated boundary layer, LES mode should be active, and the turbulent kinetic energy should be mostly resolved. However, resolved turbulent content is required for LES mode to operate correctly, which cannot be provided by the upstream RANS region. Therefore, the modeling mode in this region is not LES due to the lack of resolved turbulence, nor is it RANS due to the reduced eddy viscosity as a result of using the reduced length scale of LES (l_{LES}). This is aggravated by the transport of eddy viscosity from the upstream RANS region. The severity of the grey area problem depends on the flow case and the strength of the shear layer instabilities. The problem is more severe in stable flows, such as shallow separations, which lack strong natural instabilities that could quickly develop into resolved turbulence. On the contrary, unstable flows, such as massively separated flows, can quickly develop such natural instabilities. As a result, unstable flows can show resolved turbulence relatively quickly downstream of the RAN-LES interface, thus they are not severely affected by the grey area problem.

A final drawback of DES97 is the Log Layer Mismatch (LLM). The LLM appears as a kink in the velocity profile between the RANS and LES logarithmic layers, resulting in an underestimation of the skin friction coefficient of the order of 15% [17]. LLM is a common issue even in zonal HRLM, which the IDDES formulation attempts to solve as discussed in section 2.3.

2.2. Delayed Detached-eddy Simulation (DDES)

Delayed Detached-Eddy Simulation (DDES) is an enhanced version of DES97 that addresses some of the aforementioned shortcomings. First, the issue of the damping terms being active in the LES mode is addressed with a correction function Ψ. The reader is directed to [18] for the exact formulation of Ψ. Briefly, Ψ restores the Smagorinsky model behavior for all values of eddy viscosity, and is included in the length scale definition as follows:

$$l_{\text{LES}} = C_{\text{DES}}\Psi\Delta. \tag{2.2}$$

Next, the issue of the LES incursion within the boundary layer that causes modeled stress depletion is resolved using a shielding/delay function (f_d). In DES97, the switching from RAN to LES is based solely on the grid spacings, which results in the grid ambiguity issue. To solve this issue, it is natural to formulate a new length scale to be dependent on the solution. Spalart et al. [18] proposed a sensor that is able to detect the boundary layer, and is defined as follows:

$$r_d = \frac{\nu_t + \nu}{\kappa^2 d_w^2 \max\left(\sqrt{\frac{\partial U_i}{\partial x_j}\frac{\partial U_i}{\partial x_j}}; 10^{-10}\right)} \tag{2.3}$$

The sensor r_d is based on the function r from the SA model but modified to be applicable to any eddy viscosity model. Using this sensor, the delay function f_d blends between the RANS region and the LES region and reads

$$f_d = 1 - \tanh\left[(c_d r_d)^3\right] \tag{2.4}$$

where c_d is a coefficient with a value of 8, unless stated otherwise. The ideal behavior of the delay function is such that $f_d = 0$ inside turbulent boundary layers, and blends smoothly to $f_d = 1$ at the edge of the boundary layer. As a result, f_d prevents the activation of the LES mode inside the boundary layer using a hybrid length scale that is defined as follows:

$$l_{\text{DDES}} = l_{\text{RANS}} - f_d \max\left(0; l_{\text{RANS}} - l_{\text{LES}}\right) \tag{2.5}$$

With this length scale definition, DDES addresses most of the shortcomings of DES97, with the exception of the LLM issue. However, the boundary layer is still fully modeled by RANS, rendering DDES incapable of performing WMLES. An Improved version of DDES (IDDES) that addresses the LLM issue and allows for WMLES capabilities was proposed in [19].

2.3. Improved Delayed Detach Eddy Simulation (IDDES)

Improved Delayed Detach Eddy Simulation (IDDES) is an improved version of DDES proposed by Shur et al. [19]. The IDDES formulation has two branches: DDES and WMLES. The WMLES branch was proposed to solve the LLM issue. The main components of this method are a new formulation of the near-wall LES subgrid length scale Δ and a faster switching between RANS and LES modes compared to DES97 and DDES.

First, a new subgrid length scale was proposed. This was done as an alternative to changing the Smagorinsky constant, depending on whether the flow is homogeneous or sheared. The new formulation of the subgrid length scale reads as follows:

$$\Delta_{\text{IDDES}} = \min\left[\max\left(C_w d_w; C_w h_{\max}; h_{wn}\right); h_{\max}\right] \tag{2.6}$$

where $h_{\max}$ is the maximum grid spacing in all three directions, i.e., the standard $\Delta_{\max}$. h_{wn} is the spacing in the wall-normal direction, and C_w is an empirical constant with a value of 0.15.

The second component of the IDDES formulation is the rapid switching from RANS to LES within the boundary layer. This enables IDDES to perform WMLES, where a large part of the boundary layer is resolved. The WMLES branch is intended to be active only when turbulent content is present and the grid is fine enough to resolve the large turbulent structures in the boundary layer. The WMLES branch merges between RANS and LES through a new hybrid length scale l_{WMLES}, defined as follows:

$$l_{\text{WMLES}} = f_{\text{B}}\left(1 + f_{\text{e}}\right) l_{\text{RANS}} + \left(1 - f_{\text{B}}\right) l_{\text{LES}} \tag{2.7}$$

where f_{B} and f_{e} are the two ingredients of the new hybrid length scale definition. f_{B} is an empirical blending function that switches rapidly between RANS ($f_{\text{B}} = 1$) and LES ($f_{\text{B}} = 0$) modes. It is a function of the ratio $d_{\text{w}}/h_{\max}$ and reads

$$f_{\text{B}} = \min\left\{2\exp\left(-9\alpha^2\right), 1.0\right\}, \quad \alpha = 0.25 - d_{\text{w}}/h_{\max}. \tag{2.8}$$

The second empirical function, f_e, aims to eliminate the LLM issue by preventing excessive reduction of modeled Reynolds stresses near the RANS-LES interface. This is achieved by increasing the RANS length scale near the interface. f_{e} is known as the elevation function since it increases the modeled Reynolds stresses and is given by

$$f_{\text{e}} = \max\left\{\left(f_{\text{e1}} - 1\right), 0\right\} \Psi f_{\text{e2}} \tag{2.9}$$

f_{e} consists of two components, one is grid-dependent and the other solution-dependent. The grid-dependent component, f_{e1}, is defined as follows:

$$f_{\text{e1}}\left(d_{\text{w}}/h_{\max}\right) = \begin{cases} 2\exp\left(-11.09\alpha^2\right) & \text{if} \quad \alpha \geq 0 \\ 2\exp\left(-9.0\alpha^2\right) & \text{if} \quad \alpha < 0 \end{cases} \tag{2.10}$$

The solution-dependent component is defined similarly to Equation 2.4, however, the turbulent viscosity ν_t and the laminar viscosity ν are separated into two different terms and renamed r_{dt} and r_{dl}, respectively. The reader is referred to [19] for their detailed formulation.

The final aspect of the IDDES formulation is to combine the newly developed WMLES branch and the DDES branch. The DDES length scale Equation 2.5 and that of the WMLES branch Equation 2.7 are combined in a manner that ensures the proper selection of the branch based on the presence of turbulent content and the grid resolution. To achieve this, Shur et al. [19] proposed a modified formulation of l_{DDES}, which is practically equivalent to the original formulation in Equation 2.5. The modified l_{DDES}, denoted $\tilde{l}_{\text{DDES}}$, reads:

$$\tilde{l}_{\text{DDES}} = \tilde{f}_{\text{d}} l_{\text{RANS}} + \left(1 - \tilde{f}_{\text{d}}\right) l_{\text{LES}} \tag{2.11}$$

where the blending function $\tilde{f}_{\text{d}}$ is defined as follows:

$$\tilde{f}_{\text{d}} = \max\left\{\left(1 - f_{\text{dt}}\right), f_{\text{B}}\right\} \tag{2.12}$$

with $f_{\mathrm{dt}} = 1 - \tanh\left[(8r_{\mathrm{dt}})^3\right]$. Using Equation 2.11, the hybrid IDDES length scale that combines the DDES branch and the WMLES branch is then:

$$l_{\mathrm{hyb}} = \tilde{f}_{\mathrm{d}}\,(1 + f_{\mathrm{e}})\,l_{\mathrm{RANS}} + \left(1 - \tilde{f}_{\mathrm{d}}\right) l_{\mathrm{LES}} \tag{2.13}$$

The choice to operate in one of the branches is assessed as follows: in case the flow field contains turbulent content, $r_{\mathrm{dt}} \ll 1$; f_{dt} is close to 1.0 ; therefore $\tilde{f}_{\mathrm{d}}$ is equal to f_{B}; and so $l_{\mathrm{hyb}} = l_{\mathrm{WMLES}}$. Otherwise, f_e becomes zero, and then $l_{\mathrm{hyb}} = \tilde{l}_{\mathrm{DDES}}$. In this work, the WMLES branch is enforced by manually setting $f_{\mathrm{dt}} = 1$.

From DES97 through DDES and subsequently IDDES, it is evident that complexity has been rising. However, IDDES is regarded as the most suitable formulation for wall-bounded flows, which is of major relevance in this work, because of its capacity to address the LLM issue. Furthermore, the IDDES formulation provides proper WMLES capability in the sense that most of the turbulent structures in boundary layers are resolved.

3

Non-zonal Approaches: A Brief Study

Non-zonal DES-like methods rely on the natural instabilities of the flow, such as in free shear layers or separated flows, as the source of resolved turbulence. This makes them attractive as they do not require injecting synthetic turbulence. However, these instabilities get typically dampened, which results in a delayed transition from modeled to resolved turbulence, especially in stable flows. The dampening of the instabilities occurs due to two reasons. The first is the convection of eddy viscosity from the upstream attached boundary layer treated by RANS, while the second is the excessively large modeled turbulence in the initial part of the separated flow region treated by LES. The latter is caused by the anisotropy of the grid or the Smagorinsky-like subgrid-scale models, typically used in DES-like methods [3]. Two strategies that address the latter are the subgrid length scale $\tilde{\Delta}_\omega$ [3] and subgrid-scale (SGS) $\sigma-$model [7], which are discussed in this chapter.

Although using σ-DDES with $\tilde{\Delta}_\omega$ as a non-zonal grey area mitigation approach is common in the literature, these studies only investigate cases with massive separation. It is believed that non-zonal grey area mitigation approaches, such as the σ-DDES and $\tilde{\Delta}_\omega$, will struggle in more stable flow cases (e.g. smooth body separation) due to the lack of sufficient natural instabilities. This is evaluated in this brief study, where σ-DDES with $\tilde{\Delta}_\omega$ are applied to a test case with pressure-induced separation. In this chapter, the rounded step test case, which is detailed in subsection 4.2.2, is used to illustrate the limitations of non-zonal methods in stable flows. The rounded step is a shallow separation test case, with an expansion of $1H$ (the step high), resulting in a pressure-induced separation and subsequent re-attachment. Note that the subgrid length scale $\tilde{\Delta}_\omega$ and the SGS $\sigma-$model are also used in embedded WMLES computations as part of the main research activities, detailed in section 4.1.

3.1. The Subgrid Length Scale: $\tilde{\Delta}_\omega$

The first version of DES (DES97) is known to have a slow transition from modeled to resolved turbulence in free and separated shear layers due to excessively large modeled turbulence [20]. The anisotropic grids in these regions, which are fine across a shear layer but coarse in the spanwise direction, are one main cause of the high levels of eddy viscosity. Such cells produce grids that differ greatly from the isotropic cells assumed in LES functions within the DES approach. As a result, the subgrid length scale Δ_{max}, defined in the original DES formulation, produces too large modeled turbulence. This is far from the intended functioning of DES, as it is intended to operate in LES mode in separated flow regions. This issue, which was anticipated by Spalart [2] in their first introduction of DES, severely decreases the accuracy of flow predictions, especially in flows with shallow boundary layer separations.

To address this shortcoming, new subgrid length scales that are dependent on the solution and not merely on the grid resolution have been proposed in the literature. Chauvet et al. [5] introduced the idea of sensitizing the subgrid length scale to the orientation of the vorticity vector. The formulation was later generalized to be used for unstructured grids by Deck [6]. Shur et al. [3] improved the formulation by limiting the influence of the smallest grid spacing and proposed $\tilde{\Delta}_\omega$. For a cell-centered at $\mathbf{r}$ and its vertices located at $\mathbf{r}_n$ (for a hexahedral cell, r = 1...8), the new subgrid length scale $\tilde{\Delta}_\omega$ reads:

$$\tilde{\Delta}_\omega = \frac{1}{\sqrt{3}} \max_{n,m=1,8} |(\mathbf{l}_n - \mathbf{l}_m)| \tag{3.1}$$

where $\mathbf{l}_n = \mathbf{n}_\omega \times \mathbf{r}_n$ and $\mathbf{n}_\omega$ is the unit vector aligned with the vorticity vector.

This subgrid length scale offers some advantages over the standard DES97 length scale Δ_{max} and the length scale of [5], Δ_ω. To demonstrate these advantages, consider the example of a free shear layer flowing in the x-y plane, with a large grid spacing in the z-direction. Since the vorticity vector is nearly aligned with the z-direction at the beginning of the shear layer, $\tilde{\Delta}_\omega$ reduces to $\frac{1}{\sqrt{3}}\left(\Delta x^2 + \Delta y^2\right)^{1/2}$, i.e., it is $O(\max\{\Delta x, \Delta y\})$ instead of Δz that would have resulted when using Δ_{max} formulation or $\sqrt{\Delta_x \Delta_y}$ when using the Δ_ω definition. In this flow case, a subgrid length scale of the order of $O(\max\{\Delta x, \Delta y\})$ is the most physically plausible, because the eddies have a similar size in both x and y directions in that region. Hence, the larger of the two dimensions limits the size of the eddies that can be resolved.

Furthermore, for fully-developed turbulence, $\tilde{\Delta}_\omega$ reduces to the standard Δ_{max} definition. Therefore, the formulation in Equation 3.1, unlike Δ_ω of [5], does not result in a strong influence of the smallest grid spacing while still being able to decrease the subgrid length scale (and hence the modeled turbulence) in quasi-2D regions discretized using strongly anisotropic grids. $\tilde{\Delta}_\omega$ is used as an alternative subgrid length scale in this study.

Initial tests performed in [3] revealed that if the x-y grid cannot resolve the Kelvin Helmholtz instabilities, replacing Δ_{max} with $\tilde{\Delta}_\omega$ is not enough to enable the desired effects. An addition in the form of a kinematic measure was needed to quickly detect quasi-2D flows that require a near implicit LES (ILES) treatment to facilitate the growth of the Kelvin Helmholtz instabilities and therefore accelerate the transition to resolved turbulence. In their research, Shur et al. [3] introduced the Vortex Tilting Measure (VTM), which is defined as follows:

$$\mathrm{VTM} \equiv \frac{\sqrt{6}|(\mathbf{S}\cdot\boldsymbol{\omega})\times\boldsymbol{\omega}|}{\omega^2\sqrt{3\,\mathrm{tr}\,(\mathbf{S}^2) - [\mathrm{tr}(\mathbf{S})]^2}} \tag{3.2}$$

Where $\mathbf{S}$ is the strain tensor and tr is the trace. The reader is encouraged to consult the original publication for more details regarding the formulation. In this study, the VTM is combined with $\tilde{\Delta}_\omega$ to further decrease the eddy viscosity in an attempt to further accelerate the RANS-LES transition, as discussed in subsection 3.3.1.

3.2. The Subgrid-scale Model: σ-model

Another main cause of the excessively large modeled turbulence in the LES region is the use of Smagorinsky-like SGS models. Such SGS models are incapable of recognizing areas with quasi-2D flows and thereafter decreasing the SGS viscosity to the appropriate levels. This is of great importance in DES-like methods, where the switching between the RANS mode in the upstream attached flow region and the LES mode in the separated flow region is non-zonal. So, the subgrid-scale model should be able to decrease the SGS viscosity in the separated flow region, where the modeling approach is LES.

The Smagorinsky SGS model is defined as follows:

$$\nu_{\mathrm{Smag}} = \left(C_{\mathrm{Smag}}\Delta\right)^2 \mathcal{D}_{\mathrm{Smag}} \tag{3.3}$$

where C_{Smag} is the Smagorinsky constant, Δ is a subgrid length scale, and $\mathcal{D}_{\mathrm{Smag}}$ is the differential operator of the Smagorinsky model, which is based on the strain rate of the resolved velocity field:

$$\mathcal{D}_{\mathrm{Smag}}(u) = \sqrt{2S_{ij}S_{ij}} \tag{3.4}$$

Nicoud et al. [7] proposed a new SGS model with an improved differential operator $\mathcal{D}_\sigma$ that is capable of detecting quasi-2D flows. The improved operator makes use of the singular values of the velocity gradient tensor and vanishes for two-component or two-dimensional flows. The differential operator of the σ−model and its associated SGS viscosity are then given by:

$$\mathcal{D}_\sigma = \frac{\sigma_3(\sigma_1 - \sigma_2)(\sigma_2 - \sigma_3)}{\sigma_1^2} \tag{3.5}$$

$$\nu_\sigma = (C_\sigma\Delta)^2\,\mathcal{D}_\sigma \tag{3.6}$$

where $\sigma_1 \geq \sigma_2 \geq \sigma_3 \geq 0$ are the three eigenvalues of the velocity gradient tensor, C_σ is a calibration constant, and Δ is a subgrid length scale.

The σ-DDES approach uses $\sigma-$model in a manner that maintains the original velocity scale unchanged in the RANS region, but switches to the new formulation $B_\sigma \mathcal{D}_\sigma$ in the LES region, where B_σ is a calibrated constant. The formulation of the σ-DDES, which was proposed by Mockett et al. [4], reads

$$\mathcal{D}_{\sigma-DDES} = \mathcal{D}_{\text{RANS}} - f_d \,\text{pos}\,(L_{\text{RANS}} - L_{\text{LES}})\,(\mathcal{D}_{\text{RANS}} - B_\sigma \mathcal{D}_\sigma) \tag{3.7}$$

$\mathcal{D}_{\text{RANS}}$ is inherited from the underlying RANS model and represents a scale based on the strain rate or the vorticity rate invariant. The delay function f_d is maintained to prohibit the activation of the new operator in the RANS region, which could result in MSD on ambiguous grids. The pos-function is equal to 1 if its argument is positive, but null otherwise. Using the $\sigma-$DDES formulation, a considerable decrease in SGS viscosity is expected to be achieved in quasi-2D flow regions, which in turn reduced the damping of the natural flow instabilities. The $\sigma-$model is, unlike $\tilde{\Delta}_\omega$, active even on isotropic cells.

In the next section, the effectiveness of $\sigma-$DDES with $\tilde{\Delta}_\omega$ in terms of facilitating the development of natural flow instabilities is evaluated. They are applied to a challenging test case that does not have strong natural instabilities as a result of the smooth APG-induced separation. In this regard, this test case is different from the commonly investigated cases. The commonly studied test cases are with fixed separation point as a result of abrupt changes in geometry, such as the backward facing steps test case and the spatially developing plane mixing layer test case, studied by Shur et al. [3] and Mockett et al. [4].

3.3. Results

In this section, the rounded step test case is used to evaluate $\sigma-$DDES with $\tilde{\Delta}_\omega$. The flow conditions and the grid are described in subsection 4.2.2. The aim is to evaluate whether the use of $\sigma-$DDES with $\tilde{\Delta}_\omega$ will facilitate the development of weak natural flow instabilities, resulting from APG-induced separation. The setup used in subsection 3.3.1 and the one used in subsection 3.3.2 are shown in Figure 3.1a and Figure 3.1b, respectively.

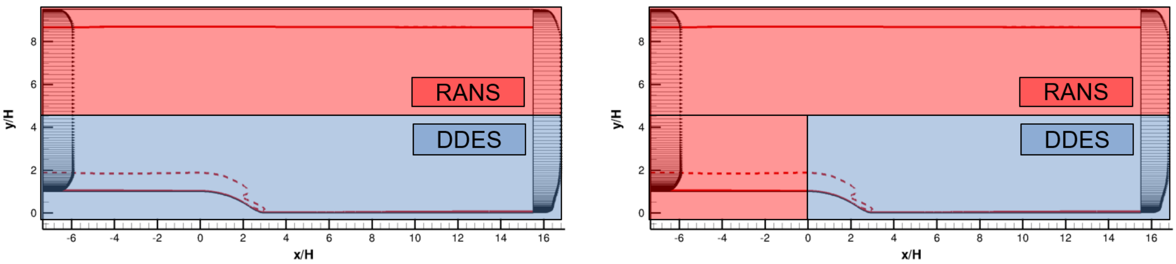

(a) Non-zonal rounded step setup

(b) Semi non-zonal rounded step setup

Figure 3.1: Rounded step test setups used in this brief study

3.3.1. Non-zonal use of σ-DDES with $\tilde{\Delta}_\omega$

In this section, the performance of $\sigma-$DDES with $\tilde{\Delta}_\omega$ in a non-zonal manner is assessed. Since no synthetic turbulence is used in this non-zonal assessment, the shielding function is kept active to shield the attached boundary layer, preventing Modeled stress depletion (MSD). The non-zonal approaches rely on the shielding/ delay function to automatically recognize detached boundary layers, increasing its value from zero to around one, which would decrease the hybrid length scale, and hence the turbulent viscosity. Such reduction in turbulent viscosity is desirable since it makes it possible to resolve the turbulent structures in detached boundary layers. In this case, due to the shallow APG-induced separation, it is not guaranteed to obtain such ideal behavior.

The shielding function f_d in the whole computational field is shown in Figure 3.2a. Note, the upper wall is predefined to be treated by RANS, and thus the shielding function is null in the boundary layer of the upper wall. It was observed that the shielding is so strong that it remains active even over the rounded step region, where the flow is separated, as shown in Figure 3.2a. As a result, the majority of the boundary layer remains treated by the underlying SA RANS model. Such strong shielding will hinder the effectiveness of the $\sigma-$ model since it will obstruct its activation over the rounded step. As given by Equation 3.7, f_d values that are close to zero result in the differential operator maintaining its RANS value, meaning, $\mathcal{D}_{\sigma-DDES} \approx \mathcal{D}_{\mathrm{RANS}}$. This is evident in the turbulent viscosity field shown in Figure 3.2b.

Figure 3.2b shows the ratio between the turbulent and the laminar viscosity using $\sigma-$DDES with $\tilde{\Delta}_{\omega}$. Indeed, the strong shielding over the initial part of the rounded step region results in large turbulent viscosity levels, similar to that produced by the RANS model on the upper wall. The ideal behavior of f_d, in this case, would have been to shield the attached boundary layer and treat it by RANS while quickly decreasing the shielding to only the inner part of the boundary layer in the rounded step region. However, f_d did not exhibit this behavior, as the decrease in shielding took place later than desired.

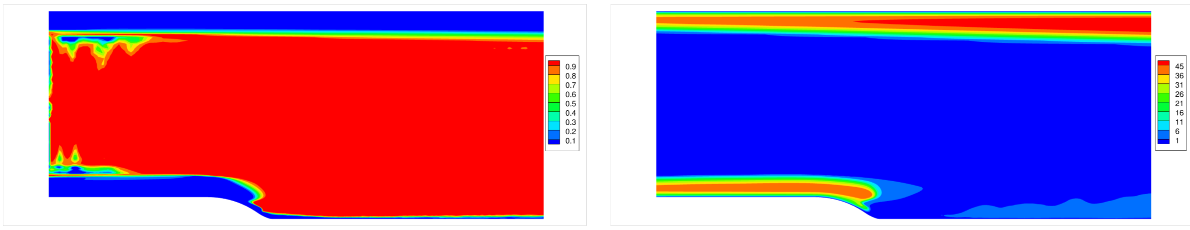

(a) f_d

(b) ν_t/ν

Figure 3.2: Shielding/ delay function used in DDES f_d (left) and ν_t/ν computed using $\sigma-$DDES with $\tilde{\Delta}_{\omega}$ (right)

Even though it may seem logical to deactivate the shielding function to resolve the issue of treating the majority of the separated boundary layer by RANS, this could be more problematic and has to be handled properly. Furthermore, deactivating the shielding function would require a zonal treatment, which is not aligned with the intent of the $\sigma-$DDES formulation, yet still explored in this work. Such zonal treatment could be achieved by either injecting synthetic turbulence (see section 9.2) or by manually predefining the regions treated by RANS and the ones treated by LES. The latter is explored in the next section.

Instead, in this section, two different approaches were considered, aiming at reducing the strength of the shielding. More specifically, the intent of these two approaches is to limit the effect of the shielding function to the inner part of the boundary layer in the rounded step region. The first approach is to decrease the strength of the shielding by setting the coefficient c_d to its original value of 8 (see Equation 2.4). The second approach is to use the Vortex Tilting Measure (VTM) to further decrease the eddy viscosity. The result of these two approaches along with the standard $\sigma-$DDES with $\tilde{\Delta}_{\omega}$ and the standard SA-DDES are shown in Figure 3.3 and Figure 3.4

In the attached boundary layer region upstream of the rounded step, there is no difference between the different explored approaches, as shown in Figure 3.3. This is expected since the attached boundary layer is treated in its entirety by SA-RANS, regardless of the subgrid length scale Δ, and the SGS model. As a result, there is no resolved turbulence, and the Reynolds stresses are completely modeled, as shown in Figure 3.3b, and Figure 3.3c. The region around the rounded step is of more interest. Figure 3.4f shows the shielding function using the aforementioned different approaches. Even though the two proposed approaches result in a faster switching from RANS ($f_d = 0$) to LES ($f_d = 1$), the switching is not sufficiently fast. This can be seen at the locations $x/H = 0.5$ and 1.5, where the shielding function maintains the RANS mode ($f_d = 0$) for the majority of the boundary layer. As a result, the advantageous characteristics of the σ model and $\tilde{\Delta}_{\omega}$ subgrid length scale cannot be fully exploited.

The iso-surfaces of Q-criterion for the aforementioned computations are shown in Figure 3.5. When using SA-DDES, structures similar to that obtained with URANS appear just downstream of the rounded step. Such cylinder-like structures are not to be confused with proper turbulent structures. When σ-DDES is used, turbulent structures that are more physical appear, as shown in Figure 3.5b to Figure 3.5d. In particular, with the two approaches of decreasing c_d and using VTM, the decreased shielding seems to accelerate the development of turbulent structure, as shown in Figure 3.5c and Figure 3.5d. In these two cases, turbulent structures appear more upstream compared to the standard $\sigma-$DDES with $\tilde{\Delta}_{\omega}$. Nonetheless, there is a clear lack of sufficient turbulent structures in all computations. This is due to the lack of sufficient natural instabilities that cannot be provided by such a shallow separation.

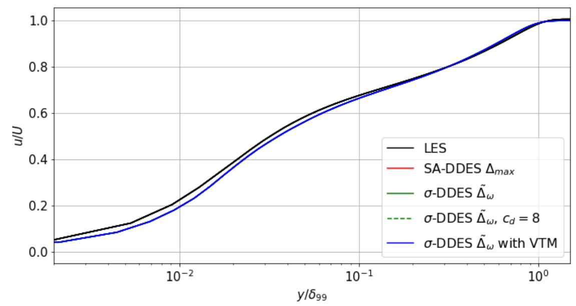

(a) u at the first location

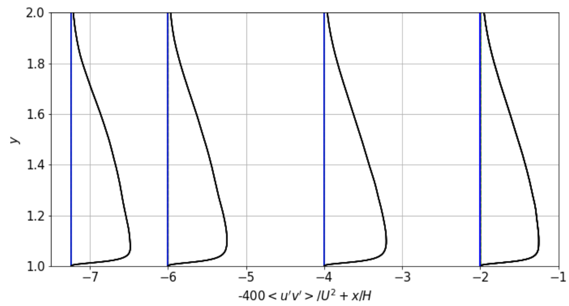

(b) Resolved $<u'v'>$

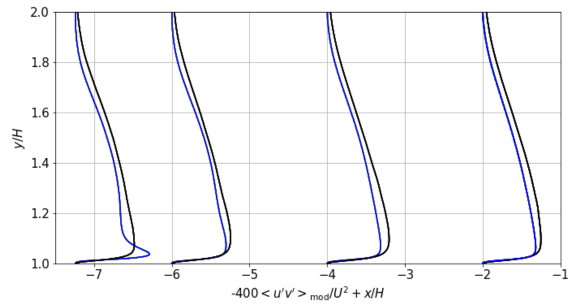

(c) Modeled $<u'v'>$

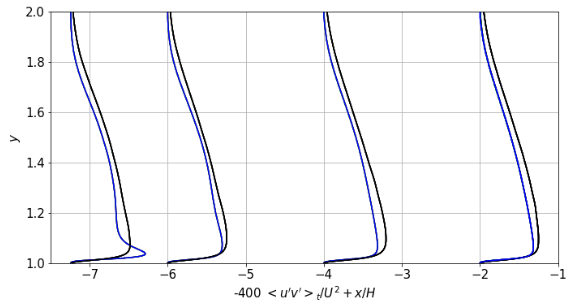

(d) Total $<u'v'>$

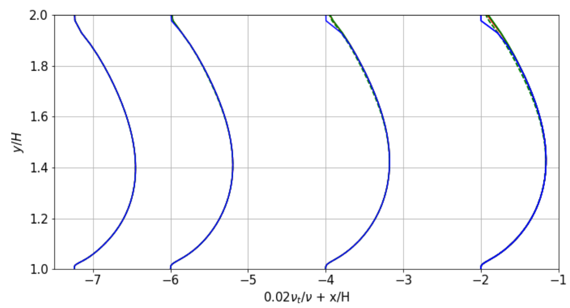

(e) ν_t

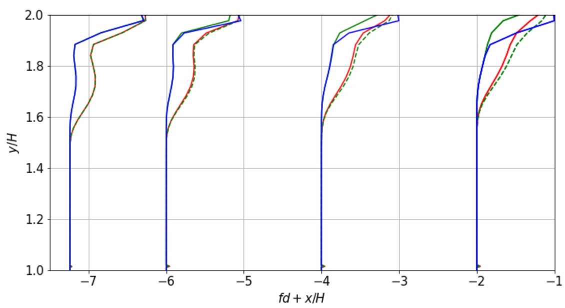

(f) Shielding function f_d

Figure 3.3: Results of using σ-DDES with $\tilde{\Delta}_\omega$ in a non-zonal manner in the upstream region

The mean surface quantities are shown in Figure 3.6. All the computations fail to capture the correct location of separation and reattachment, as shown in Figure 3.6a. It is interesting to see that using σ-DDES with $\tilde{\Delta}_\omega$, especially combined with VTM and $c_d = 8$, shows a closer agreement with the reference C_f data far downstream of the reattachment. A similar behavior is observed with the pressure coefficient shown in Figure 3.6b. This is in agreement with the results of Q-criterion. This reinforces the idea that only with an appropriate rapid switching between the upstream RANS and the downstream LES, the advantageous characteristics of σ-DDES with $\tilde{\Delta}_\omega$ can be exploited.

It is then instructive to investigate the following scenario: Had the shielding been less strong or even absent, would the σ-DDES with $\tilde{\Delta}_\omega$ have shown better performance? This scenario is explored in the next section.

3.3.2. Semi non-zonal use of σ-DDES with $\tilde{\Delta}_\omega$

To properly assess the performance of σ-DDES with $\tilde{\Delta}_\omega$, in terms of detecting quasi-2D flows and adjust the eddy viscosity levels accordingly, the strong shielding observed with the f_d function needs to be decreased or eliminated. In an attempt to prevent this shielding from obstructing the activation of σ-DDES with $\tilde{\Delta}_\omega$, a "semi non-zonal" setup was analyzed. That is, the upstream attached boundary layer was manually predefined to be treated by RANS, whereas the rounded step region was treated by

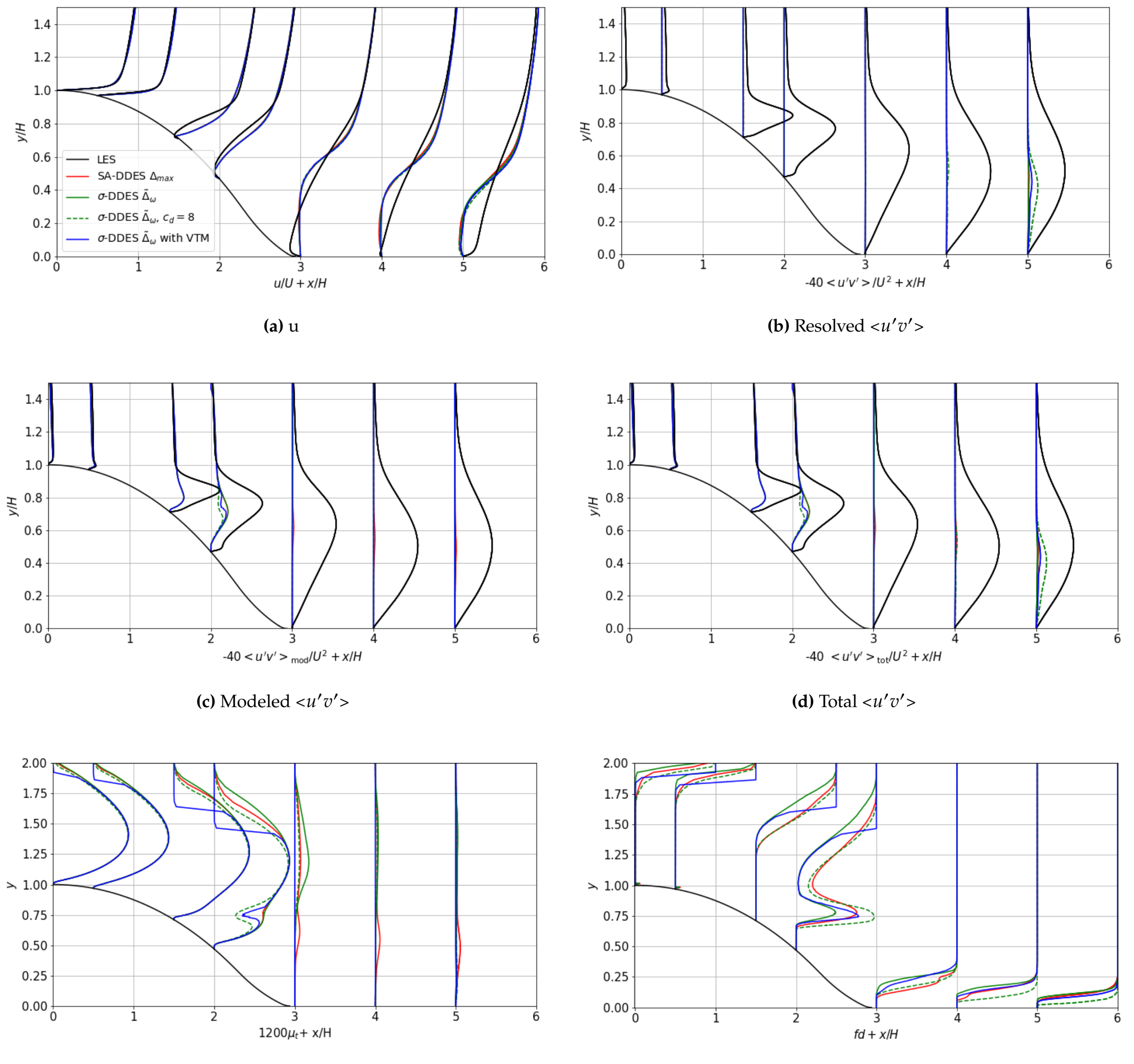

(a) u **(b)** Resolved $<u'v'>$

(c) Modeled $<u'v'>$ **(d)** Total $<u'v'>$

(e) ν_t **(f)** Shielding function f_d

Figure 3.4: Results of using σ-DDES with $\tilde{\Delta}_\omega$ in a non-zonal manner in the rounded step region

σ-DDES with a modified shielding function. In this manner, it is ensured that the shielding function can no longer delay the activation of the σ- model and $\tilde{\Delta}_\omega$, which allows for a fair assessment of their performance. The test setup is shown in Figure 3.1b. The modified shielding function considers only the viscous part of the original f_d function, and reads

$$f_{d_{\text{visc}}} = 1 - \tanh\left[(8r_{visc})^3\right] \tag{3.8}$$

with r_{visc} considering only the viscous component as follows:

$$r_{\text{visc}} = \frac{\nu}{\kappa^2 d_w^2 \max\left(\sqrt{\frac{\partial U_i}{\partial x_j}\frac{\partial U_i}{\partial x_j}}; 10^{-10}\right)} \tag{3.9}$$

The results of the "semi non-zonal" computation along with the two explored approaches in the typical non-zonal $\sigma-$DDES with $\tilde{\Delta}_\omega$ setups are shown in Figure 3.7. Figure 3.7f shows the modified shielding function $f_{d_{\text{visc}}}$ compared to the standard shielding function f_d. Indeed, the modified shielding function switches quickly from RANS in the near-wall region to LES in the rest of the boundary layer. However, this switching takes place very close to the wall, it is almost as if there is no shielding at all. This is evident

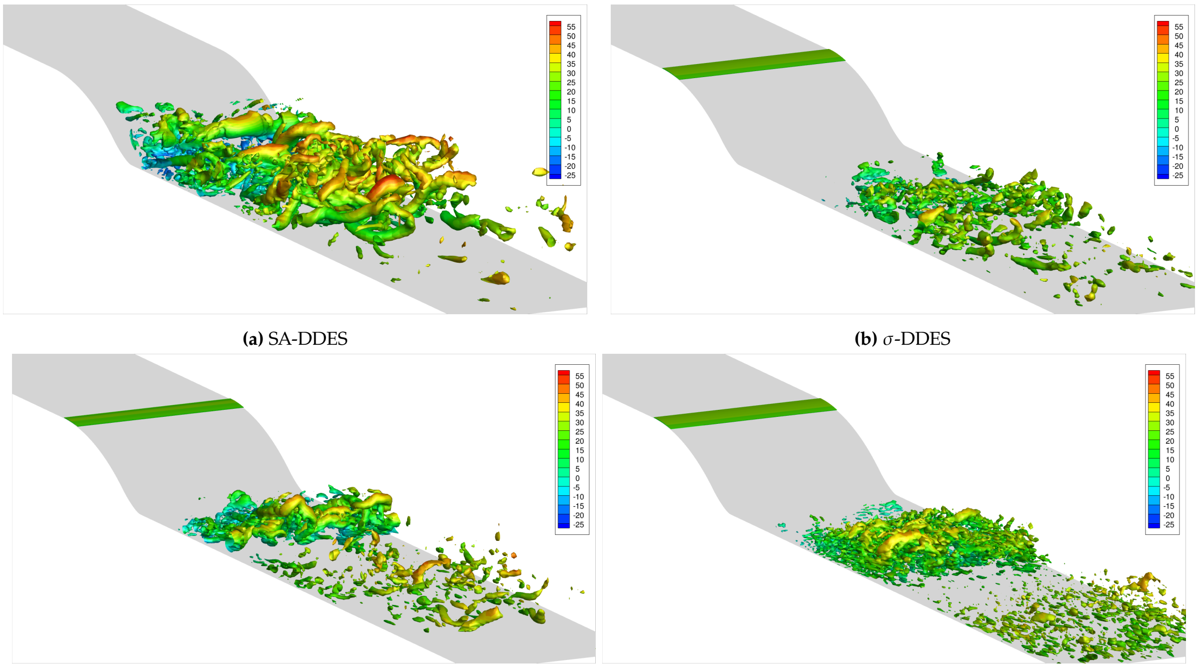

(a) SA-DDES

(b) σ-DDES

(c) σ-DDES with $c_d = 8$

(d) σ-DDES with VTM

Figure 3.5: Iso-surfaces of Q-criterion ($Q = 2U^2/H^2$), colored by the streamwise velocity for the rounded step case

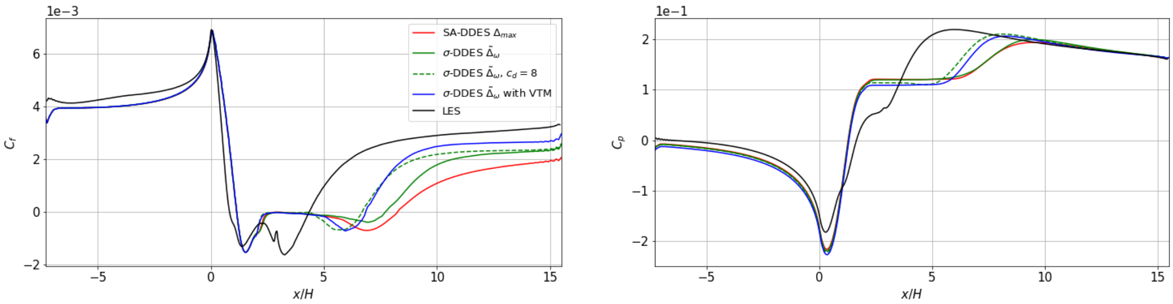

(a) C_f

(b) C_p

Figure 3.6: Skin friction and pressure coefficient using σ-DDES with $\tilde{\Delta}_\omega$ in a non-zonal manner

in the eddy viscosity, shown in Figure 3.7e, where there is some eddy viscosity at $x/H = 0$, convected from upstream, which quickly disappears downstream. While the large eddy viscosity maintained by the original shielding function is unfavorable, the absence of eddy viscosity is problematic. Even though resolved turbulent shear stress can be observed with the modified shielding function in the "semi non-zonal" setup, the velocity profiles are completely unrepresentative of the flow, as shown in Figure 3.7b and Figure 3.7a, respectively. These results are not encouraging, and they illustrate the limitations of non-zonal approaches in flow cases with shallow separation.

The skin friction and the pressure coefficient are shown in Figure 3.8. Figure 3.8a shows unsatisfactory results in terms of the location of separation and reattachment, even when the modified shielding function was used in the "semi non-zonal" setup. Regarding the "semi non-zonal" setup, the sudden decrease of eddy viscosity, with a lack of resolved turbulence content, has shown to be problematic. In fact, this is the very issue this work is focused on, the grey area problem.

From this brief study, it can be concluded that non-zonal approaches are limited in terms of the type of flows they can accurately predict. As illustrated in this brief study, non-zonal methods struggle in flows with shallow pressure-induced separations. To achieve improvement in non-zonal methods, faster switching between the RANS and the LES region, while still shielding the inner part of the boundary

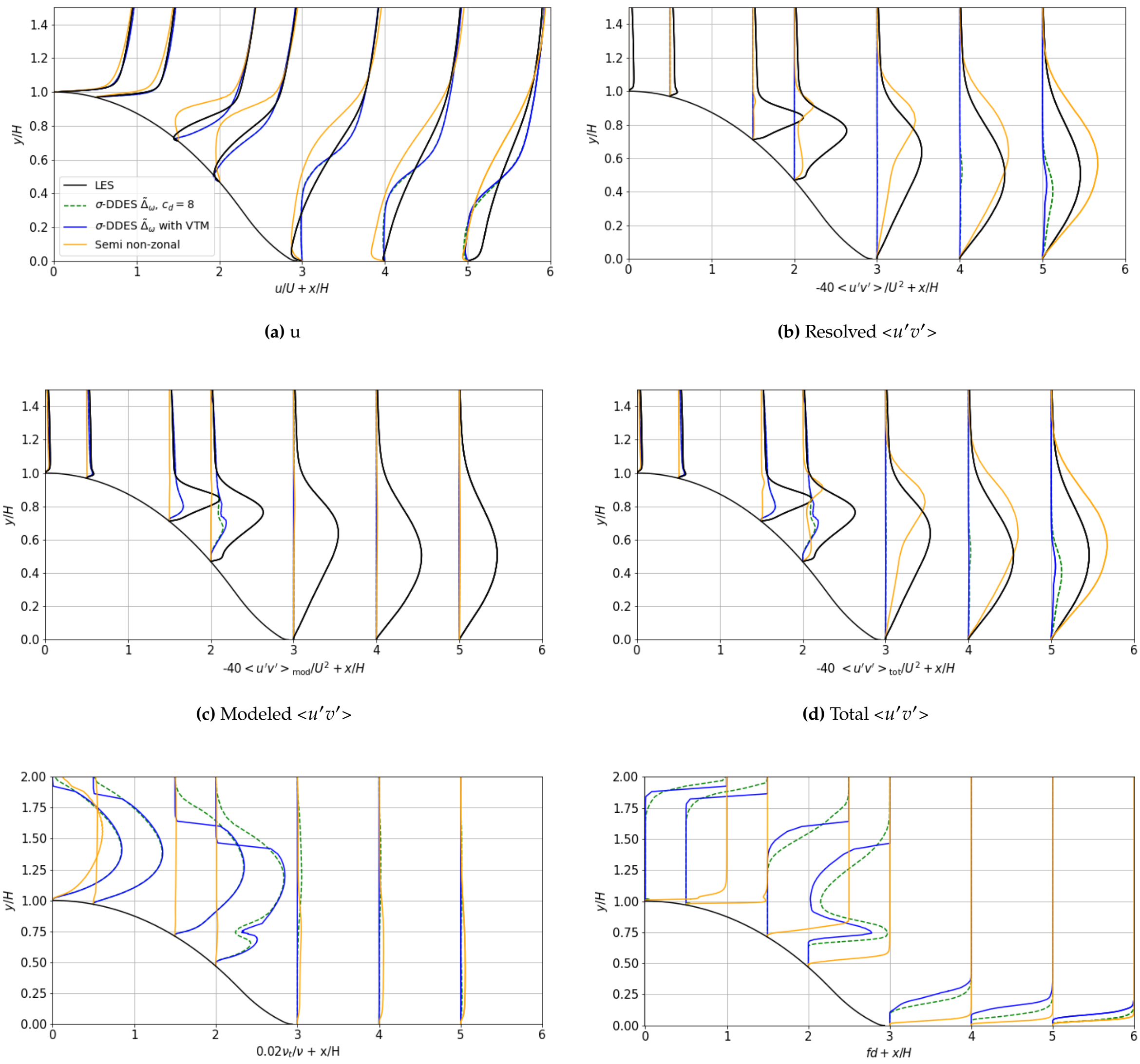

(a) u

(b) Resolved $<u'v'>$

(c) Modeled $<u'v'>$

(d) Total $<u'v'>$

(e) ν_t

(f) Shielding function f_d

Figure 3.7: Results of using σ-DDES with $\tilde{\Delta}_\omega$ in a non-zonal and "semi non-zonal" manner in the rounded step region

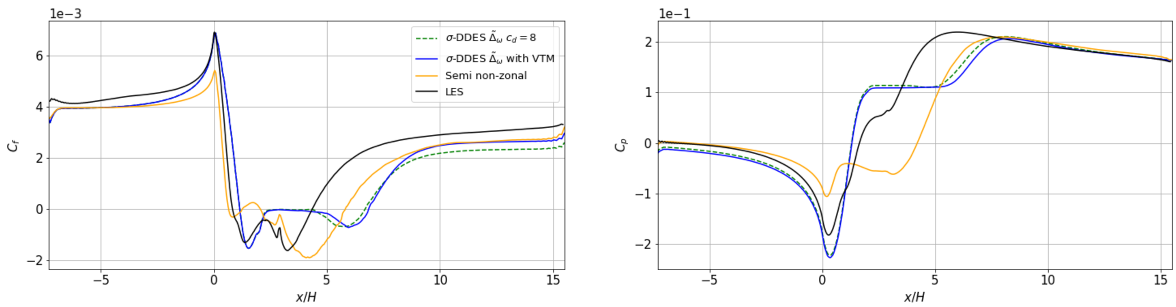

(a) C_f

(b) C_p

Figure 3.8: Skin friction and pressure coefficient using σ-DDES with $\tilde{\Delta}_\omega$ in a non-zonal and "semi non-zonal" manner

layer, is needed. The current shielding function f_d fails in this aspect, as it is not sensitive to shallow separation. To make use of the advantageous characteristic of σ-DDES and $\tilde{\Delta}_\omega$, a new shielding function is needed. Developing a less conservative shielding function could be an interesting area of research, however not addressed in this work. Even with such an improved shielding function, the performance of non-zonal methods could still remain dependent on the flow case and the instabilities of the free shear layers. For this reason, this work focuses on zonal methods instead, in particular embedded WMLES methods, where synthetic turbulence is used to provide turbulent content.

4
Zonal Approaches: Research Focus and Activities

In this chapter, different aspects of the research activities are presented. First, the different aspects of the research are stated, and the research questions are presented. Then, test cases are described, and the numerical setup is discussed.

As illustrated in chapter 3, non-zonal methods are limited to massively separated flow, where the natural instabilities can provide sufficient turbulent content for the LES region. For this reason, this work focuses on zonal methods, more specifically embedded WMLES methods, where synthetic turbulence is used to provide the needed turbulent content. In such zonal approaches, the delay in transitioning from fully modeled turbulence in the upstream RANS region to mostly resolved turbulence in the downstream WMLES region is governed by the quality of the injected synthetic turbulence. In such approaches, the transition can be accelerated by improving the synthetic turbulence and the methods used to introduce it into the flow [10]. The research activities can be divided into two categories. The first focuses on the synthetic turbulence and its injection into the flow, whereas the second focuses on the use of σ-DDES and $\tilde{\Delta}_{\omega}$ in an embedded WMLES manner.

4.1. Research objectives and Activities

One main aspect of zonal approaches, when used as embedded WMLES methods (zonal approaches for short), is the synthetic turbulence generation. In this work, the synthetic turbulence generator (STG) of Adamian et al. [12], and its successor NTS-STG of Shur et al. [13] are studied. Both methods are based on the superposition of Fourier modes, such that the statistics of the generated synthetic velocities match the prescribed target Reynolds stresses. To achieve this, both STG variants require random quantities as well as statistical ones as input. The random quantities include the direction vectors and the phase shift of each mode. These random quantities are referred to as the random numbers set hereafter. The statistical quantities are the target Reynolds stresses, which are typically taken from upstream of the RANS-LES interface.

Patterson et al. [16] found that the random number set could have a bias error, which results in a large deviation between the statistics of the synthetic velocities and the target Reynolds stresses. This is mainly because the random number set in both STG variants, unlike in the SEM, is drawn once and kept constant during the whole computation. In this work, the influence of the random number set is assessed by comparing the results of two different realizations of random numbers. The first is drawn randomly from the appropriate density functions, and the second is selected to ensure a small bias error. The a-priori bias error estimation by Patterson et al. [16] are implemented and used to choose the random number set with the least associated bias error. Such set is denoted the selected set in this work. Regarding the target Reynolds stresses, they can be either reconstructed from a RANS solution or obtained from high-fidelity results (DNS or LES). The impact of using each on turbulence development is also evaluated.

Regarding the STG implementation in DLR-TAU, it was found the skin friction results deteriorate after large computational times. This issue is referred to as temporal decay, as an increasing deterioration in the outcome was observed with increasing computational time. The cause of this issue is explored and identified. Furthermore, an assessment of two parameters used in the STG formulation is carried out. These two parameters are the macro-scale velocity and the cut-off frequency.

Another crucial aspect of zonal approaches is the injection of synthetic turbulence. To introduce synthetic turbulence into the flow, source terms are added to the momentum equations. In this work, different forcing methods are evaluated. The performance of two source terms, the DLR source term [14] and the VSTG source term [15], is assessed. To this end, based on the aforementioned aspects, research questions that focus on synthetic turbulence generation and its injection into the flow were identified. These are as follows:

- What are the main parameters that affect the quality of the synthetic turbulence, produced by the STG/ NTS-STG?
- To what extent can the choice of a random number set in the STG decrease the bias errors associated with a specific realization?
- What are the main strengths and shortcomings of different synthetic turbulence forcing approaches?

The research activities focused on the synthetic turbulence generation and its forcing into the flow are shown in Figure 4.1. There are four blocks with grey boxes showing the process of providing the STG with the needed input, generating the synthetic turbulence (ST) using the STG, and computing the statistics of the synthetic velocities. Then, the third block entails injecting this synthetic turbulence into the flow using source terms, and finally obtaining resolved stresses.

In this work, the research activities follow a systematic step-wise approach in which sources of error are identified and eliminated to avoid error accumulation. Starting with the ST generation block, an improvement to the synthetic turbulence is needed to address the temporal decay issue, which is discussed in chapter 5. In the same chapter, two important aspects of the STG formulation, the macro-scale velocity and the cut-off frequency, are analyzed. Secondly, to identify the most influential factors affecting the quality of the generated synthetic turbulence, a sensitivity analysis of the STG input is carried out. This is achieved by varying the source of target Reynolds stress and the random number set, as discussed in chapter 6. With the improved synthetic turbulence at hand, its injection into the flow is addressed by evaluating different source terms. The DLR source term [14] and the VSTG [15] are assessed, where the strengths and shortcomings of each are identified. Two modifications to address these shortcomings, namely the constrained forcing and the dynamic forcing, are proposed.

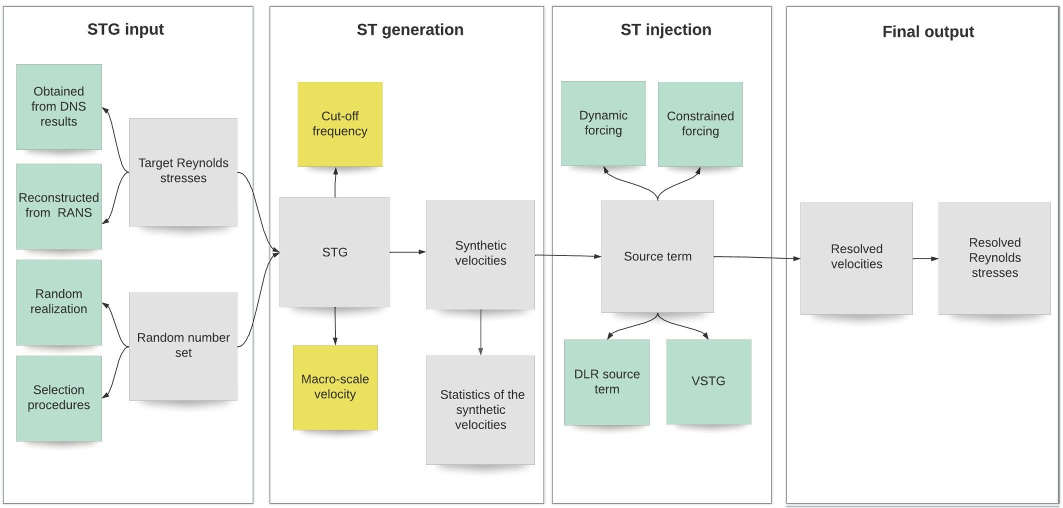

Figure 4.1: Research activities focused on the synthetic turbulence generation and its injection methods

Additionally, the WMLES capabilities of σ-DDES with $\tilde{\Delta}_\omega$ are evaluated. This is motivated by the statement of Fuchs et al. [21], however, not much evidence was provided in their publication. This aspect is assessed in two manners. The first is by providing an unsteady turbulent solution and observing whether σ-DDES with $\tilde{\Delta}_\omega$ would drive the solution to a RANS-like solution or maintain its unsteadiness. The second is to use σ-DDES with $\tilde{\Delta}_\omega$ in an embedded WMLES setup along with synthetic turbulence.

The premise is that the decreased SGS viscosity levels could allow synthetic turbulence to rapidly develop into physical turbulence, decreasing adaptation lengths. To this extent, the research questions focusing on $\tilde{\Delta}_{\omega}$ and $\sigma - DDES$, are as follows:

- To what extent can σ-DDES with $\tilde{\Delta}_{\omega}$ function as a WMLES method?
- To what extent can the use of σ-DDES with $\tilde{\Delta}_{\omega}$ as an embedded WMLES method accelerate the RANS to LES transition?

The research activities focused on the WMLES capabilities of σ-DDES with $\tilde{\Delta}_{\omega}$ are presented in chapter 9.

4.2. Test Cases

In this work, three test cases were used, each serving a specific purpose. The test cases are a zero-pressure gradient (ZPG) flat plate, an adverse-pressure gradient (APG) separation in a rounded step, and a periodic channel flow. In this section, the different test cases are described.

4.2.1. Flat plat test case

A spatially developing zero-pressure-gradient (ZPG) boundary layer over a flat plate is a standard test case in HRLM studies. In this work, a boundary layer with a zero-thickness at the inflow is considered. The free-stream velocity is U = 70 m/s, the static pressure is set to P = 99120 Pa, and the temperature equals 287 K, resulting in a Reynolds number per meter Re = 4.72×10^6 m^{-1} and a Mach number $M_0 = 0.2$.

The interface from SA-RANS to WMLES takes place at $Re_{\theta} = 3040$, corresponding to $x = 0.3517$. This location has a boundary layer thickness $\delta_0 = 0.0058m$ and is used as the origin of a local coordinate system $x/\delta_0 = 0$. The Reynolds numbers based on the momentum thickness θ_0 and the friction velocity u_{τ_0} at x/δ_0 are respectively:

$$Re_{\theta_0} = \frac{U_0\theta_0}{v} = 3040$$

$$Re_{\tau_0} = \frac{u_{\tau_0}\delta_0}{v} = 1065$$

The hybrid grid of Probst et al. [22] was used, which contains $5.8 \cdot 10^6$ grid points in the WMLES region. This grid ensures $\Delta x^+ \approx 100 - 200$, $\Delta y^+ \approx 1, \Delta z^+ \approx 50$, and is similar to the structured grid used in [14]. Note, mesh cells are stretched for $x/\delta_0 > 77$, in order to gradually dampen the turbulent fluctuations. This procedure is standard practice in HRLM studies to ensure that the region of interest is free of wave reflections. The whole grid, both the upstream RANS region and the WMLES region, is shown in Figure 4.2. The time step is $\Delta = 8 \times 10^{-7}$ s, and normalized in wall units is $\Delta t^+ \approx 0.4$.

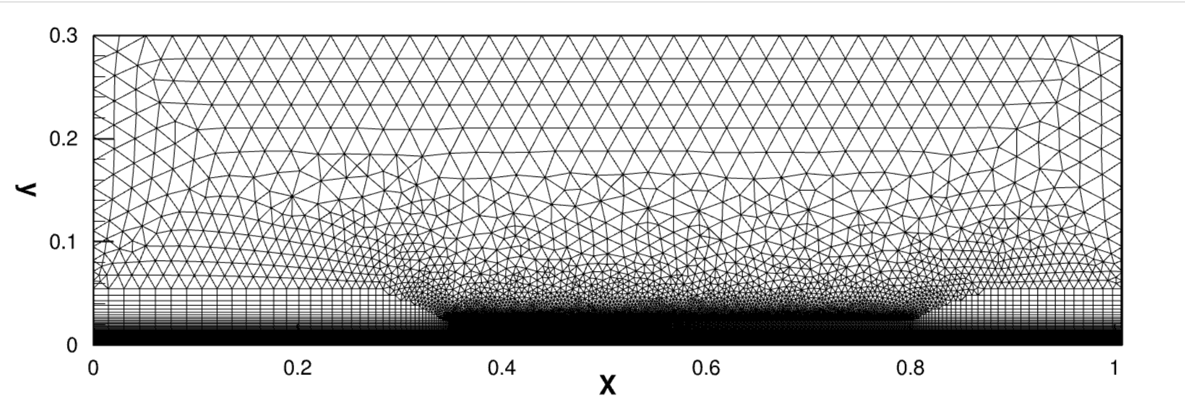

Figure 4.2: Flat plate test case grid

The reference Reynolds stresses are the target Reynolds stressed used by the synthetic turbulence generator, which are reconstructed from a precursor RANS solution. The method M2 of Laraufie et al. [23], which is based on Wilcoox's hypothesis, was used to obtain the Reynolds stress tensor using the velocity and the eddy viscosity profiles. The reference skin friction coefficient is based on the widely acknowledged Coles-Fernholz correlation [24], which reads:

$$C_f^{CF} = 2\left(\frac{1}{0.384}\ln\left(\mathrm{Re}_\theta\right) + 4.127\right)^{-2} \tag{4.1}$$

Using the flow conditions, this correlation was adapted by [22] to provide a relation between C_f and the local coordinate system x/δ_0.

4.2.2. Rounded step test case

The rounded step is a shallow separation test case, studied by Bentaleb et al. [25] using highly-resolved LES. An expansion of $1H$, the step height, leads to pressure-induced separation and subsequent re-attachment. The Reynolds number, based on H and the inlet free-stream velocity U_{in}, is 13700. The inlet is located at $x/H = -7.34$, at which the momentum-thickness Reynolds number is $Re_\theta = 1190$, and the boundary layer thickness is $\delta_{99} = 0.80H$. In this test case, only the lower wall was treated by HRLM, while the upper wall was treated by pure SA-RANS. The synthetic turbulence injection take place at the inlet, as the whole lower wall is treated by HRLM. The baseline setup is shown in Figure 4.3.

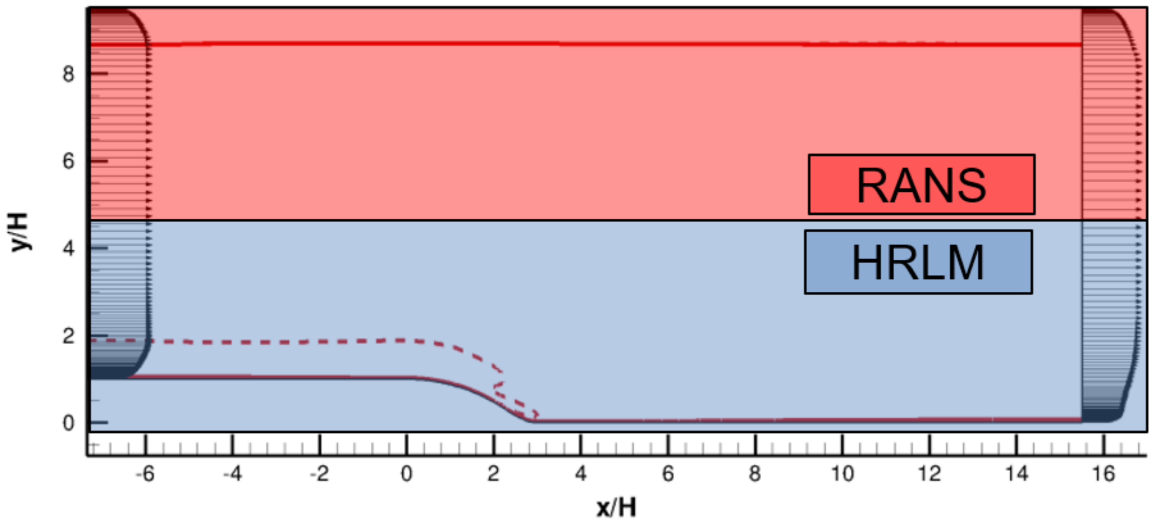

Figure 4.3: Standard rounded step test case setup

The step geometry is defined as follows:

$$\begin{aligned} y_{\mathrm{wall}} &= (1 - R_1) + \sqrt{R_1^2 - x^2} && \text{for} \quad 0 < x/H < 2.3 \\ y_{\mathrm{wall}} &= y_2 - \sqrt{\frac{R_1^2}{4} - (x_2 - x)^2} && \text{for} \quad 2.3 < x/H < 2.835 \\ y_{\mathrm{wall}} &= R_2 - \sqrt{R_2^2 - (3 - x)^2} && \text{for} \quad 2.835 < x/H < 2.937 \end{aligned} \tag{4.2}$$

with $R_1 = 4.03$, $R_2 = 0.333$, $x_2 = 3.449$ and $y_2 = 1.936$.

The hybrid grid of [26] was used. The grid consists of two structured blocks, separated by a prisms block as shown in Figure 4.4. The structured WMLES block is of interest, which contains $350 \times 96 \times 64$ points. In this block, the streamwise spacing varies such that $\Delta x/H = 0.1$ at the inlet, $\Delta x/H = 0.042$ in the separation region ($x/H = 0 - 5$), and $\Delta x/H = 0.15$ at the outlet. Furthermore, it is ensured to maintain $y^+ \approx 1$, with a stretching factor of 1.05 in the WMLES block.

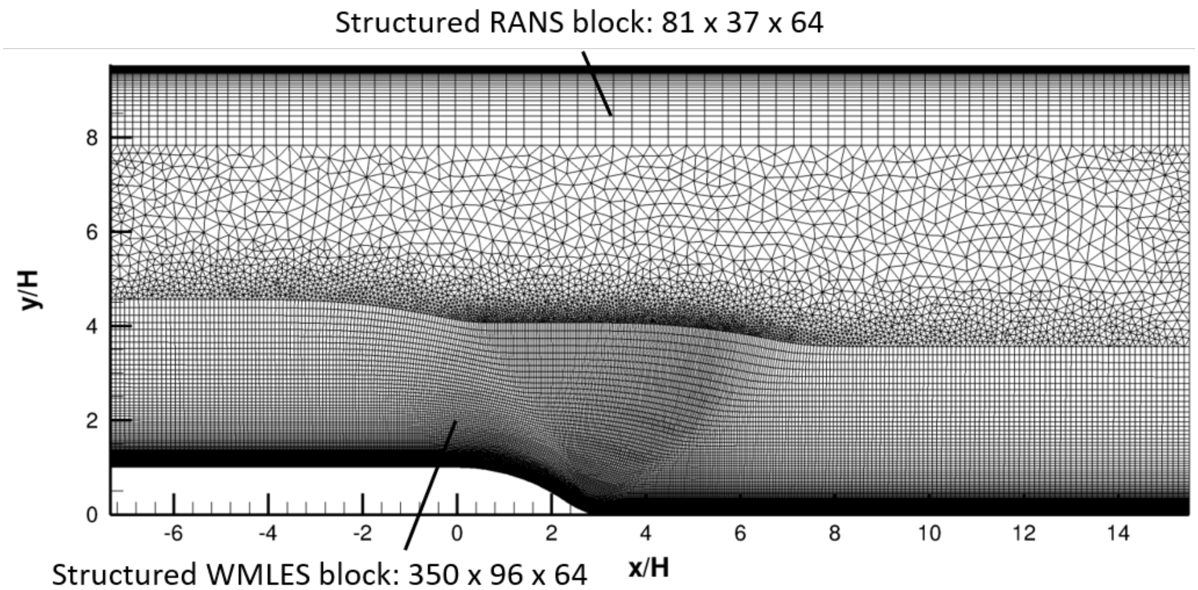

Figure 4.4: Rounded step test case grid

4.2.3. Channel flow test case

Periodic channel flow is a standard test case in HRLM studies. In this work, a channel flow at $Re_\tau \approx 4200$ is used. The channel has a height of 2δ, a length of $2\pi\delta$, and a width of $\pi\delta$, where δ is the channel half-height. The free-stream velocity is U = 50 m/s, and the temperature equals 287 K, resulting in a Reynolds number based on δ $Re_\delta = 98300$ and a Mach number M = 0.15. The reference data for this test case is the DNS data of Lozano-Durán et al. [27].

The grid is that used by Probst et al. [28], containing $65 \times 101 \times 65$ grid points. This grid has a constant wall-tangential spacing of $\Delta x^+ = 416$ and $\Delta z^+ = 206$, with $y^+ = 0.8$ and a wall-normal stretching factor equal to 1.14. The grid is shown in Figure 4.5. The time step is $\Delta = 4.5 \times 10^{-5}$ s, and normalized by wall units $\Delta t^+ = 0.4$. The whole domain is treated by HRLM.

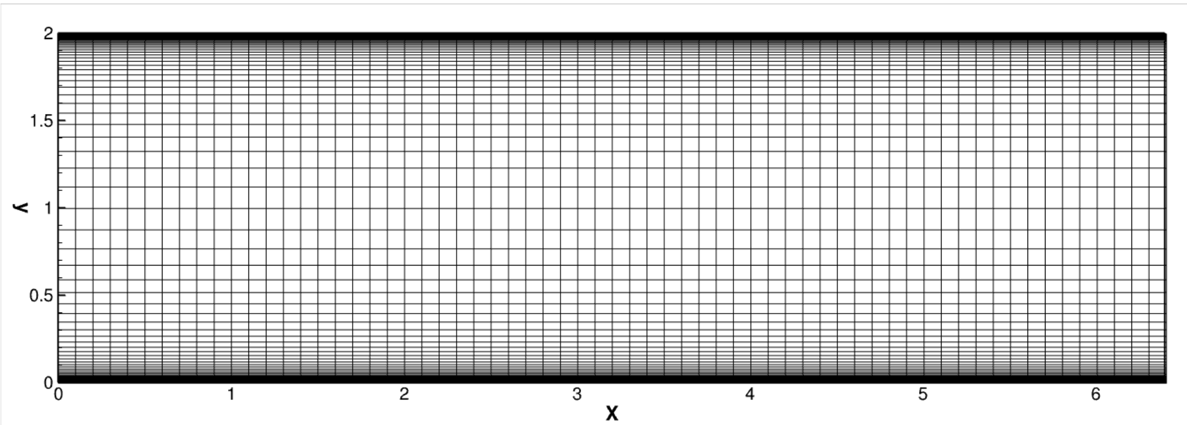

Figure 4.5: Channel flow test case grid

4.3. Numerical Setup

This work was performed using the German aerospace agency compressible solver DLR-TAU. DLR-TAU is an unstructured compressible finite-volume solver. It uses 2nd-order spatial and temporal discretization schemes, along with low-Mach number preconditioning for incompressible flows [29]. The inviscid fluxes are based on the LD2 scheme, which is a low dissipation, low dispersion scheme suitable for scale-resolving simulations [30].

In IDDES simulation, the WMLES branch of IDDES is always enforced by setting $f_{dt} = 1$. This procedure is also followed in [22]. In this work, SA is used as the default underlying RANS model. Furthermore, NTS-STG of Shur et al. [13] is used as the default synthetic turbulence generator, and the DLR source term of Probst [14] is the default forcing term to inject the synthetic turbulence into the flow. These default parameters are always used, unless explicitly stated otherwise.

5
Synthetic Turbulence Generation

In this chapter, synthetic turbulence generation methods are discussed. The synthetic turbulence generator (STG) that was proposed by Adamian et al. [12] as well as a similar STG (NTS-STG), proposed by Shur et al. [13], are studied. Two important aspects of their formulations are analyzed. Furthermore, recommendations to ensure the quality of synthetic turbulence are provided.

The STG of Adamian et al. [12] is already implemented in DLR-TAU, and thus referred to as the original STG hereafter. NTS-STG is a new variant of the original STG, with the only difference being in the time-dependent term in Equation 5.1. Both the original STG and NTS-STG are synthetic turbulence methods based on the superposition of random Fourier modes. In both formulations, the synthetic velocities are defined such that their second-order moments at the RANS-LES interface/inflow are equal to the prescribed target Reynolds stress tensor. This is achieved by superimposing a fixed number N of spatiotemporal Fourier modes. In the original STG formulation, this reads as follows[12]:

$$u'_{s_i} = a_{ij} 2\sqrt{\frac{3}{2}} \sum_{n=1}^{N} \sqrt{q^n} \sigma_j^n \cos\left(\kappa^n d_l^n x_l + \psi^n + S^n \frac{t}{\tau}\right) \tag{5.1}$$

with a_{ij} being the Cholesky decomposition of the Reynolds stress tensor $a_{ik}a_{jk} = R_{ij}$, τ is a timescale, and the random quantities are described as follows:

$$\sigma^n = \sigma^n\left(\theta^n, \phi^n\right), \quad \sigma_j^n d_j^n = 0, \quad d_i^n = d_i^n\left(\theta^n, \phi^n, \eta^n\right). \tag{5.2}$$

Here Einstein notation is used where the contraction is between spatial dimensions (subscripts), and a sum symbol is used to sum over the Fourier modes.

q^n is the normalized amplitude of mode n, and κ^n is the amplitude of the wave number vector of the mode n. The terms θ^n, ϕ^n, η^n, and ψ^n are sets of random variables defined by their probability density functions and intervals. The two random sets of spherical angles $\theta^n$and ϕ^n result in the unit vectors σ_j^n being uniformly distributed over a unit sphere. A divergence-free velocity is imposed ($\sigma_j^n d_j^n = 0$) together with the requirement that d_j^n is also uniformly distributed over a unit sphere. This results in d_j^n being a function of σ_j^n (and therefore $\theta^n$and ϕ^n) and the angle η in the plane perpendicular to σ_j^n. ψ^n is the phase of the mode n. Finally, the last random variable is S^n, which is multiplied by a time-dependent term to add time dependency to the synthetic fluctuations. Note that these random quantities are chosen only once at the start of the computation. One realization of these random quantities will be referred to as the random number set hereafter.

The main difference between the original STG and NTS-STG is the time-dependent term. In NTS-STG formulation, the wave-convection approach was used to add time-dependency to the synthetic fluctuations [13]. The synthetic turbulence field is then computed as follows:

$$u'_{s_i} = a_{ij} 2\sqrt{\frac{3}{2}} \sum_{n=1}^{N} \sqrt{q^n} \sigma_j^n \cos\left(\kappa^n d_l^n \hat{x}_l + \psi^n\right) \tag{5.3}$$

with the modified coordinates given by:

$$\hat{x}_i \equiv \left\{(x_1 - U_0 t)\, \kappa_e^{\min}/\kappa^n, x_2, x_3\right\}, \tag{5.4}$$

U_0 is a macro-scale velocity at the RANS-LES interface, such as the maximum or bulk velocity. In this work, the bulk velocity was used as a macro scale velocity. The macro-scale velocity accounts for the bulk convection of the flow. The normalized amplitudes of each mode are computed as a fraction of the total energy contained in the energy spectrum.

$$q^n = \frac{E(\kappa^n)\,\Delta\kappa^n}{\sum_{n=1}^{N} E(\kappa^n)\,\Delta\kappa^n}, \quad \sum_{n=1}^{N} q^n = 1 \tag{5.5}$$

where $E(\kappa^n)$ is a prescribed turbulent kinetic energy spectrum. Both formulations of the STG use a modified Von Karman spectrum, defined as follows:

$$E(\kappa^n) = (\kappa^n/\kappa_e)^4 f_\eta f_{\text{cut}} \left[1 + 2.4\,(\kappa^n/\kappa_e)^2\right]^{-17/6}, \tag{5.6}$$

where κ_e is the wave number of the most energetic modes, f_η and f_{cut} are empirical functions that modify the energy spectrum. The purpose of the f_η function is to guarantee that the spectrum is dampened around the wave number that corresponds to the Kolmogorov length scale, and reads

$$f_\eta = \exp\left[-\left(12\kappa/\kappa_\eta\right)^2\right], \kappa_\eta = 2\pi/l_\eta \tag{5.7}$$

where $l_\eta = \left(v^3/\varepsilon\right)^{1/4}$ is the Kolmogorov length scale, ε is the turbulence dissipation rate, and ν is the kinetic viscosity. The function f_{cut} damps the energy spectrum at wave numbers larger than the Nyquist value, κ_{cut}, and reads

$$f_{\text{cut}} = \exp\left(-\left[\frac{4\max(k - 0.9\kappa_{\text{cut}}, 0)}{\kappa_{\text{cut}}}\right]^3\right), \kappa_{\text{cut}} = 2\pi/l_{\text{cut}}, \tag{5.8}$$

where l_{cut} is the cut-off length scale and is defined as follows:

$$l_{\text{cut}} = 2\min\left\{\left[\max\left(h_y, h_z, 0.3h_{\max}\right) + 0.1d_w\right], h_{\max}\right\}, \tag{5.9}$$

where h_y, h_z are the local grid steps at the interface, and $h_{\max} = \max\left(h_x, h_y, h_z\right)$.

Two important aspects of the STG/NTS-STG formulation are discussed in the following sections. These are the macro-scale velocity U_0 and the cut-off frequency f_{cut}. Recommendations are provided to ensure high-quality synthetic turbulence in terms of the proper auto-correlation and the correct normalized amplitudes distribution (q_n). All computations in this chapter were performed using the WMLES branch of IDDES with SA as the underlying RANS model. Furthermore, the DLR source term was used as the synthetic turbulence injection method, which is detailed in section 7.1.

5.1. The Macro-scale Velocity

In this section, the first aspect of the STG formulation, the macro-scale velocity, is discussed. The STG performance when using an instantaneous macro-scale velocity instead of a mean one is evaluated. It was found that when the former is used, the results show what is referred to as temporal decay. Temporal decay is a situation in which the quality of the solution deteriorates as the averaging time period over which the solution is averaged increases. To illustrate this issue, Figure 5.1 shows the skin friction coefficient of the flat plate test case, averaged over two different time periods, 3 convective time units (CTU for short) and 7 CTU, where one CTU is equivalent to one domain flow-through. It is apparent that the solution averaged over 7 CTU has a significant reduction in skin friction downstream of the interface and requires a larger adaptation length to reach the reference C_f. Nonetheless, both results show a very larger adaptation length to be with 5% of the reference.

A decline in the quality of the time-averaged solution as the averaging period increases indicates that the instantaneous solution at later time steps is rapidly deteriorating. To further illustrate this point, the Q-criterion was calculated using the instantaneous solutions at computation times of 2 CTU, 7 CTU, 10 CTU, and 12 CTU. The results of the Q-criterion calculation are presented in Figure 5.2, which depicts the Q-criteria at increasing computation times from left to right. The results show that for the two largest computation times, there is a lack of turbulent structures in the immediate vicinity of the interface. Furthermore, the larger turbulent structures vanish immediately downstream of the interface, only to reappear far downstream. These observations are consistent with the C_f results shown in Figure 5.1, where the skin friction coefficient begins to recover approximately $15\delta_0$ downstream of the interface. It should be noted that these results were obtained using the original STG, but the NTS-STG exhibits similar behavior. Therefore, the results are not included here to avoid repetition.

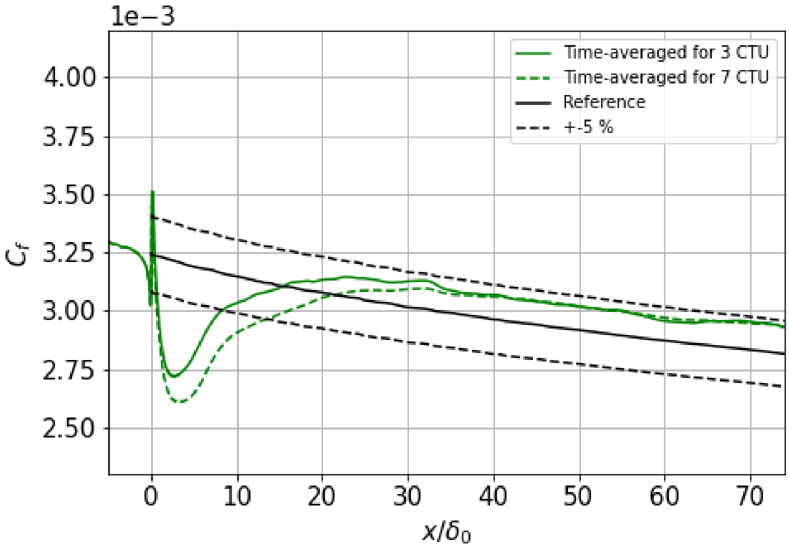

Figure 5.1: Skin friction coefficient of the flat plate case time-averaged for different time periods. Results were obtained using the original STG with instantaneous U_0 and the DLR source term.

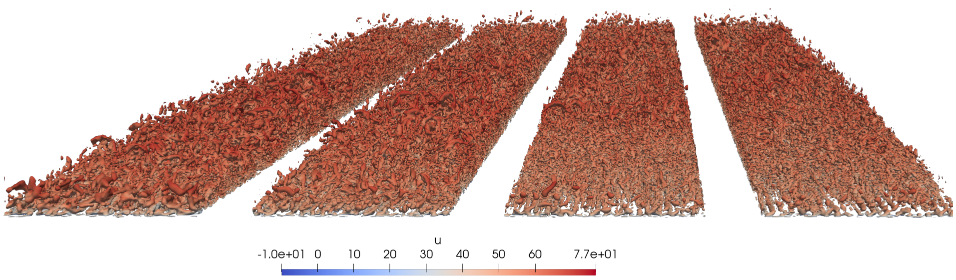

Figure 5.2: Iso-surfaces of Q-criterion ($Q = 1U^2/\delta_0^2$), colored by the streamwise velocity, at increasing computation time from left to right. Results were obtained using the original STG with instantaneous U_0 and the DLR source term.

To understand the mechanism of the temporal decay issue, recall that the macro-scale velocity U_0 appears in the original STG through the timescale τ, and is explicitly used in the NTS-STG in the wave-convection-like approach, as shown in equation Equation 5.4. To demonstrate the impact of using an instantaneous U_0, consider the NTS-STG formulation given in Equation 5.3. Substituting the definition of $\hat{x}_i$ into the synthetic velocity equation results in Equation 5.10. In this relation, U_0 is multiplied by the time to add a time dependency to the generated synthetic velocities.

$$u_s' = a_{1j}\, 2\sqrt{\frac{3}{2}} \sum_{n=1}^{N} \sqrt{q^n}\sigma_j^n \cos\left(d_1^n\,(x_1 - U_0 t)\,\kappa_e^{\min} + \psi^n\right) \tag{5.10}$$

An instantaneous U_0 can be thought of as the sum of a mean component and a fluctuating component. The use of an instantaneous time-varying U_0 leads to an amplification of the fluctuating component as time progresses, resulting in an increasing deviation from the mean U_0. To demonstrate this effect, an instantaneous velocity U_{test} was used as the macro-scale velocity. U_{test} is the sum of the mean U_0 and a time-varying random value drawn from a normal distribution centered around 0. With a different random value drawn at each time step, U_{test} was computed as follows:

$$U_{\text{test}} = U_0(1 + N(0, 0.1)) \tag{5.11}$$

Figure 5.3 compares the effect of using a time-varying macro-scale velocity, represented by U_{test}, with that of using a mean macro-scale velocity. At later times, the random component of the macro-scale velocity is largely amplified, leading to the synthetic velocity approximating a white noise signal. Such a synthetic velocity signal lacks the proper auto-correlation required to represent coherent turbulent structures.
The auto-correlation was calculated using both the mean and the instantaneous macro-scale velocities at a simulation time of 7 CTU. The results of the auto-correlation calculation are depicted in Figure 5.4. The use of the mean U_0 produced auto-correlation coefficients that exhibit the expected behavior, characterized by a starting value of 1 and a gradual decrease as time progresses. In contrast, when the instantaneous U_0 was used, the auto-correlation was significantly distorted, indicating that the generated synthetic velocities were not properly correlated, if at all.

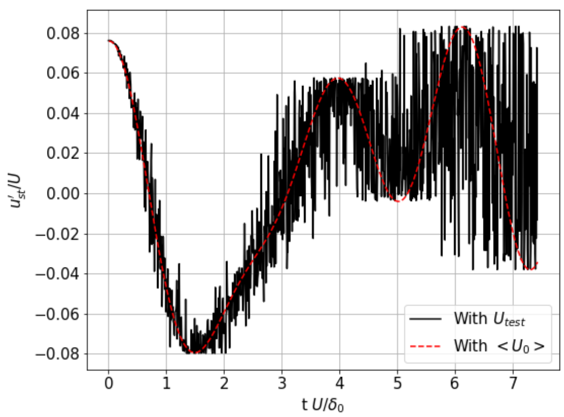

Figure 5.3: Synthetic streamwise velocity with mean U_0 and instantaneous U_0

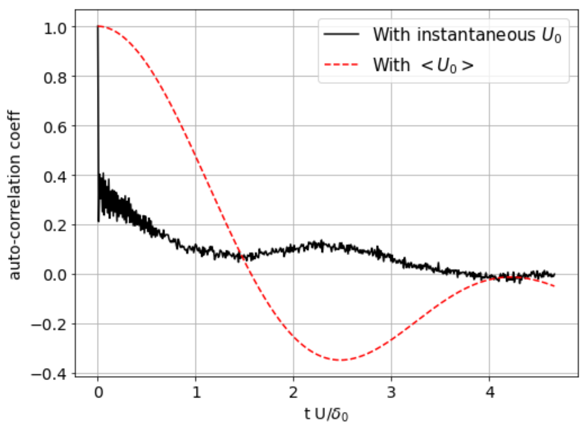

Figure 5.4: Auto-correlation of synthetic streamwise velocity using mean U_0 and instantaneous U_0

Based on this discussion, it is necessary to use the mean macro-scale velocity to avoid deteriorating synthetic turbulence with large computation times. Using the mean macro-scale velocity effectively avoids the temporal decay in both STG formulations. Figure 5.5 shows the skin friction coefficient averaged for 10 CTU, calculated using both the original STG and NTS-STG. As the mean macro-scale velocity is used, further averaging of the solution over extended periods produces minimal changes in the results.

5.2. The Cut-off Frequency

A comparison between the obtained skin friction coefficients in Figure 5.5 and those present in the literature revealed that the skin friction was overestimated, particularly when using the NTS-STG. This deviation was founded to be due to the definition of the cut-off frequency. The previous result used an erroneous definition of f_{cut}. In this section, the effect of using the erroneous definition of f_{cut} is

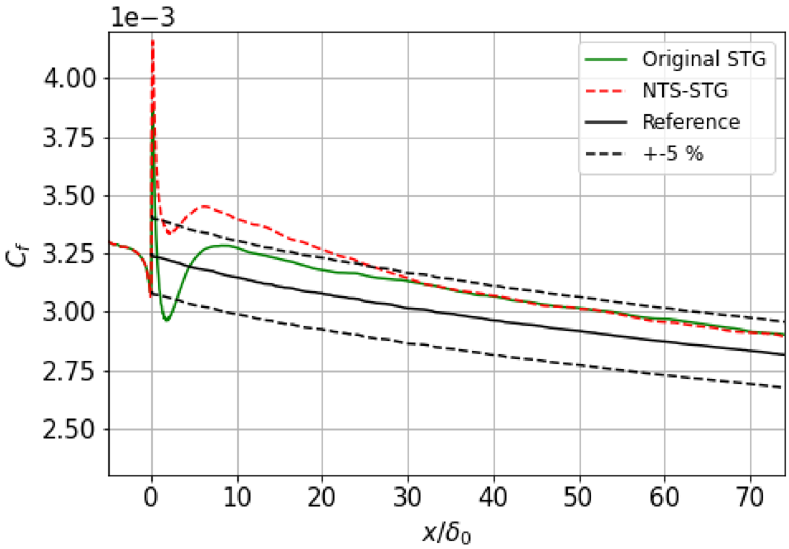

Figure 5.5: Skin friction coefficient of the flat plate case time-averaged for 10 CTU. The results were obtained using the original STG and NTS-STG with the mean U_0 and the DLR source term.

discussed. First, the erroneous definition is a result of a typo in the translated version of the original publication ([12]), and reads as follows:

$$f_{\text{cut erroneous}} = \exp\left(-\frac{\left[4\max\left(k - 0.9\kappa_{\text{cut}}, 0\right)\right]^3}{\kappa_{\text{cut}}}\right) \tag{5.12}$$

It is evident that this definition is wrong, as f_{cut} is a non-dimensional quantity. Figure 5.6a and Figure 5.6b show the erroneous and the correct definition of f_{cut}, respectively. The erroneous f_{cut} abruptly eliminates all modes with $n > 120$, whereas the correct definition transitions gradually from a value of 1 to a value of 0, encompassing modes with $n > 120$ up to $n = N = 136$ near the wall. This is of high significance because f_{cut} determines the energy spectrum, which is used to compute the normalized amplitudes of the different modes, as outlined in Equation 5.5. A comparison between

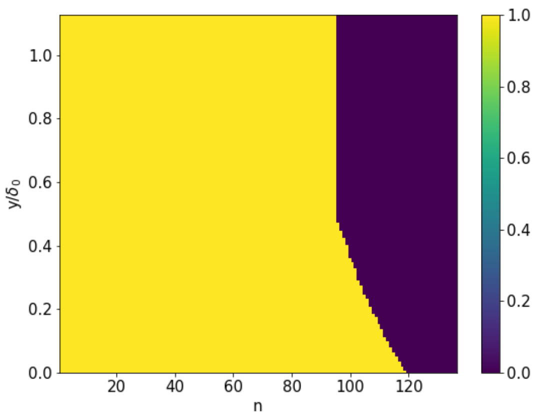

(a) Erroneous f_{cut}

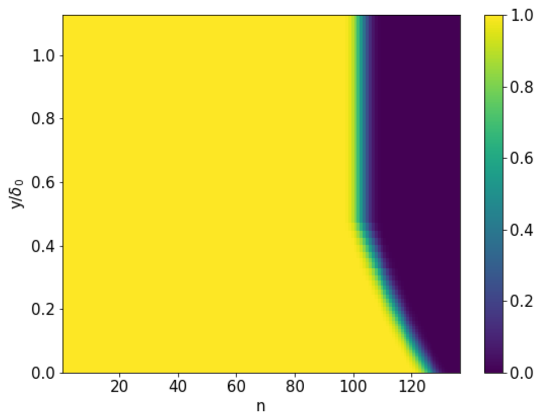

(b) Correct f_{cut}

Figure 5.6: Comparison between the erroneous and the correct f_{cut} for the flat plate test case

the normalized amplitudes using the erroneous and correct definitions of f_{cut} is shown in Figure 5.7a and Figure 5.7b, respectively. The use of the erroneous definition results in modes with $n > 120$ having negligible amplitudes near the wall, while the correct definition allows for proper distribution of amplitudes across all modes. The correct definition ensures that small turbulent structures in the near-wall region have non-zero amplitudes, while larger structures are more prevalent farther away from the wall. This is important, as using normalized amplitudes (q_n) makes the computation of the amplitudes of one mode have a direct impact on the amplitude distribution of the other modes. For example, an error in computing the near-wall amplitudes of certain modes has a cascading effect on the amplitude distribution of the other modes.

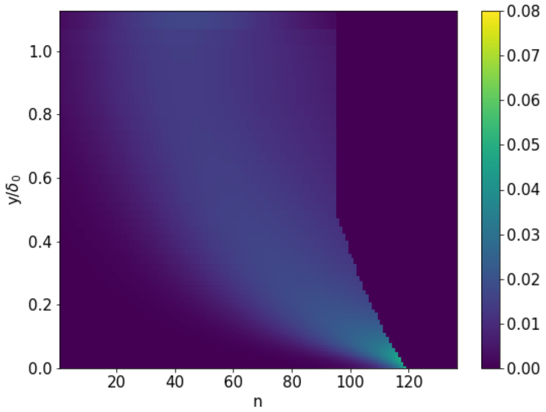

(a) q_n with erroneous f_{cut}

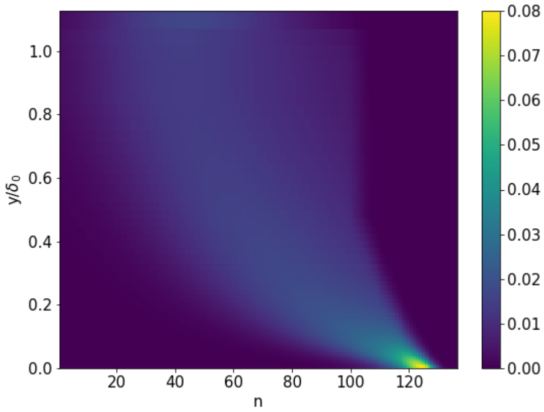

(b) q_n with correct f_{cut}

Figure 5.7: Comparison between the normalized amplitude distribution using the erroneous and the correct f_{cut} for the flat plate test case

Incorrectly assigning zero amplitudes to certain modes leads to a distorted representation of the overall amplitude distribution. This is because the amplitude distribution of the remaining modes gets skewed, causing some of them to have exaggerated amplitude values. The effect of this error can be seen in the normalized amplitude distribution at $y \approx 15\%\delta_0$, as shown in Figure 5.8. As expected, the erroneous assignment of zero amplitude to large mode numbers ($n \geq 116$ at this specific y value) results in exaggerated amplitudes of the rest of the modes. Using the correct definition of f_{cut} shows a significant improvement in the skin friction coefficient for both STG formulations, as depicted in Figure 5.9. The adaptation length is significantly smaller compared to the results with the erroneous definition of f_{cut} .

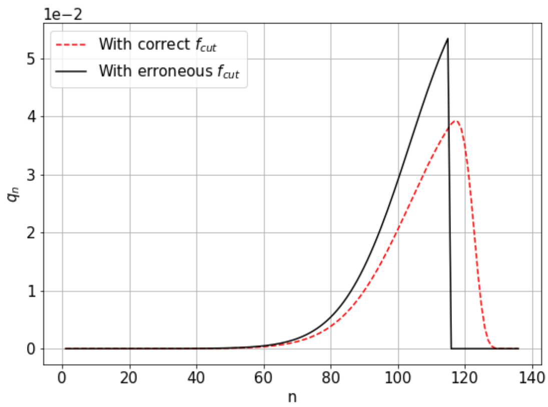

Figure 5.8: The normalized amplitude distribution for the flat plate test case at $y \approx 15\%\ \delta_0$

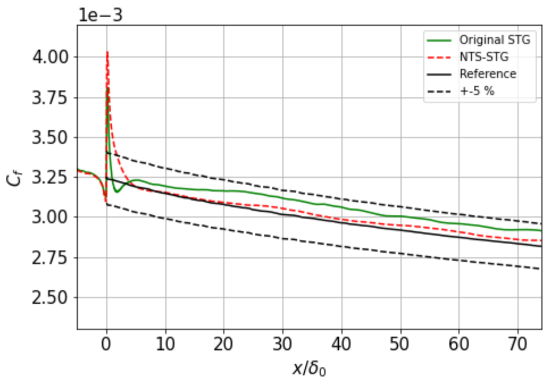

Figure 5.9: Skin friction with the correct f_{cut} for the flat plate test case. Results were obtained using the original STG and NTS-STG with the mean U_0 and the DLR source term.

In this chapter, two important aspects of the STG formulation were studied, namely, the macro-scale velocity and the cut-off frequency. It was found that using instantaneous macro-scale velocity leads to temporal decay in the quality of the synthetic turbulence. This is because the synthetic velocities do not exhibit the correct auto-correlation when using instantaneous macro-scale velocity. Furthermore, the effect of using the erroneous definition of the cut-off frequency was analyzed. It was found that the erroneous f_{cut} distorts the normalized amplitude distribution. With these two aspects, an improvement in the original STG of Adamian et al. [12] implementation was achieved. Moreover, a new variant of the original STG, known as NTS-STG, was implemented and evaluated. A comparison between the two variants showed comparable results, with the NTS-STG showing slightly better agreement with the reference in terms of C_f. As a result, all the upcoming computations will use NTS-STG, unless explicitly stated otherwise.

6

The Input of the Synthetic Turbulence Generator: A Sensitivity Analysis

In this chapter, the sensitivity of the Synthetic Turbulence Generator (NTS-STG) to two of its inputs is evaluated. The first input involves the random number set used to determine the direction and phase shifts of the various modes, and the second is the target Reynolds stresses, which can either be reconstructed from a RANS solution or taken for an existing DNS or LES results.

This chapter focuses on the direct output of the NTS-STG, more specifically, the statistics of the synthetic velocities $\left\langle u'_{s_i} u'_{s_j} \right\rangle_t$, as opposed to the resolved stresses $\left\langle u'_i u'_j \right\rangle_t$. The synthetic velocities are produced by the NT-STG, while the resolved velocities are $u'_i = \widetilde{u}_i - \langle \widetilde{u}_i \rangle_t$, such that $\left\langle u'_i u'_j \right\rangle_t$ are the resolved Reynolds stresses. The resolved velocities (and thus the resolved Reynolds stresses) are the result of injecting synthetic turbulence into the flow using a source/forcing term. Such source terms take synthetic velocities as input and result in resolved velocities as output. A schematic illustrating this distinction together with the focus of this chapter (highlighted in green) is shown in Figure 6.1. In this chapter, the default DLR source term, detailed in section 7.1, is used in all computations.

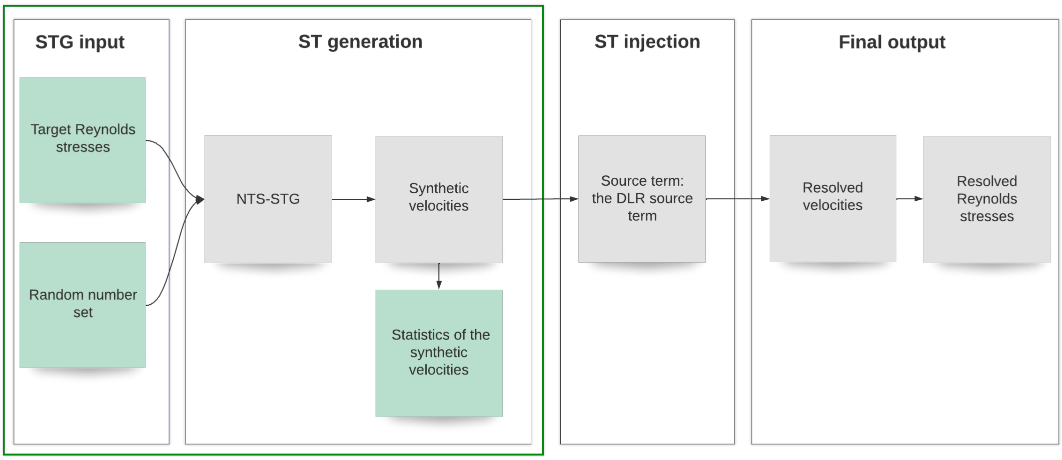

Figure 6.1: Schematic showing the area of focus in this chapter

In NTS-STG, a limited number of wave modes and a predetermined set of random numbers are used, which could lead to inaccuracies in the statistics of the synthetic velocities $\langle u'_{s_i} u'_{s_j} \rangle_t$. An increase in the number of wave modes, which directly correlates to the number of random numbers, can enhance the recovery of the properly normalized energy spectra or, in physical space, the auto-correlation functions. However, increasing the number of wave modes is computationally expensive. To ensure small errors in the statistics of the synthetic turbulence, while maintaining a relatively small number of modes, the random numbers have to be chosen properly. In this chapter, selection procedures are outlined to choose a random number set in a manner that minimizes the discrepancy between the synthetic turbulence statistics and the target Reynolds stresses.

Since one can only use a finite number of wave modes and time steps, two important aspects need to be studied. The first pertains to the convergence of the synthetic turbulence statistics to the target Reynolds stresses when averaged over an infinite time, i.e., whether $\lim_{t\to\infty} \left\langle u'_{s_i} u'_{s_j} \right\rangle_t = R_{ij}$. The second aspect relates to the time required for convergence, namely, whether $\left\langle u'_{s_i} u'_{s_j} \right\rangle_t - \lim_{t\to\infty} \left[\left\langle u'_{s_i} u'_{s_j} \right\rangle_t \right]$ is sufficiently small for an appropriate averaging time, which is typically a few domain flow-through times. The first aspect is referred to as the bias error, and the second is referred to as the time convergence error [16].

The analysis starts with deriving mathematical expressions that isolate the bias and the time convergence errors, associated with a particular realization of a random number set, relative to the target Reynolds stress tensor. The covariance tensor of the synthetic velocities is,

$$\left\langle u'_{s_l} u'_{s_m} \right\rangle_t = a_{li} a_{mj} \left\langle v'_i v'_j \right\rangle_t , \tag{6.1}$$

where the Cholesky decomposition of the Reynolds stress tensor a_{ij} provides the scaling of the random fluctuations v'_i. Therefore, to study the aforementioned realization-dependent errors, one may consider only the covariance of the fluctuation tensor $\left\langle v'_i v'_j \right\rangle_t$, with v'_i

$$v'_i = 2\sqrt{\frac{3}{2}} \sum_{n=1}^{N} \sqrt{q^n} \sigma_i^n \cos\left(\kappa^n d_l^n \hat{x}_l + \psi^n\right) \tag{6.2}$$

It is known from Kraichnan [31] that as the number of realizations (in this case, the number of wave modes) increases, the covariance of the fluctuation tensor converges to δ_{ij}. Despite being more precise, a large number of modes is not desirable due to the high computational effort associated with Equation 6.2. Therefore, it is only practical to minimize the error associated with the specific realization of a finite random set by ensuring small bias and time convergence errors.

The covariance of the fluctuation tensor $\left\langle v'_i v'_j \right\rangle_t$ is decomposed to a time-independent component α_{ij}^{np} and a time-dependent component β^{np}. Based on this decomposition, Patterson et al. [16] defined measures to a priori evaluate the errors associated with using a specific random number set, namely, the bias and time convergence errors. The decomposition is as follows:

$$\left\langle v'_i v'_j \right\rangle_t = \sum_{n=1}^{N} \sum_{p=1}^{N} \alpha_{ij}^{np} \beta^{np} \tag{6.3}$$

with α_{ij}^{np} and β^{np} given by

$$\alpha_{ij}^{np} \equiv 6\sqrt{q^n q^p} \sigma_i^n \sigma_j^p , \quad \beta^{np} \equiv \frac{1}{t} \int_0^t \cos\left(\gamma^n t' + \hat{\psi}^n(x)\right) \cos\left(\gamma^p t' + \hat{\psi}^p(x)\right) \mathrm{d}t' \tag{6.4}$$

The benefit of isolating the unsteady time-dependent error and the time-independent error is that the contribution of the former to the overall error can be eliminated by computing the limit as $t \to \infty$, which reads:

$$\lim_{t\to\infty} \beta^{np} = \frac{1}{2} \delta^{np} \tag{6.5}$$

Combining Equation 6.4 and Equation 6.5, the infinite time value of the covariance of the fluctuation tensor is then

$$\sum_n \sum_p \alpha^{np} \delta^{np} / 2 = \sum_n \alpha^{nn} / 2 \tag{6.6}$$

The error in the time-independent term α_{ij}^{np}, denoted (e_{ij}^{α}), is then computed by finding the difference between this infinite-time value of the covariance tensor and the δ_{ij}. Since the bias error ($e_{ij}^{R_b}$) is a measure of the deviation from the target Reynolds stress, e^{α}_{ij} is scaled with Cholesky decomposition components. The bias error is then computed as follows:

$$\begin{aligned} e^{\alpha}_{ij} &= \alpha^{nn}_{ij}\frac{1}{2} - \delta_{ij} \\ e^{R_b}_{ij} &= a_{il}a_{jm}e^{\alpha}_{lm} \end{aligned} \tag{6.7}$$

Similarly, the error in the time-dependent term β^{np} is simply the difference between its time-averaged value and the infinite-time value given in Equation 6.5, therefore, $e^{np}_t = \langle\beta^{np}\rangle_t - \frac{1}{2}\delta^{np}$. More importantly, the time convergence error is the difference between the running averaged second-order moments and the corresponding target Reynolds stress components

$$e^{R_t}_{ij} = a_{il}a_{jm}\left\langle u'_{s_i}u'_{s_j}\right\rangle_t - \left\langle u'_{s_i}u'_{s_j}\right\rangle_{t\to\infty} \tag{6.8}$$

With an estimation of bias and time convergence errors at hand, Patterson et al. [16] developed different procedures for selecting an appropriate random number set, one of which is referred to as sequential choosing, which is partially adopted in this work. The sequential choosing procedure is to choose the two random sets θ^n and ϕ^n that produce σ^n in a way that minimizes the bias error. The sequential choosing method then determines a third random set η^n, which along with θ^n, produces d^n_j. The first component d^n_1 determines γ^n, which should not be too small or too close to other γ^p in absolute value to avoid slow time convergence.

It was found that minimizing both the bias and time convergence errors simultaneously, as opposed to focusing on just one aspect, results in a larger error in one of the aspects [16]. So, it can be seen as a compromise between the two errors. In this work, the focus is to minimize the bias error. The bias error estimation in Equation 6.7 was used to evaluate the bias error for 10000 different random number sets and select the one with the least bias error. This ensures that the selected random number set has a sufficiently small bias error, resulting in a better representation of the target Reynolds stresses. This selection of a specific realization of random numbers based on the bias error estimation will be referred to as the selection procedures.

6.1. Results

To illustrate the influence of the realization-dependent bias error, two different realizations of random numbers were drawn and used to generate synthetic velocities. The statistics of these two sets of synthetic velocities were computed, which yields the synthetic Reynolds stresses. These are simply the time averaged $<u'_{s_i}u'_{s_j}>$. Note that this is the direct output of the NTS-STG, meaning that the synthetic velocities are not yet injected in the flow. When the synthetic velocities are injected into the flow by means of a source term, the resolved velocities and thus the resolved Reynolds stresses are obtained. Eventually, we are interested in the resolved Reynolds stresses and how they are affected by errors in the statistics of the synthetic turbulence, which are discussed in subsection 6.1.1 and subsection 6.1.2.

Figure 6.2 shows the time-averaged $<u'_s u'_s>$ and $<u'_s v'_s>$, and the respective target Reynolds stresses for the flat plate case. Note that the notation $< . >$ is now adopted instead of $< . >_t$ for the sake of simplicity. It can be seen that the statistics of the synthetic velocities exhibit substantial variations solely due to the specific realization of random numbers, representing an undesirable source of error. This error is the bias error, which remains present even when the averaging time approaches ∞. In the next subsections, the influence of this error on the resolved Reynolds stresses and the mean surface quantities is discussed. Furthermore, the selection procedures are implemented and used to obtain synthetic velocities whose statistics exhibit small bias errors.

6.1.1. Influence of the random number set: the flat plate test case

In this subsection, the selection procedures are applied in the flat plate case. Figure 6.3 shows the statistics of the synthetic turbulence (in green) as well as the second-order statistics of the resolved velocities (in red) using two different realizations. One of these realizations was obtained using the aforementioned selection procedures (indicated by the dashed lines), whereas the other was drawn randomly (indicated by the solid lines). First, looking at the statistics of the synthetic velocities, the selection procedures lead to smaller deviations between the statistics of the synthetic turbulence and the

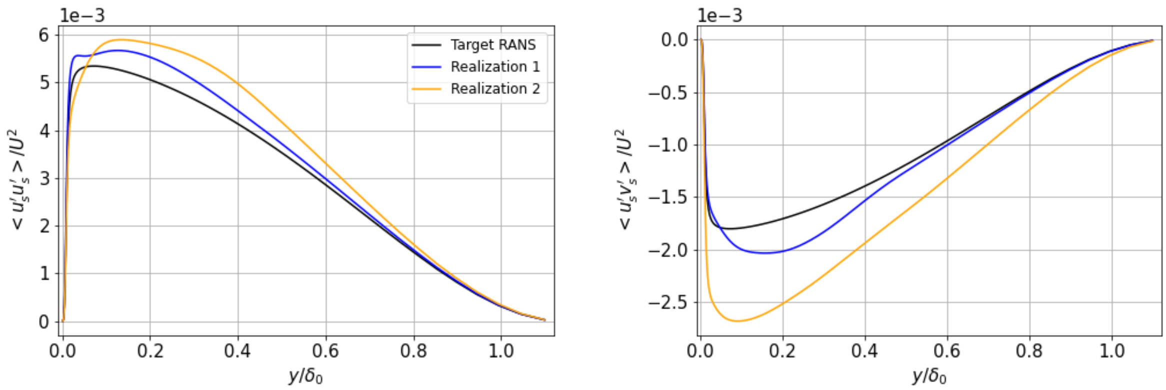

(a) $<u_s' u_s'>$ **(b)** $<u_s' v_s'>$

Figure 6.2: Statistics of the synthetic turbulence using two different random number set realizations for the flat plate test case

target stresses. This is especially evident in the turbulent shear stress in Figure 6.3b, where the synthetic turbulence computed with the selected random number set matches the target very well, whereas the random realization produces synthetic velocities that severely underestimate their target.
Regarding the resolved stresses (in red), they demonstrate a consistent underestimation compared to the target Reynolds stresses, even when the statistics of the synthetic velocities are accurate. For instance, the wall-normal Reynolds stress exhibits a good agreement with the target stress, however, the resolved stress still falls short as shown in Figure 6.3c. This behavior is also observed in other Reynolds stresses, especially in $<u'v'>$ and $<w'w'>$ as depicted in Figure 6.3b and in Figure 6.3d, respectively. This deficit in resolved stresses is discussed in the upcoming chapters, as the focus of this chapter is to study the input and the direct output of the NTS-STG itself, and not the resulting output of the forcing term. The mean surface quantities, the skin friction coefficient and the pressure fluctuations, using the two random number sets are shown in Figure 6.4. The skin friction coefficient results are comparable, with both computations showing a large peak at the RAN-LES interface. When using the selection procedures, a small underestimation in C_f is observed downstream of the interface, then it rapidly approaches the reference value. Both realizations show a large spike in pressure fluctuations, an indication of significant spurious noise at the interface. So, the mean surface quantities produced using both random number sets are very comparable. Note, the peak observed in both C_f and the pressure fluctuations is addressed in chapter 8. The flat plate test case has limitations in two aspects:

- The target Reynolds stresses are not very accurate since they are reconstructed from a RANS solution.
- There is a lack of DNS/LES or experimental data in close proximity to the interface.

Even though the target Reynolds stresses reconstructed from a RANS are reasonably accurate, particularly in the outer part of the boundary layer, they do not capture the detailed statistics of turbulent fluctuations near the wall. This is evident in the streamwise Reynolds stress $<u'u'>$, where the near-wall peak, present in both DNS and experimental data, is not captured by reconstructed $<u'u'>$. While it is not strictly necessary to have an accurate estimate of the Reynolds stress in the vicinity of the wall, as this region is treated by RANS, this still introduces a source of error that needs to be considered. With the rounded step case, the target Reynolds stresses are available from DNS results at the same Reynolds numbers.

The second limitation is the absence of high-fidelity data, which prohibits the assessment of turbulence development in close proximity to the RANS-LES interface. The rounded step case, on the other hand, provides a better opportunity for such assessment thanks to its well-resolved LES solution of [25]. As a result, the rounded step test case is considered more attractive to study turbulence development and is discussed in the next subsection.

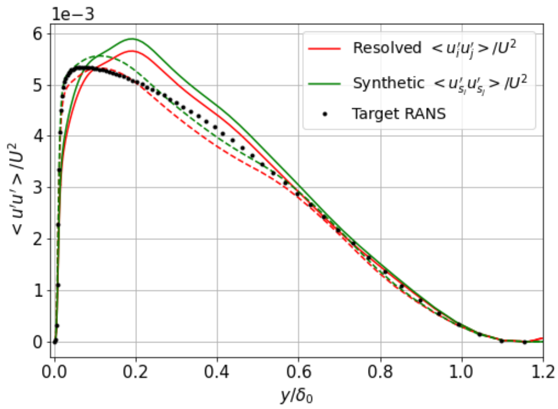

(a) Synthetic, resolved and target $<u'u'>$

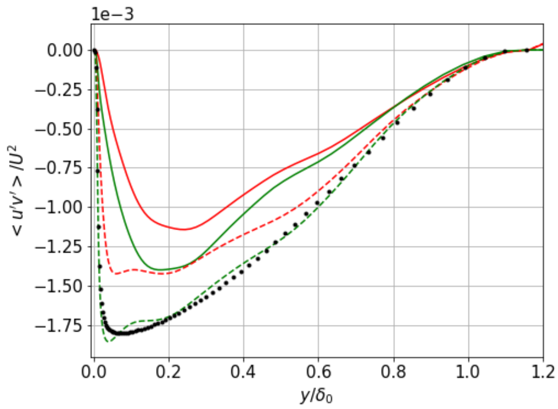

(b) Synthetic, resolved and target $<u'v'>$

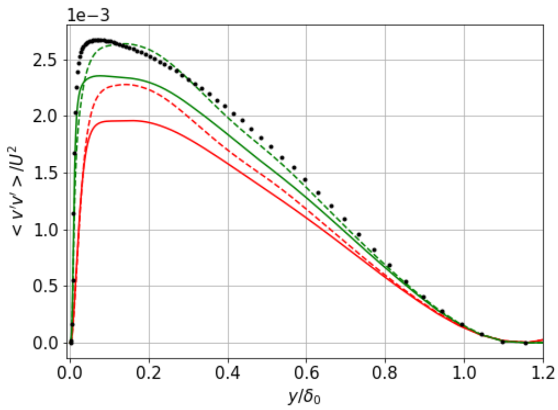

(c) Synthetic, resolved and target $<v'v'>$

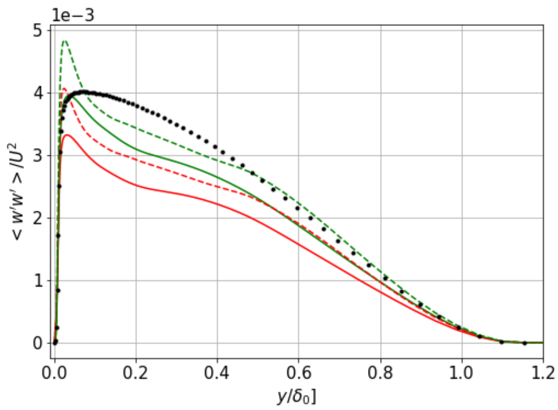

(d) Synthetic, resolved and target $<w'w'>$

Figure 6.3: Statistics of the synthetic turbulence and the resolved velocities for the flat plate. Solid lines: random realization, dashed lines: with the selection procedures

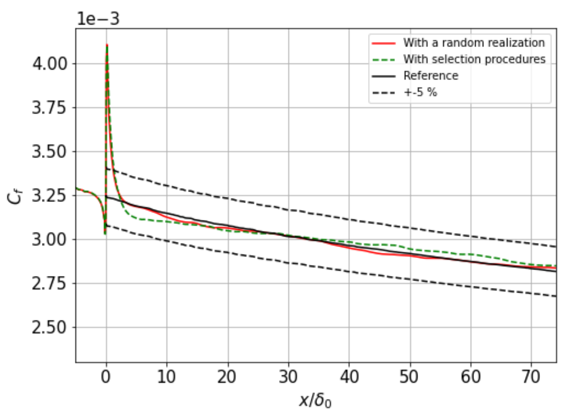

(a) C_f

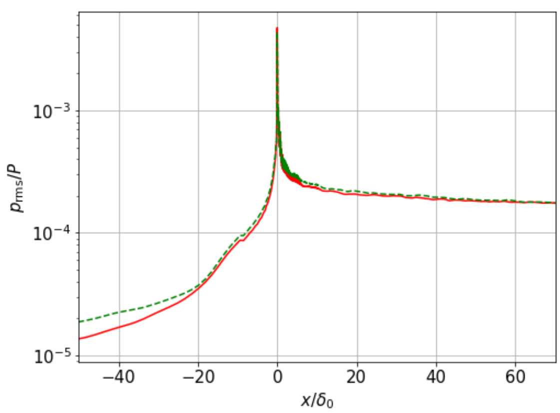

(b) Pressure fluctuations

Figure 6.4: Skin friction coefficient and pressure fluctuations for the flat plate case using the DLR source term

6.1.2. Influence of the random number set and target Reynolds stresses: the rounded step test case

In this subsection, the influence of the random number set is assessed for the rounded step case. Furthermore, the availability of DNS target Reynolds stress allows assessing the influence of the target

Reynolds stresses themselves, which are either taken from existing DNS results or reconstructed from a RANS solution. Ideally, one would try to provide synthetic turbulence generators with target stresses that are obtained using a high-fidelity method, such as LES or DNS. However, this is not always possible, simply due to the lack of such high-fidelity data. Alternatively, target Reynolds stresses are typically reconstructed using the underlying RANS model. This, of course, introduces a source of error that is assessed in this subsection.

Similar to the flat plate case, RANS target Reynolds stresses were used to generate synthetic turbulence with NTS-STG using both a random realization and a realization with the selection procedures. The statistics of the synthetic turbulence along with the RANS target for both realizations are shown in Figure 6.5. The random realization produces synthetic turbulence that matches fairly well the target stresses, except for the turbulent shear stress. As shown in Figure 6.5b, the statistics of the synthetic velocities that were computed using the random realization has a large peak (solid green line), whereas that computed with the selected set match perfectly the target (dashed green line). On the other hand, the statistics of the synthetic velocities that were computed using the selected set match perfectly all target stresses except for $<w'w'>$, with a slight underestimation, as shown in Figure 6.5d. So, using the selected set is advantageous, as it results in a smaller bias error. Regarding the resolved stresses, a consistent deficit in resolved stress is observed in both computations, as it is the case for the flat plate, which is discussed in chapter 8. The mean surface quantities for the rounded step using RANS target

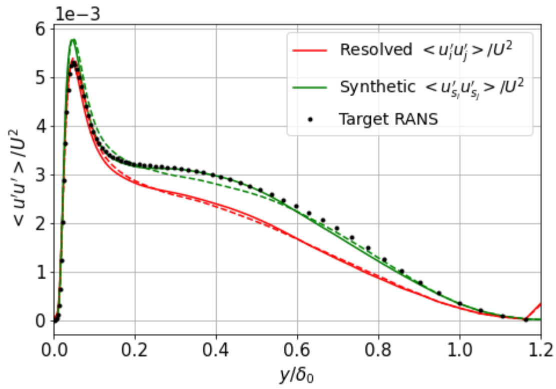

(a) Synthetic, resolved and target $<u'u'>$

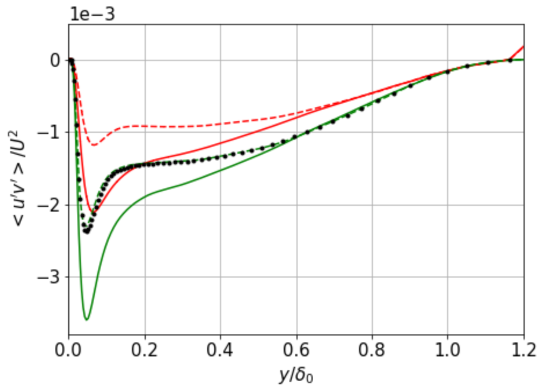

(b) Synthetic, resolved and target $<u'v'>$

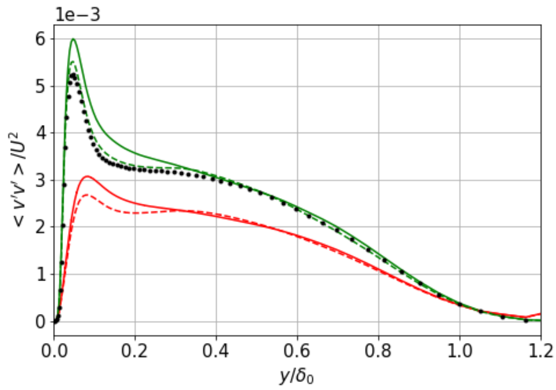

(c) Synthetic, resolved and target $<v'v'>$

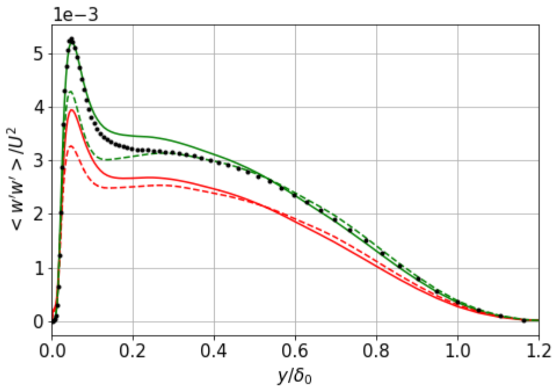

(d) Synthetic, resolved and target $<w'w'>$

Figure 6.5: Statistics of the synthetic turbulence and the resolved velocities with RANS target Reynolds stress for the rounded step. Solid lines: random realization, dashed lines: with the selection procedures

Reynolds stresses combined with either a random or selected realization of random numbers are shown in Figure 6.6. Both computations show comparable results. The specific realization of the random number set appears to have less impact on the mean surface quantities compared to the Reynolds stresses. Similarly, the DNS target Reynolds stresses were used to compute the synthetic velocity field

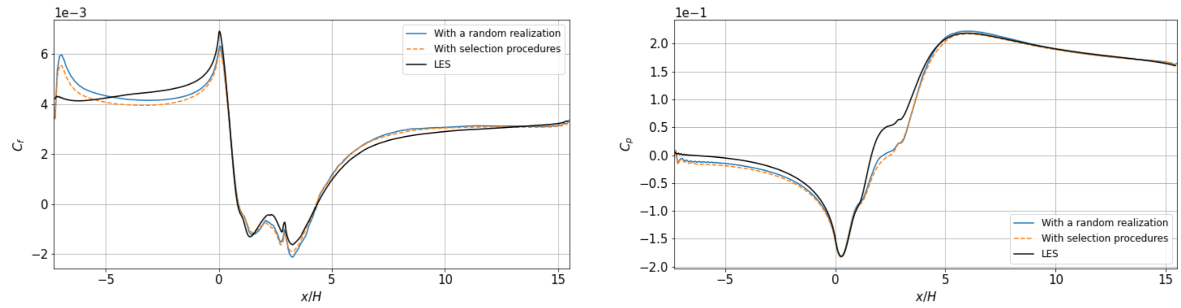

(a) C_f **(b)** C_p

Figure 6.6: Skin friction and pressure coefficient using RANS target Reynolds stresses

along with either a random realization or a properly selected random set using the selection procedures. Similar to the computation with RANS target stress, when the selected set is used, the statistics of the synthetic velocities are in close agreement with the target stress. This is particularly clear in the turbulent shear stress, shown in Figure 6.7b. Interestingly, even when using the selected random number set, the near-wall physical peak in <$u'u'$> could not be captured as shown in Figure 6.7a. Regarding the wall-normal and spanwise stresses, the selected random number set shows good agreement with the target, except for a small deviation in the latter, as shown in Figure 6.7d. Regarding the mean surface

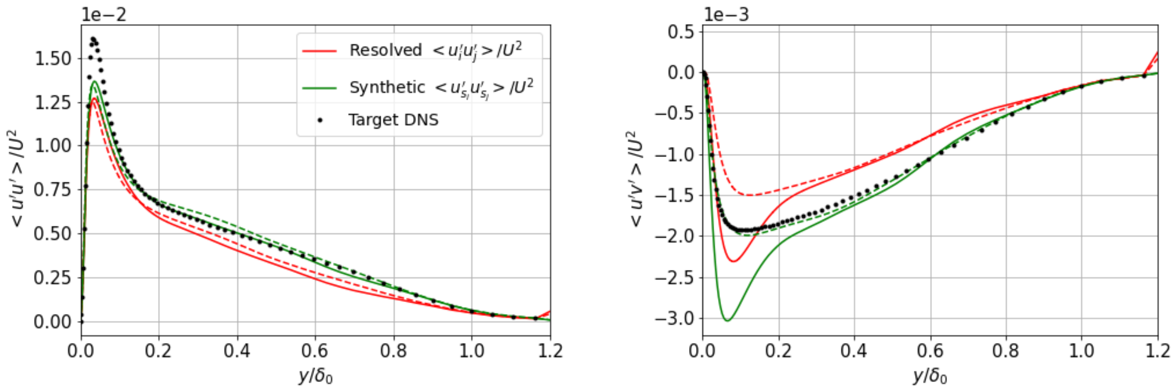

(a) Synthetic, resolved and target <$u'u'$> **(b)** Synthetic, resolved and target <$u'v'$>

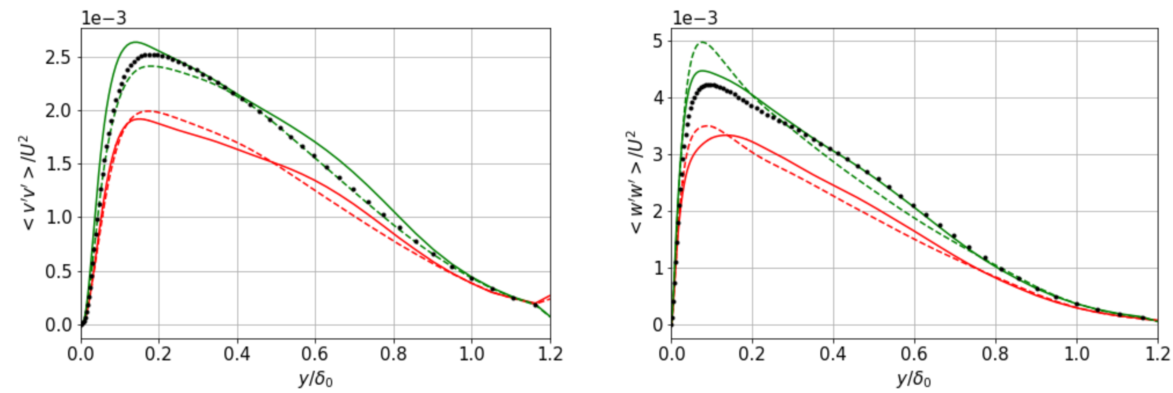

(c) Synthetic, resolved and target <$v'v'$> **(d)** Synthetic, resolved and target <$w'w'$>

Figure 6.7: Statistics of the synthetic turbulence and the resolved velocities with DNS target Reynolds stress for the rounded step. Solid lines: random realization, dashed lines: with the selection procedures

quantities, the results are shown in Figure 6.8. As shown in Figure 6.8a, there is no significant deviation between the two cases in terms of C_f in the upstream region. However, in the reattachment region, the computation with the selection procedures shows closer agreement with the LES reference data. Furthermore, the pressure coefficient shows a better agreement with the reference data in the upstream region when the selection procedures are used.

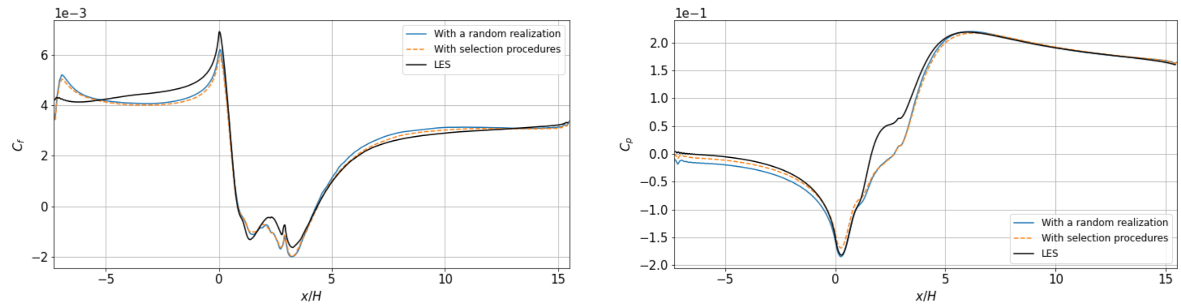

(a) C_f **(b)** C_p

Figure 6.8: Skin friction and pressure coefficient using DNS target Reynolds stresses

In order to accurately evaluate the impact of the target Reynolds stresses and the choice of random number set, it is necessary to examine the development of the resolved stresses downstream of the RANS-LES interface. The results of varying these two factors for the upstream region of the rounded step case are presented in Figure 6.9. It is observed that neither the source of the target Reynolds stresses nor the realization of the random set has an effect on the mean velocity profile, as shown in Figure 6.9a and Figure 6.9b. Regarding the Reynolds stresses, the impact of the target Reynolds stresses is evident, particularly in the resolved $<u'v'>$ and $<w'w'>$, shown in Figure 6.9d and Figure 6.9h, respectively. These stresses exhibit near-wall peaks that persist even far downstream of the interface.

Regarding the influence of the random number set realization, using the selection procedures results in a smaller near-wall peak in the resolved stress compared to the case with a random realization even with RANS target Reynolds stresses. This is particularly clear in Figure 6.9d and Figure 6.9h, where the resolved $<u'v'>$ and $<w'w'>$, respectively, have a smaller peak near the wall. It is evident that the use of the DNS target Reynolds stress along with the selection procedures results in the most agreement with the LES reference data.

Figure 6.10 shows the result of the same computations in the vicinity of the rounded step. All computations show comparable results, with no clear outperforming method. Given that the location downstream of the rounded step is far from the location where the synthetic turbulence is forced and because of the presence of natural instabilities caused by separation, the correlation between the injected synthetic turbulence and the resolved stress in this region is not expected to be strong. The results are presented for the sake of completeness.

In this chapter, the impact of two important input parameters for the NTS-STG was assessed. The first is the random number set used to define the direction and the phase shifts of different modes, while the second is the target Reynolds stresses, which can be either reconstructed from the underlying RANS model or obtained from DNS results. It was found that using the selection procedures prevents large bias errors that will otherwise be present when a random realization is used. The impact of these large bias errors is not limited to the forcing region, but has long-lasting effects that remain present downstream of the forcing region.

Furthermore, the influence of the target Reynolds stresses was evaluated in the rounded step case. It was found that even when inaccurate RANS Reynolds stresses were used, the flow was still able to adapt to the correct Reynolds stress levels. However, this adaptation length can be significantly large compared to using DNS or, in general, more accurate target Reynolds stresses. It was also found that using selection procedures along with inaccurate RANS stresses could slightly decrease the distance needed for the stress levels to adapt to the correct values. On the other hand, the influence of these two aspects on the velocity profiles and the mean surface quantities is not as severe as it is on the Reynolds stresses. Nevertheless, for the rounded step case, C_f and C_p showed a slightly better agreement with the reference when the DNS target stresses along with the selection procedures were used.

To avoid accumulating sources of error, all the upcoming computations will use the selected random

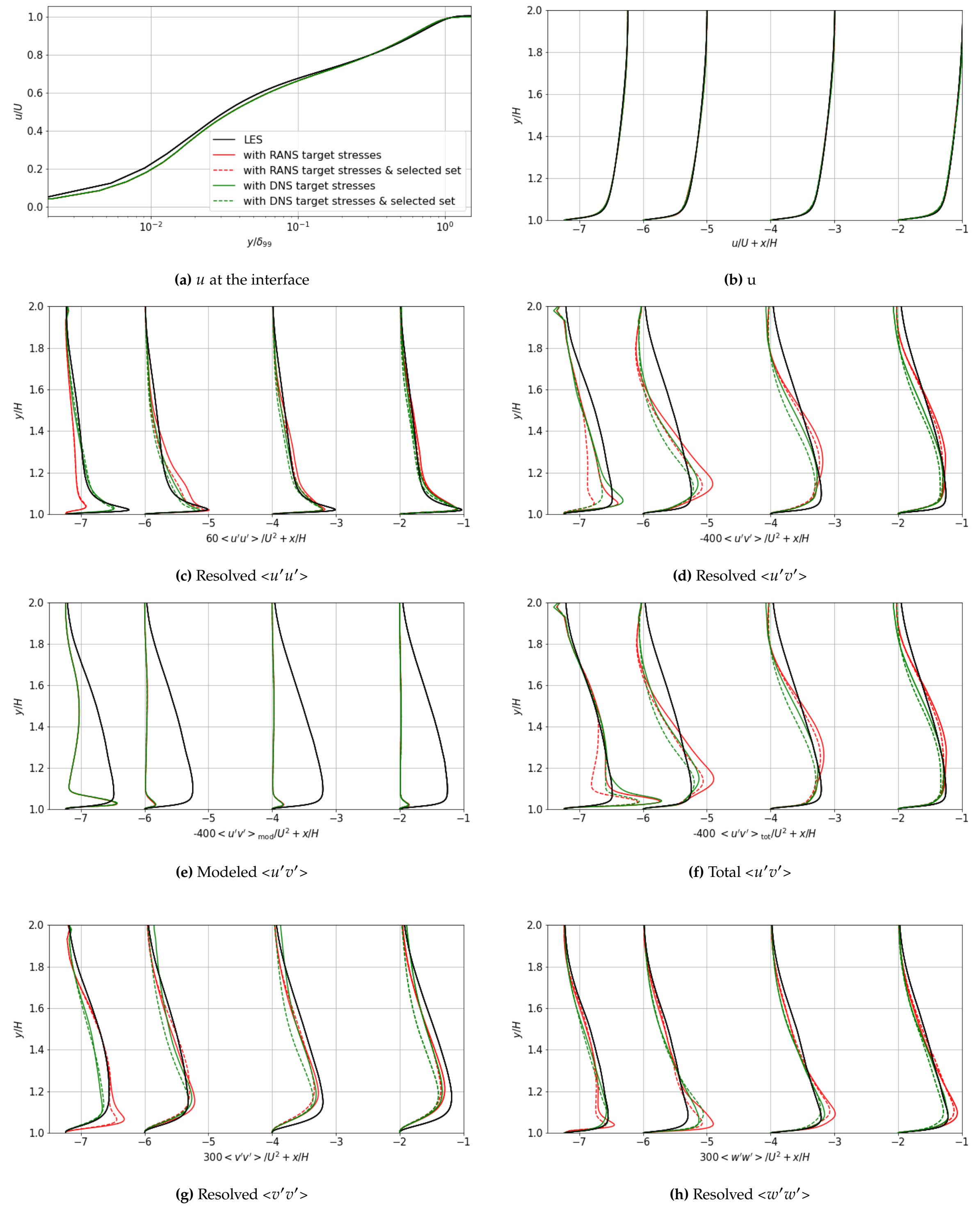

(a) u at the interface

(b) u

(c) Resolved $<u'u'>$

(d) Resolved $<u'v'>$

(e) Modeled $<u'v'>$

(f) Total $<u'v'>$

(g) Resolved $<v'v'>$

(h) Resolved $<w'w'>$

Figure 6.9: Comparison between using DNS and RANS as target Reynolds stresses with (dashed lines) and without (solid lines) the selection procedures upstream the curved section

number sets that were used in this chapter, unless explicitly stated otherwise. Furthermore, DNS target Reynolds stresses will be used for the rounded step test case. With an ensured high-quality synthetic turbulence (see chapter 5) and an accurate input for the NTS-STG as discussed in this chapter, the forcing of the synthetic turbulence can be studied, which is discussed in the next chapter.

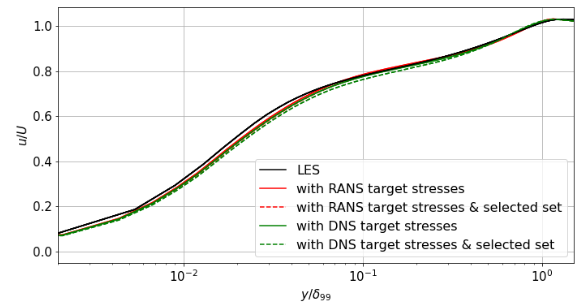

(a) u at $x/H = 0$

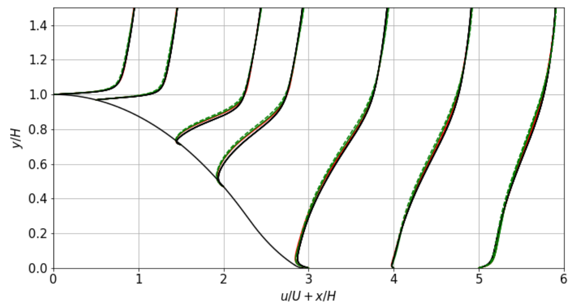

(b) u

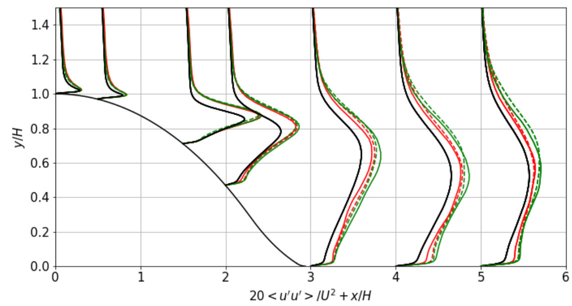

(c) Resolved $<u'u'>$

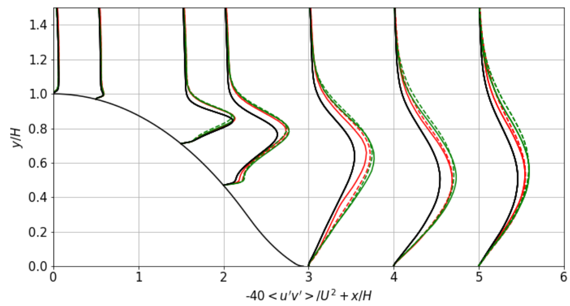

(d) Resolved $<u'v'>$

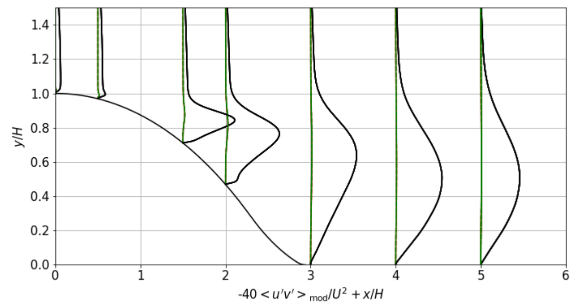

(e) Modeled $<u'v'>$

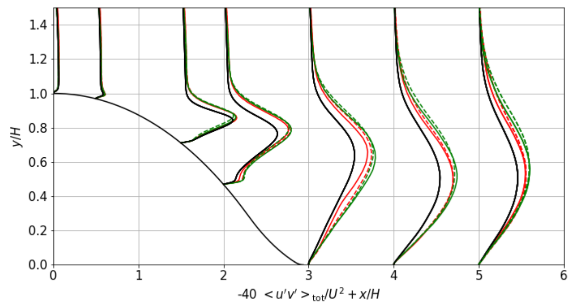

(f) Total $<u'v'>$

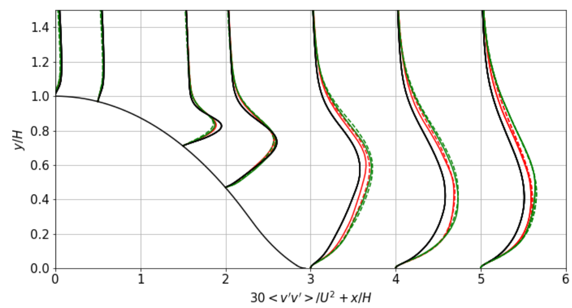

(g) Resolved $<v'v'>$

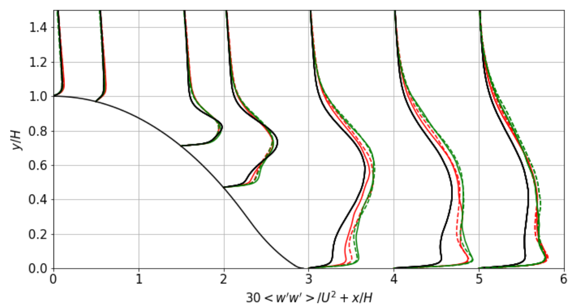

(h) Resolved $<w'w'>$

Figure 6.10: Comparison between using DNS and RANS as target Reynolds stresses with (dashed lines) and without (solid lines) the selection procedures at the curved step

7

Synthetic Turbulence Forcing: Assessment and Sensitivity

In this chapter, different forcing methods are evaluated. The aim is to assess the sensitivity of the turbulence development to different factors, such as the source term, the underlying RANS model, and the size of the forcing region. The source terms evaluated are the DLR source term of Probst [14] and the VSTG source term of Shur et al. [15]. The analysis highlights the advantages and limitations of each method and provides insight into the factors that influence the development of turbulence downstream of the forcing region.

The synthetic turbulence is injected into the flow as a source term in the momentum equations. The filtered momentum equation of LES for an incompressible flow with a forcing term f_i is as follows:

$$\frac{\partial \widetilde{u_i}}{\partial t} + \widetilde{u_j}\frac{\partial \widetilde{u_i}}{\partial x_j} = -\frac{1}{\rho}\frac{\partial \widetilde{p}}{\partial x_i} + v\frac{\partial^2 \widetilde{u_i}}{\partial x_j \partial x_j} - \frac{\partial \tau_{ij}}{\partial x_j} + f_i \tag{7.1}$$

where the $\widetilde{\cdot}$ denotes the LES filtering operator and $\tau_{ij} = \widetilde{u_i u_j} - \widetilde{u_i}\widetilde{u_j}$ is the sub-grid scale tensor.

Source terms can be applied in two manners, namely, interface or volumetric. In interface forcing, the synthetic turbulence is injected in a single plane perpendicular to the flow direction. In volumetric forcing, the injection takes place over a volume that extends in the streamwise direction, commonly referred to as the forcing region. Volumetric forcing has the ability to gradually increase the intensity of the forcing in the downstream direction by using blending functions. As a result, volumetric forcing could reduce spurious noise associated with the sudden onset of turbulence, typical of interface forcing, without using additional tools (such as internal damping layer (IDL)) [15]. On the other hand, having a large forcing region is undesirable, in particular in the case of rapidly varying flows, because the target velocity profiles and Reynolds stresses may become unrepresentative of the flow. This is not a concern in interface forcing, since the synthetic turbulence injection is applied in a plane, so the target quantities are typically sampled from directly upstream of the interface.

7.1. The DLR Source Term

The first source term is based on computing the partial time derivative of the fluctuating velocity component (u_i') [14]. It is donated the DLR source term, as it was proposed by DLR. In the formulation of the DLR source term, an implicit 2nd-order time discretization scheme is used, which reads as

$$F_i = \frac{\partial \left(\rho u_i'\right)}{\partial t} \approx \frac{3\left(\rho u_i'\right)^{n+1} - 4\left(\rho u_i'\right)^{n} + \left(\rho u_i'\right)^{n-1}}{2\Delta t} \tag{7.2}$$

The fluctuating velocity $u_i'^{n+1}$ is taken from the synthetic turbulence generator, so $u_i'^{n+1} = u_{s_i}'^{n+1}$. Thus, this source term seeks to force the flow to generate fluctuations equal to those produced by the synthetic turbulence generator at time step $n+1$. The fluctuating velocities at the previous times are computed as the difference between the instantaneous and the running time-averaged velocities as follows:

$$u_i'^{n} = u_i^{n} - \langle u_i \rangle\,,\ u_i'^{n-1} = u_i^{n-1} - \langle u_i \rangle \tag{7.3}$$

This treatment prevents the decoupling of the computed flow from the synthetic turbulence field, however, it requires computing the running time averages.

The DLR source term can be applied in either a single plane (interface forcing) or in a volume (volumetric forcing). When applied in a volume, a blending function can be used to gradually introduce the synthetic velocities into the flow. Typically, such blending functions start with a value of zero at the beginning of the forcing region, increase to a value of 1 near the center of the forcing region, and then decrease back to zero at the end of the forcing region. In this work, the forcing region, when using the volumetric DLR forcing, is always half of the boundary layer thickness ($0.5\delta_0$), which was shown to produce good agreement with the reference [22].

7.2. The VSTG Source Term

The other forcing term analyzed in this work is the VSTG. It is a volumetric source term proposed by Shur et al. [15] with the aim of reducing the spurious noise associated with the sudden onset of turbulence when interface force is used. This forcing approach consists of introducing a source term to the momentum equations and a sink term to the turbulent kinetic energy transport equations. The VSTG is based on a purely empirical formulation of the source term in the momentum equation, which reads:

$$F_i = C_{BF}\rho U_0 u'_{s_i}(x,y,z)\alpha_{\mathrm{VSTG}}(x) \tag{7.4}$$

where $C_{BF} = 1.1$ is an empirical constant, $\alpha_{\mathrm{VSTG}}(x)$ is a blending function determining the spatial distribution of the source term intensity. In addition to introducing a source term to the momentum equations, a sink term is added to the turbulent kinetic energy transport equations. The VSTG was originally formulated for IDDES with $k-\omega$ SST as the underlying RANS model. Therefore, the sink term is defined as follows:

$$F_{k-\omega} = -\rho U_0 \alpha_{\mathrm{VSTG}}(x)\omega \max\left\{\left(\nu_t^{\mathrm{IDDES}} - \nu_t^{\mathrm{Smag}}\right), 0\right\} \tag{7.5}$$

where ν_t^{IDDES} and ν_t^{Smag} are the eddy viscosity computed using IDDES and Smagorinsky model, respectively. ω is the specific dissipation rate. This sink term rapidly decreases the modeled turbulence kinetic energy k , and hence, ν_t^{IDDES}, until ν_t^{IDDES} is equal to ν_t^{Smag}. This ensures a rapid transition from the RANS SST eddy viscosity to the SGS viscosity levels within the forcing region.

Since the Spalart-Allmaras (SA) model was used as the main underlying RANS model in most of the computations in this work, an equivalent sink term was used. The sink term associated with the SA model reads as follows:

$$F_{SA} = -\rho U_0 \alpha_{\mathrm{VSTG}}(x) \max\left\{\left(\nu_t^{\mathrm{IDDES}} - \nu_t^{\mathrm{Smag}}\right), 0\right\} \tag{7.6}$$

This sink term serves the same purpose as the one proposed by Shur et al. [15] and is assessed in subsection 7.3.2.

7.3. Results

In this section, the results of different forcing approaches are discussed. The sensitivity of the turbulence development to different factors is performed in the following order. First, the effect of the underlying RANS model is assessed in subsection 7.3.1. Next, the volumetric DLR and the VSTG source terms are compared, where the influence of the additional sink term (Equation 7.6) is evaluated in subsection 7.3.2. Lastly, the effect of the forcing region length is evaluated using the VSTG as the source term in subsection 7.3.3.

For the flat plate case, results are always presented at two locations, the interface or the middle of the forcing region (when volumetric forcing is used), and at a distance of 3 boundary layers thickness ($3\delta_0$) downstream of the interface. This close distance to the RANS-LES interface was chosen, as one focus of this work is to improve the quality of the synthetic turbulence, which can only be done by closely monitoring its development. Due to the lack of DNS reference data at this location, the target RANS Reynolds stresses are used as the reference data. These RANS reconstructed stresses are considered to be reliable throughout the boundary layer, excluding the near-wall region, which is modeled by RANS regardless.

7.3.1. Interface forcing with the DLR source term

The DLR source term was used in an interface setup, with two different underlying RANS models, SA and k-ω SST (SST for short). The two different RANS models were used to assess the source term sensitivity to different underlying RANS models and hence different turbulent viscosity distributions in the boundary layer. The results of the flat plate case at the interface are shown in Figure 7.1. The vertical dashed line indicates the RAN-LES interface location in the boundary layer. It is observed that the velocity profile and the resolved stress profiles are identical, regardless of the underlying RANS model. However, the modeled turbulent shear stress varies considerably as a result of the different eddy viscosity produced by each model, as shown in Figure 7.1h and Figure 7.1d. SA-IDDES shows large eddy viscosity compared to that computed by SST-IDDES throughout the whole boundary layer. Consequently, the total shear stress is overestimated with SA-IDDES, as shown in Figure 7.1e.

The results at a distance of 3 boundary layers thickness ($3\delta_0$) downstream of the interface are shown in Figure 7.2. It is evident that the development of the resolved stresses is affected by the different underlying RANS models. When using SA as the underlying RANS model, larger resolved stresses are consistently observed. Furthermore, using the SA model shows smaller eddy viscosity, especially in the outer boundary layer, as depicted in Figure 7.2h. This indicates that the SA model, unlike the SST model, quickly decreases its eddy viscosity relative to the upstream RANS, rapidly approaching the SGS viscosity levels expected in the WMLES branch of IDDES. This can be clearly seen in Figure 7.3, which shows the ratio between the eddy viscosity and the kinematic viscosity for each computation. Nonetheless, the velocity profiles and the Reynolds stresses produced using the two underlying RANS models are highly comparable.

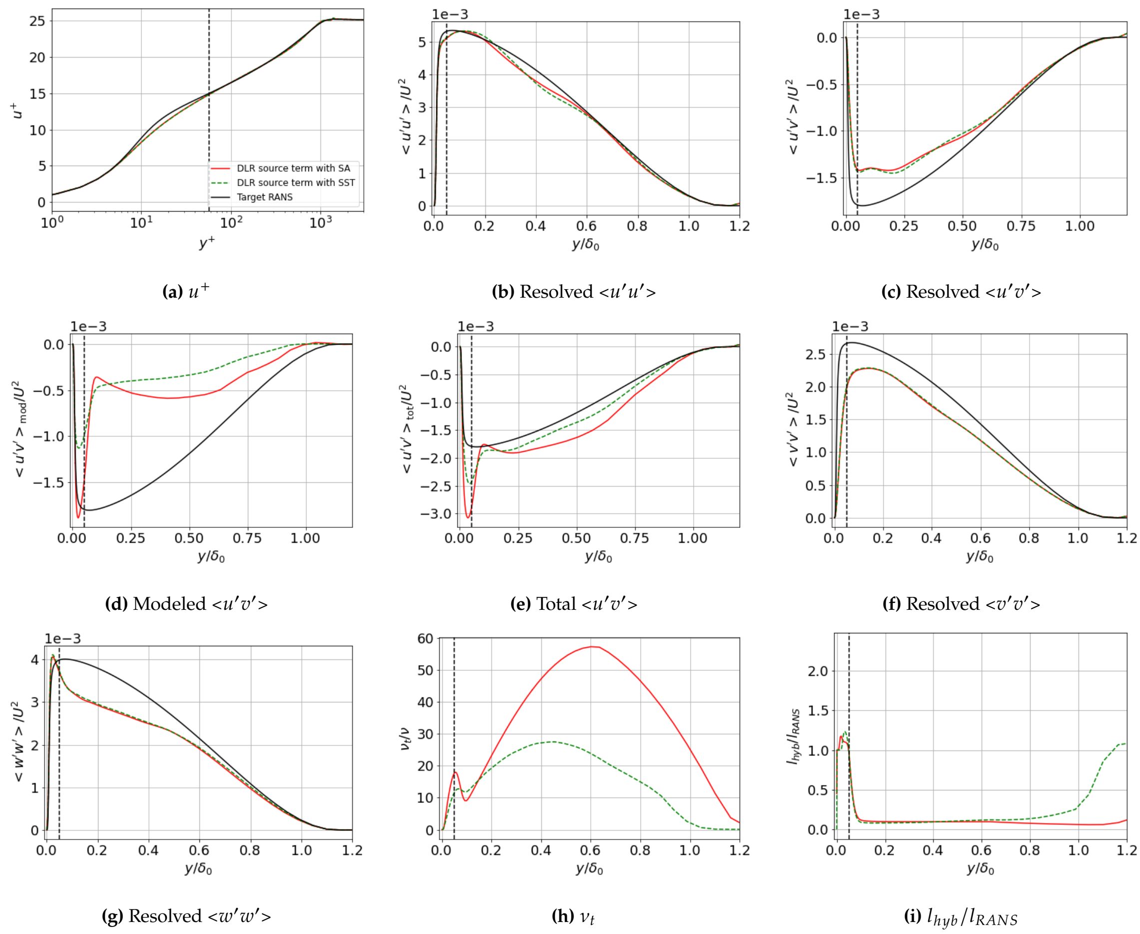

(a) u^+ (b) Resolved $<u'u'>$ (c) Resolved $<u'v'>$

(d) Modeled $<u'v'>$ (e) Total $<u'v'>$ (f) Resolved $<v'v'>$

(g) Resolved $<w'w'>$ (h) ν_t (i) l_{hyb}/l_{RANS}

Figure 7.1: Results of interface forcing using the DLR source term for the flat plate case at the interface ($x = 0$)

The skin friction coefficient and pressure fluctuations are presented in Figure 7.4. The results in Figure 7.4a indicate that the SA-IDDES provides a closer agreement with the reference skin friction

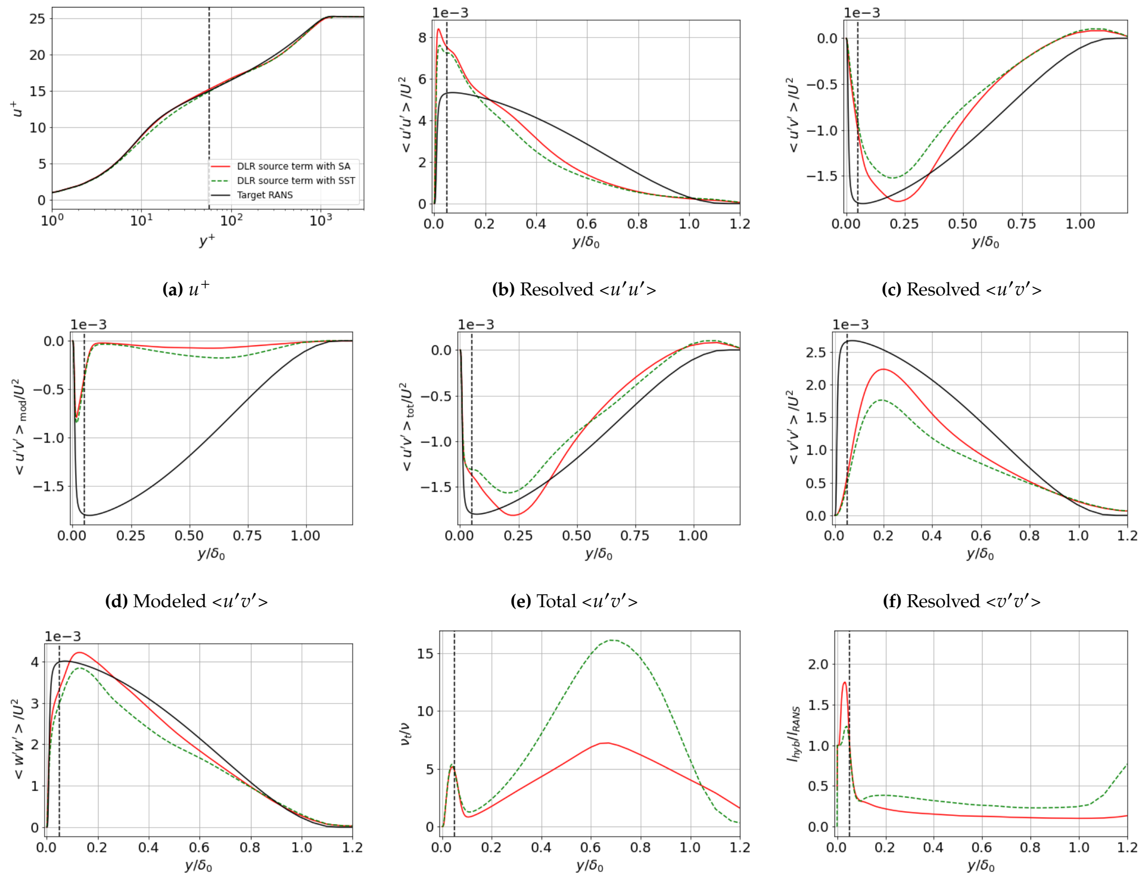

(a) u^+ **(b)** Resolved $<u'u'>$ **(c)** Resolved $<u'v'>$

(d) Modeled $<u'v'>$ **(e)** Total $<u'v'>$ **(f)** Resolved $<v'v'>$

(g) Resolved $<w'w'>$ **(h)** ν_t **(i)** l_{hyb}/l_{RANS}

Figure 7.2: Results of interface forcing using the DLR source term for the flat plate case at $x = 3\delta_0$

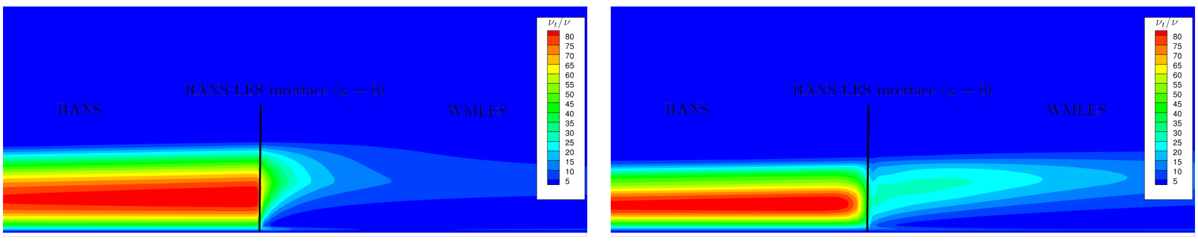

(a) SA-IDDES **(b)** SST-IDDES

Figure 7.3: ν_t/ν for the flat plate case, using SA and SST as the underlying RANS models. The synthetic turbulence was injected using the DLR source term.

coefficient. Additionally, the skin friction produced by the SST-IDDES appears to have the wrong slope, where the skin friction remains almost constant. With regard to pressure fluctuations, both the SA-IDDES and the SST-IDDES exhibit large pressure disturbances, which is discussed and treated in chapter 8.

The strange slope of C_f, observed with SST-IDDES in Figure 7.4a, can be partly attributed to the specific random number set. In order to illustrate this, another computation using another random number set was carried out. This random number set is the randomly-drawn set that was used in subsection 6.1.1. The outcome of this computation along with the result in Figure 7.4 are shown in Figure 7.5, with the former illustrated in blue. It can be observed that the skin friction coefficient resulting from SST-IDDES with the random realization matches the reference slightly better, especially far downstream ($\delta_0 > 40$). However, it still deviates from the result of SA-IDDES. The reason for this deviation is due to the different underlying RANS models, and thus different eddy viscosity distribution especially in the vicinity of the interface, as shown in Figure 7.3. Such deviations in C_f are to be expected, since even the pure SA-RANS and SST-RANS show such differences, which can be seen in (Figure 7.5a just upstream of the interface (x< 0).

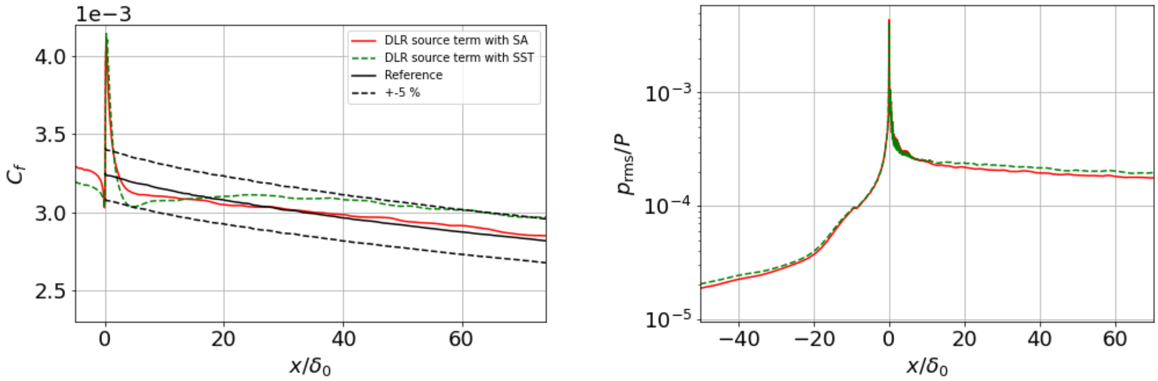

(a) C_f **(b)** Pressure fluctuations

Figure 7.4: Skin friction coefficient and pressure fluctuations for the flat plate case using interface forcing of the DLR source term

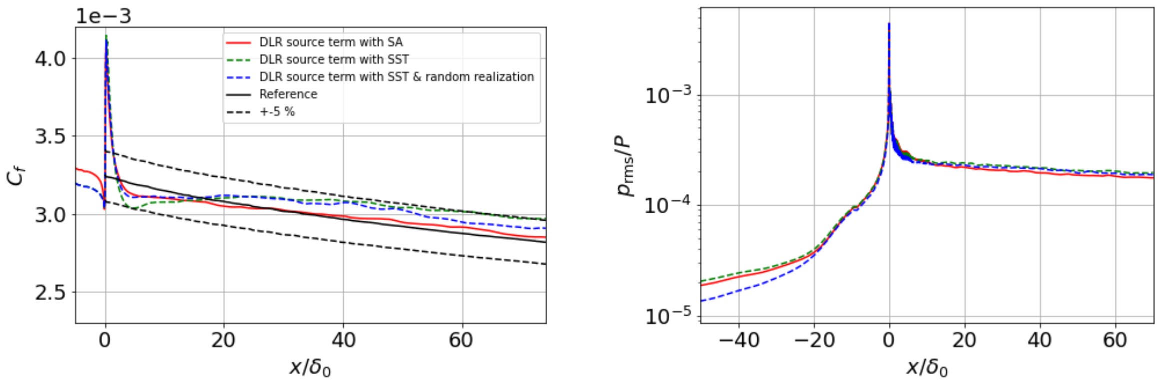

(a) C_f **(b)** Pressure fluctuations

Figure 7.5: Skin friction coefficient and pressure fluctuations for the flat plate case using interface forcing of the DLR source term and a different random number set in SST-IDDES computation.

7.3.2. Volumetric forcing: the volumetric DLR source term and the VSTG

In this section, the performance of two volumetric source terms is evaluated. The first is the DLR source term that is implemented in a volumetric manner, and the second is the VSTG. In this assessment, the forcing region used for both source terms is half a boundary layer thickness ($0.5\delta_0$). The results of volumetric forcing are always shown in the middle of the forcing region. Both source terms are applied with and without the sink term described in Equation 7.6.

The outcomes of using the two volumetric source terms are shown in Figure 7.6. The sink term does not result in any additional decrease in eddy viscosity with the DLR source term, and only a slight decrease is observed with the VSTG. Nevertheless, this further decrease in eddy viscosity has minimal impact on the resolved and modeled stresses as well as the velocity profile. This negligible decrease in eddy viscosity is due to enforcing the WMLES branch of IDDES by setting $f_{dt} = 1$, which results in already low eddy viscosity levels. A comparison between the VSTG and the volumetric DLR source terms reveals that the latter produces resolved stresses which are in a better agreement with the target stresses. This is to be expected, since the DLR source term forces the flow to generate fluctuations that are equal to the synthetic velocities produced by the synthetic turbulence generator. Since the statistics of the synthetic velocities approximate the target Reynolds stresses, the generated (resolved) fluctuations will also match the target Reynolds stresses.

The results of the volumetric forcing methods 3 δ_0 downstream of the interface are shown in Figure 7.7. The resolved stresses obtained from both forcing methods exhibit similarities, with the result of VSTG showing higher values at around $x/\delta_0 = 0.25$ in both $<u'v'>$ and $<v'v'>$, as depicted in Figure 7.7c and Figure 7.7f, respectively. However, the resolved shear stress better aligns with the target in the outer boundary layer when using the VSTG compared to the volumetric DLR source term.

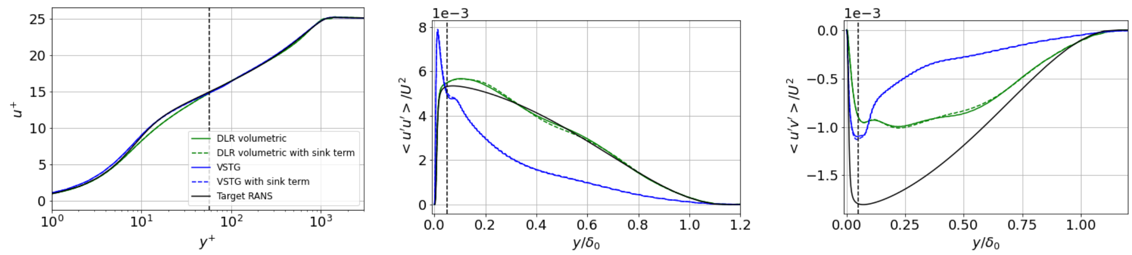

(a) u^+ **(b)** Resolved $<u'u'>$ **(c)** Resolved $<u'v'>$

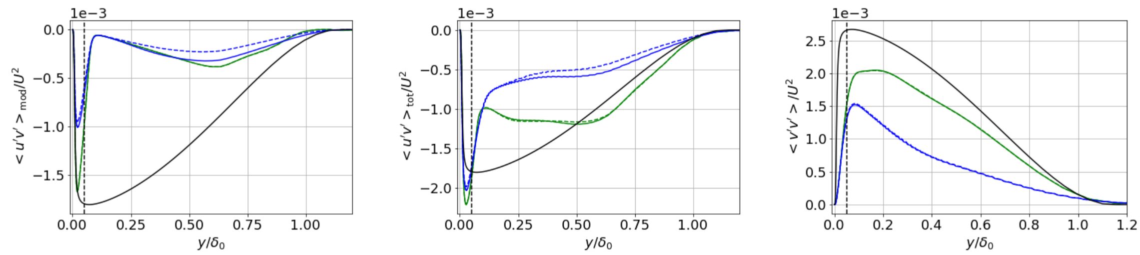

(d) Modeled $<u'v'>$ **(e)** Total $<u'v'>$ **(f)** Resolved $<v'v'>$

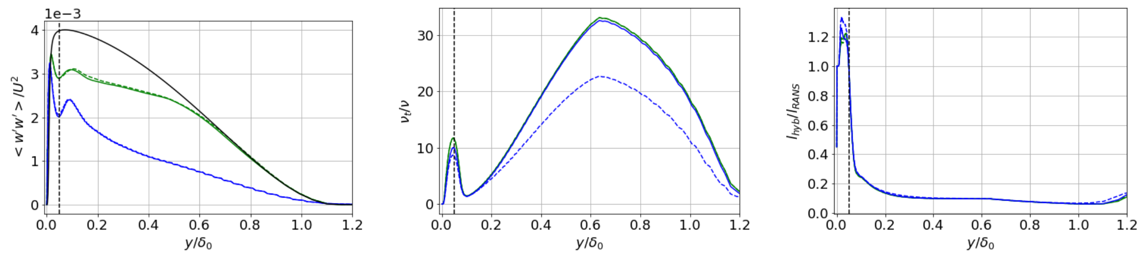

(g) Resolved $<w'w'>$ **(h)** ν_t **(i)** l_{hyb}/l_{RANS}

Figure 7.6: Results of volumetric forcing for the flat plate case at $x = 0.25\delta_0$. The forcing region size is 0.5 δ_0.

The skin friction coefficient and the pressure fluctuations obtained using the two volumetric forcing terms are shown in Figure 7.8. Once again, the lack of influence of using the sink term to further decrease the eddy viscosity is shown in both C_f and the pressure fluctuations. Moreover, the result of VSTG exhibits a peak in C_f comparable to that of the interface forcing. The advantage of the VSTG is shown in the pressure fluctuations in Figure 7.8b, where the spike in pressure fluctuations is significantly reduced with the VSTG. It is also observed that even the volumetric DLR source term shows significant spurious pressure fluctuations. So, even with the use of blending functions, the volumetric DLR source term still fails to treat these spurious pressure fluctuations. This is in agreement with the original publication of the volumetric DLR source term Probst et al. [22]. The issue of spurious pressure fluctuations is treated in chapter 8.

In terms of the spurious pressure fluctuations, it is apparent that the VSTG source term has an advantage over the DLR source term. In the VSTG publication, it was found that larger forcing regions, exceeding the $0.5\delta_0$ that is employed in this subsection, yield superior outcomes. Thus, it would be unjust to solely evaluate suboptimal forcing regions for the VSTG. The effect of the forcing region size is addressed in the next subsection.

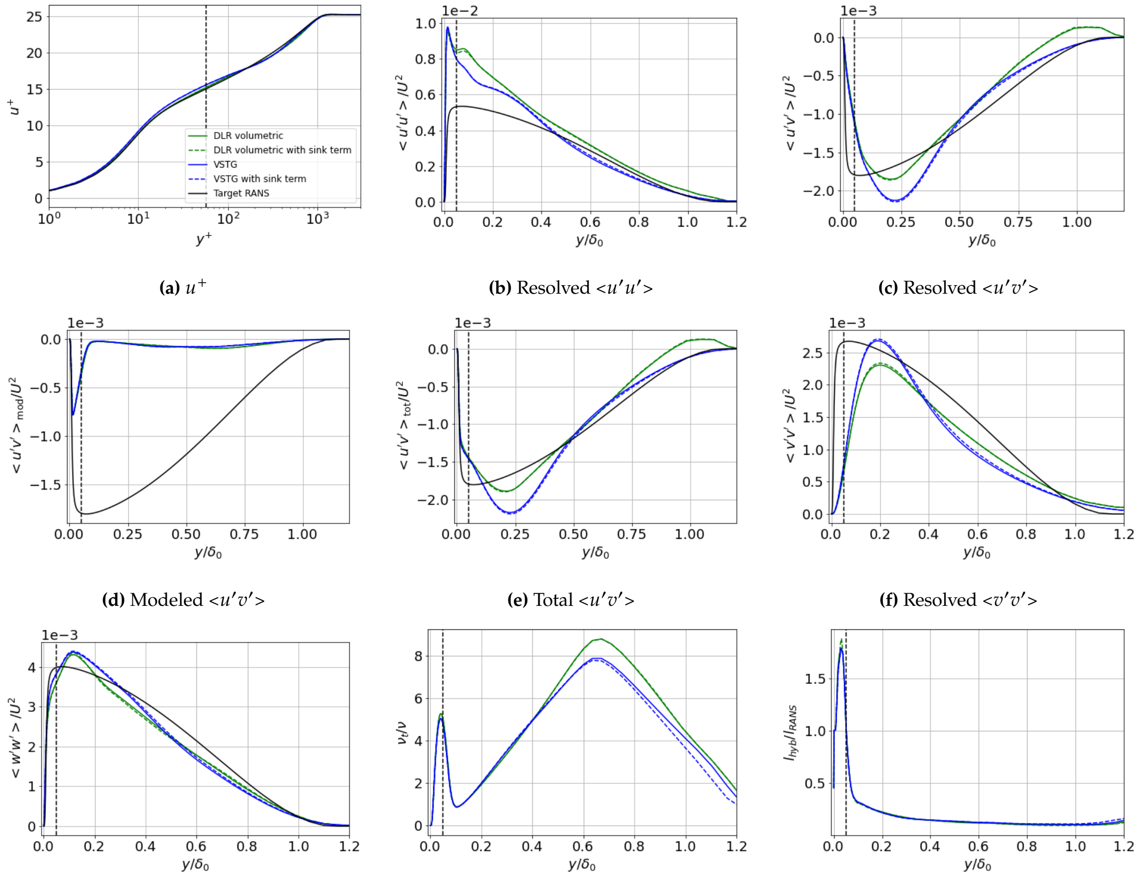

(a) u^+ **(b)** Resolved $<u'u'>$ **(c)** Resolved $<u'v'>$

(d) Modeled $<u'v'>$ **(e)** Total $<u'v'>$ **(f)** Resolved $<v'v'>$

(g) Resolved $<w'w'>$ **(h)** ν_t **(i)** l_{hyb}/l_{RANS}

Figure 7.7: Results of volumetric forcing for the flat plate case at $x = 3\delta_0$. The forcing region size is $0.5\ \delta_0$.

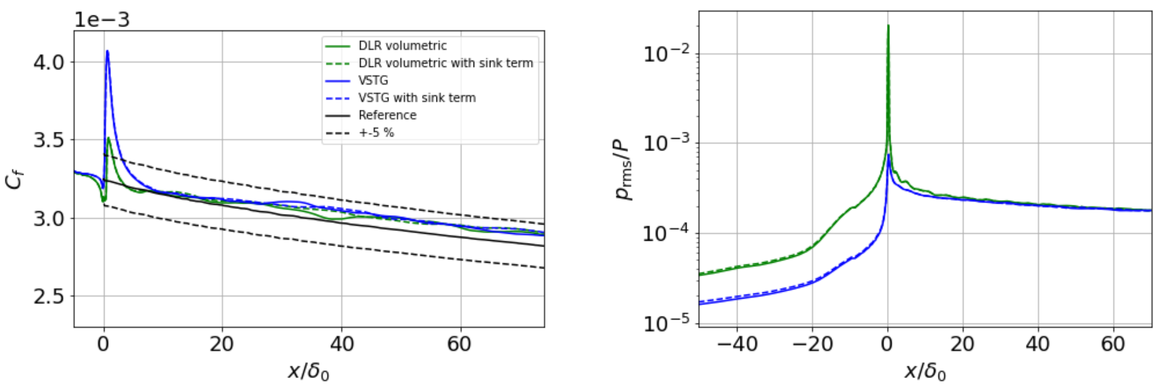

(a) C_f **(b)** Pressure fluctuations

Figure 7.8: Skin friction coefficient and pressure fluctuations for the flat plate case using volumetric source terms. The forcing region size is $0.5\ \delta_0$.

7.3.3. Effect of the forcing region in VSTG

The impact of increasing the forcing region with the VSTG is assessed in this subsection. The VSTG source term was used in a forcing region of length $1\delta_0$ and $2\delta_0$ in addition to 0.5δ that was already presented in subsection 7.3.2. The results of these computations in the middle of the forcing region of size $2\delta_0$, namely at $x = 1\delta_0$, can be found in Appendix A. More importantly, the results of these computations at a distance of $3\delta_0$ downstream of the interface are shown in Figure 7.9. Once again, the sink term shows no influence on the results. This is because the WMLES branch of IDDES is imposed, and thus the eddy viscosity levels are already sufficiently low. The resolved stresses appear to match the target slightly better when the forcing region = 1δ, as shown in Figure 7.9c. This is because the flow had a greater distance downstream of the forcing region to adapt to the correct Reynolds stress values. Nonetheless, the difference between the results using the two forcing regions is acceptable.

The surface quantities are of more interest, the results are shown in Figure 7.10. The peak in both C_f and the pressure fluctuations relaxes as the forcing region size increases. This is in agreement with the original publication [15]. The sudden decrease in C_f, present with forcing region size = $2\delta_0$, is also consistent with the original publication. However, the original publication shows results at a smaller Re_θ and over a smaller range of Re_θ, so it is hard to establish a one-to-one correlation. Nonetheless, the presented results show good agreement with the original publication.

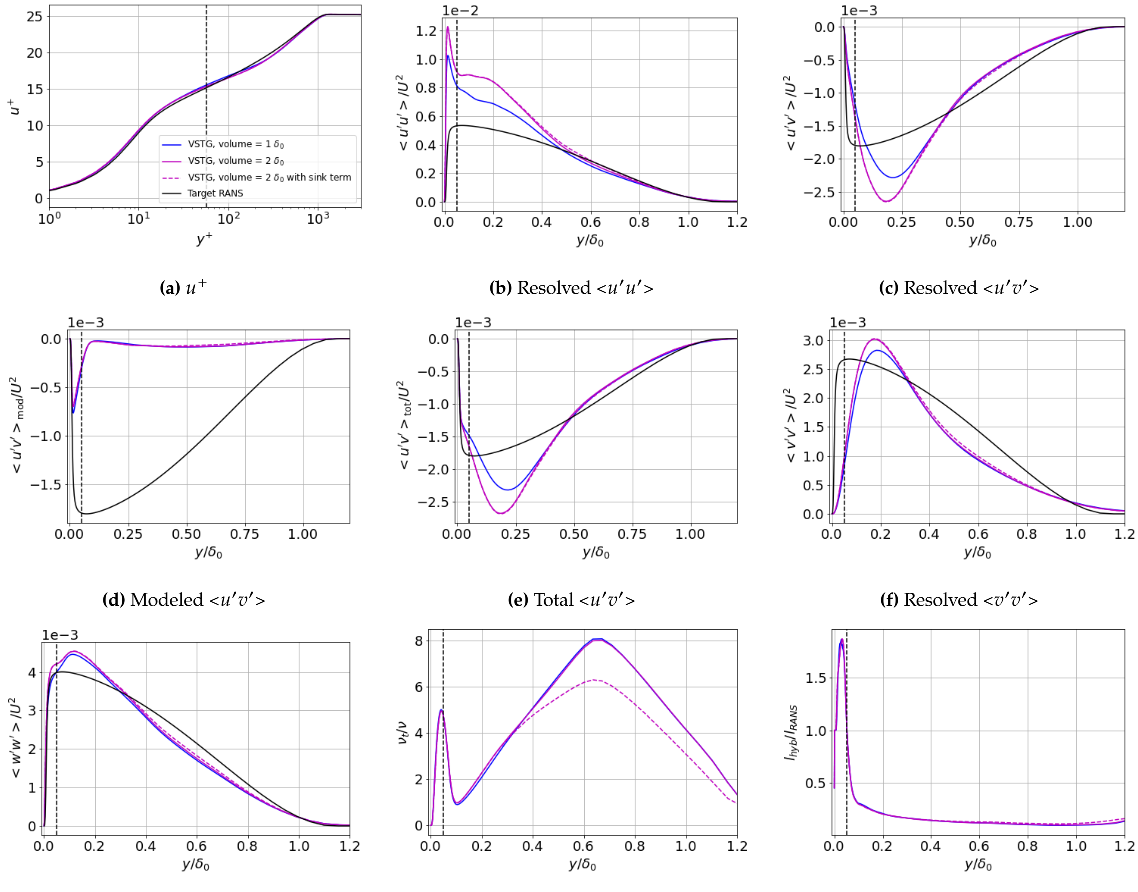

(a) u^+ (b) Resolved $<u'u'>$ (c) Resolved $<u'v'>$

(d) Modeled $<u'v'>$ (e) Total $<u'v'>$ (f) Resolved $<v'v'>$

(g) Resolved $<w'w'>$ (h) ν_t (i) l_{hyb}/l_{RANS}

Figure 7.9: Results of the VSTG forcing with different forcing region sizes for the flat plate case at $x = 3\delta_0$. The forcing region sizes are $1\delta_0$and$2\delta_0$.

In this chapter, different synthetic turbulence forcing methods were evaluated. To summarize, using SA and k-ω SST as the underlying RANS models produced similar results in terms of velocity profiles and resolved Reynolds stresses. However, the skin friction coefficient resulting from SST-IDDES, unlike its counterpart, showed a larger deviation with respect to the reference. It was found that SST-IDDES is more sensitive to the random number set used in the NTS-STG. Increasing the number of Fourier modes by modifying the mode distribution could treat this issue. However, this is not explored in this work, since SA is used as the main underlying RANS model.

Regarding the volumetric forcing, it was found that a further decrease in eddy viscosity by using additional sink terms does not gain any benefit with any of the source terms. This is believed to be because the eddy viscosity levels are already sufficiently low as a result of manually imposing the WMLES branch (by setting $f_{\mathrm{dt}} = 1$). These sink terms could be more beneficial in cases where such manual enforcement of the WMLES branch is not applied.

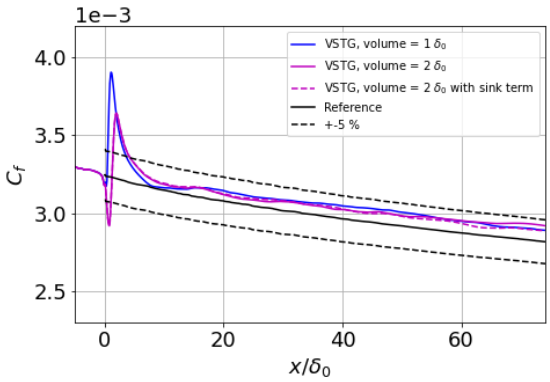

(a) C_f

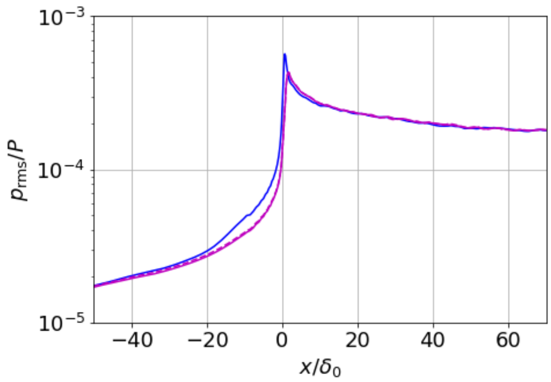

(b) Pressure fluctuations

Figure 7.10: Skin friction coefficient and pressure fluctuations for the flat plate case using VSTG forcing with different forcing region sizes. The forcing region sizes are $1, 2\ \delta_0$.

The DLR source term showed better agreement with the target stresses, in the forcing region/interface and downstream of the interface, compared to the VSTG. Nonetheless, both source terms showed a deficit in resolved stresses in the forcing regions. On the other hand, the VSTG source term clearly exceeds over the DLR source term in terms of the lower level of spurious noise, indicated by significantly smaller pressure fluctuations. The volumetric DLR source term did not show an improvement in this respect, even though it uses a blending function to gradually introduce the synthetic velocities into the flow. The issue of spurious noise with the DLR source term as well as the deficit in the resolved stresses in the forcing region with both source terms is discussed in the next chapter.

8

Improved Synthetic Turbulence Forcing

In this chapter, two improvements to the forcing methods are proposed. Even though the resolved Reynolds stresses obtained using the DLR source term show good agreement with the target Reynolds stresses compared to the VSTG, shortcomings were encountered. these shortcomings motivate the proposed modifications. As discussed in chapter 7, the DLR interface forcing was found to cause a spike in the skin friction coefficient at the interface, an issue partially treated by the volumetric forcing. Furthermore, both DLR interface and volumetric source terms resulted in significant spurious noise, indicated by a pressure fluctuations spike at the RANS-LES interface. Such nonphysical pressure fluctuations pollute the computational domain, and could have a negative impact on the solution downstream of the interface. The other shortcoming, which both the DLR source term and the VSTG encountered, is that some resolved stresses were underestimated in and downstream of the forcing region.

The first shortcoming is treated by limiting the forcing to the LES-treated region of the boundary layer, which is referred to as constrained forcing. The second is treated by introducing additional production terms that increase the production of the underestimated resolved stresses, which is achieved through dynamic forcing. The constrained forcing and dynamic forcing are discussed in section 8.1 and section 8.2, respectively.

8.1. Constrained Forcing

The first modification is based on the idea of not injecting synthetic turbulence in the near-wall RANS region. This is thought to be a more physically sound approach, as the eddy viscosity in the RANS region is sufficient to fully model the Reynolds stresses. In fact, when injecting synthetic turbulence in the RANS region, resolved stresses are added to the already existing modeled stresses, which is undesirable as it results in too large total stresses. Recall that in the IDDES formulation, the hybrid length scale is deliberately increased near the RANS-LES interface in the boundary layer (using the elevation function f_e) to prevent excessive reduction in the modeled stresses near the interface. This ensures sufficiently large modeled stresses in the near-wall region up to the interface. Therefore, there is no need to add resolved stresses in this region.

In this work, it is proposed to constrain the source term from being active in the near-wall RANS region, which is referred to as the constrained forcing hereafter. With the constrained forcing, it is aimed to obtain a more accurate estimation of the total turbulent shear stress. Furthermore, the constrained forcing aims at reducing the peak in the skin friction coefficient and pressure fluctuations, appearing at the interface. These nonphysical peaks were persistent even when using the volumetric DLR source term.

Another approach that aims to avoid adding resolved stresses to modeled ones is that introduced by Probst et al. [22]. In their publication, it was proposed to adjust the target Reynolds stress such that the modeled stresses at the interface are subtracted from the target stresses. So, that approach considered the whole boundary layer, not only the near-wall region. One concern with that approach is that the eddy viscosity downstream of the RANS-LES interface could be decreasing at a faster rate than the rate at which synthetic turbulence is developing. That is, the modeled stress may vanish quickly downstream of the interface, leaving only the resolved stresses to match the target stresses. This would lead to total stresses that match the adjusted target stresses, but still underestimate the correct Reynolds stress downstream of the interface. Because with the lower viscosity level downstream of the interface, the adjusted target would underestimate the correct Reynolds stresses. This possible issue is not reported in the original publication, but merely anticipated by the author of this work. The approach presented in this work is simpler and not prone to this risk.

To differentiate between the RANS and the LES regions, the f_B function that blends between the two regions in IDDES was used. The source term is then scaled by the factor $1 - f_B$ to ensure no forcing takes place in the near-wall RANS region, while rapidly increasing the source term intensity to 1 in the LES region. Both f_b and $1 - f_b$ are shown in Figure 8.1. The vertical dashed line indicates the RANS-LES interface in the boundary layer. The constrained forcing was applied to the DLR source term as follows:

$$F_i = (1 - f_b)\frac{\partial\left(\rho u_i'\right)}{\partial t} \approx (1 - f_b)\frac{3\left(\rho u_i'\right)^{n+1} - 4\left(\rho u_i'\right)^{n} + \left(\rho u_i'\right)^{n-1}}{2\Delta t} \tag{8.1}$$

The results of this modified forcing are discussed in subsection 8.3.1.

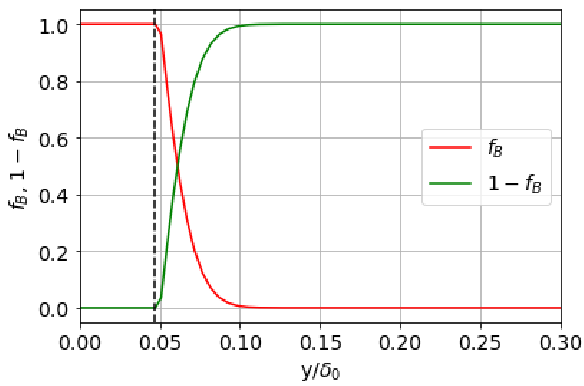

Figure 8.1: f_b and $1 - f_b$ functions used in the constrained forcing

8.2. Dynamic Forcing

The second proposed modification has the purpose of addressing the deficit in resolved stresses, observed in and downstream of the forcing region. The aim is to evaluate the impact of using an additional source term that seeks to closely match the target Reynolds stresses in the forcing region. This impact is not only limited to the resolved Reynolds stresses, but it also includes the skin friction coefficient. The end goal is, as always, to achieve a faster adaptation in terms of both the resolved stresses and the skin friction coefficient. The impact of this additional source term on the adaptation length is evaluated. The additional source term is inspired by the dynamic forcing of [32].

As described in chapter 7, the forcing of synthetic turbulence is achieved through a source term in the momentum equations. The filtered momentum equation for an incompressible flow with an additional source term f_i is considered,

$$\frac{\partial \widetilde{u}_i}{\partial t} + \widetilde{u}_j\frac{\partial \widetilde{u}_i}{\partial x_j} = -\frac{1}{\rho}\frac{\partial \widetilde{p}}{\partial x_i} + \upsilon\frac{\partial^2 \widetilde{u}_i}{\partial x_j \partial x_j} - \frac{\partial \tau_{ij}}{\partial x_j} + f_i \tag{8.2}$$

The source term f_i can be divided into a Reynolds-averaged part $\langle f_i \rangle$ and its fluctuating part f_i' as,

$$f_i = \langle f_i \rangle + f_i' \tag{8.3}$$

Using this decomposition, the contribution of the source term to the mean flow and to the resolved stresses are isolated. The contribution of the source term f_i to the mean filtered momentum equation reads

$$\frac{\partial \langle \widetilde{u_i} \rangle}{\partial t} + \frac{\partial}{\partial x_j} \left(\langle \widetilde{u_i} \rangle \langle \widetilde{u_j} \rangle \right) = -\frac{1}{\rho} \frac{\partial \langle \tilde{p} \rangle}{\partial x_i} + v \frac{\partial^2 \langle \widetilde{u_i} \rangle}{\partial x_j^2} - \frac{\partial}{\partial x_j} \left\langle u_i' u_j' \right\rangle - \frac{\partial \left\langle \tau_{ij} \right\rangle}{\partial x_j} + \langle f_i \rangle \tag{8.4}$$

where $u_i' = \widetilde{u_i} - \langle \widetilde{u_i} \rangle$, such that $\left\langle u_i' u_j' \right\rangle$ are the resolved Reynolds stresses. It is to be expected that only the averaged part of the source term affects the mean flow. It is of more interest to examine the contribution of the fluctuating part of the source term f_i' to the resolved stresses, which reads,

$$\frac{\partial \left\langle u_i' u_j' \right\rangle}{\partial t} + \left\langle \tilde{u_j} \right\rangle \frac{\partial \left\langle u_i' u_j' \right\rangle}{\partial x_j} = P_{ij}^r + P_{ij}^f + \phi_{ij}^r + \chi_{ij} + D_{ij}^{Tr} + D_{ij}^{\tau} + D_{ij}^{vr} - \varepsilon_{ij}^r \tag{8.5}$$

where P_{ij}^r, ϕ_{ij}^r, D_{ij}^{Tr}, D_{ij}^{vr}, and ε_{ij}^r are the resolved production, pressure-strain, turbulent diffusion, viscous diffusion, and dissipation terms, analogous to those found in the unfiltered Reynolds stress equations. The forcing term contribution appears in the additional term P_{ij}^f:

$$P_{ij}^f = \left\langle f_i' u_j' \right\rangle + \left\langle f_j' u_i' \right\rangle \tag{8.6}$$

Only the fluctuating part of the source term affects the development of the resolved stresses through the source/sink term P_{ij}^f. This term can increase or dampen the resolved stresses based on its sign. As discussed in chapter 7, a deficit in resolved stresses was observed, especially in $\langle u'v' \rangle$ and $\left\langle v'^2 \right\rangle$. Adding a source term that selectively increases the production of these underestimated stresses is expected to fix this deficit.

Consider the dynamic forcing proposed by Laraufie et al. [32], and given by,

$$f_i = r v' \delta_{i2} \tag{8.7}$$

This forcing term has no direct effect on the mean flow since $\langle f_i \rangle = 0$. It only affects turbulent fluctuations, as intended in this application. The resolved stress production tensor of this forcing term is

$$P_{11}^f = P_{13}^f = P_{33}^f = 0, \quad P_{22}^f = 2r \left\langle v'^2 \right\rangle, \quad P_{12}^f = r \langle u'v' \rangle, \quad P_{23}^f = r \langle v'w' \rangle. \tag{8.8}$$

The proportional integral control factor is

$$r = \Gamma \left(\langle v'v' \rangle^{\dagger} - \langle v'v' \rangle \right), \tag{8.9}$$

where Γ is a dimensional parameter ($\Gamma \equiv [\mathrm{mskg}^{-1}]$) that determines the intensity of the dynamic forcing. The shear stress production P_{12}^f due to this source term is positive when $\langle v'v' \rangle$ is smaller than the target value $\langle v'v' \rangle^{\dagger}$, tending to adjust the resolved wall normal stress to the target. Thus, from a statistical perspective, the forcing selectively generates resolved stresses $\langle u'v' \rangle$, $\left\langle v'^2 \right\rangle$, and $\langle v'w' \rangle$, at a rate dependent on the difference between the resolved and target wall normal stress $\langle v'v' \rangle$. The control factor r decreases to zero as the target is approached, causing the forcing term to vanish. This additional forcing term was used to treat the deficit in resolved stress $\langle u'v' \rangle$, $\langle v'v' \rangle$, observed in the forcing region.

This dynamic forcing is based on the dynamic forcing of Spille-Kohoff et al. [33]. In the latter, the proportional controller used $\Gamma \left(\langle u'v' \rangle^{\dagger} - \langle u'v' \rangle \right)$ instead of the controller given in Equation 8.9. However, Laraufie et al. [32] found that using the proportional control in Equation 8.9 results in much smaller adaptation lengths in terms of C_f. Therefore, this controller is used in this work.

The original publication found that the sum of non-dimensional Γ over the number of forcing planes $\sum \Gamma \cdot (\rho U \delta_0) = 19,000$, results in fast adaptation length in terms of C_f [32]. However, using this value in the flat plate test case did not show significant effect. This could be attributed to multiple reasons. The first is that when using the DLR source term, the resolved stresses already match the target stresses fairly well. The second reason is that the forcing region used in this work is significantly smaller than that used in [32]. In the former, the forcing region used is $= 0.5\delta_0$, whereas the latter used a forcing region $\approx 7\delta_0$. Furthermore, the original publication used the synthetic eddy method (SEM) of Pamiès et al. [34] as the method of generating synthetic turbulence, as opposed to the NTS-STG which is used in this work. It was found that substantial impact of the dynamic forcing can be achieved with a non-dimensional Γ with the value of $\sum \Gamma \cdot (\rho U \delta_0) = 380,000$.

8.3. Results

The results of the two proposed modifications are discussed in this section. First, the results of the constrained forcing are presented for both the flat plate and the rounded step in subsection 8.3.1. Then, the results of the dynamic forcing for the flat plate are discussed in subsection 8.3.2.

8.3.1. Results of the constrained forcing

In this subsection, the outcomes of the constrained forcing are discussed. The constrained forcing was applied to the DLR source term in an interface forcing setup. The velocity profile, Reynolds stresses, and turbulent viscosity at the interface are shown in Figure 8.2. Firstly, when using the constrained forcing, the velocity profile no longer suffers from a mismatch with respect to the RANS target profile as shown in Figure 8.2a. This mismatch can be attributed to disturbed velocity gradients in the near-wall RANS region, observed when synthetic turbulence is injected in that region.

Secondly, there is a consistent lack of resolved stresses in the near-wall region, as expected, since no synthetic turbulence was injected in that region. It is also observed that the RANS region still shows some resolved content. When considering the total shear stress in Figure 8.2e, one can see that with the constrained forcing, the total shear stress is much better estimated. This is a result of not adding resolved and to the modeled stresses in the near-wall region, as intended. So, the proposed constrained forcing does not seek to ensure resolved stresses in the RANS region, but only to maintain the sufficient modeled stresses in that region. Finally, turbulent viscosity remains unaffected, as shown in Figure 8.2h The results of the constrained forcing at a distance of $3\delta_0$ downstream of the interface are shown in

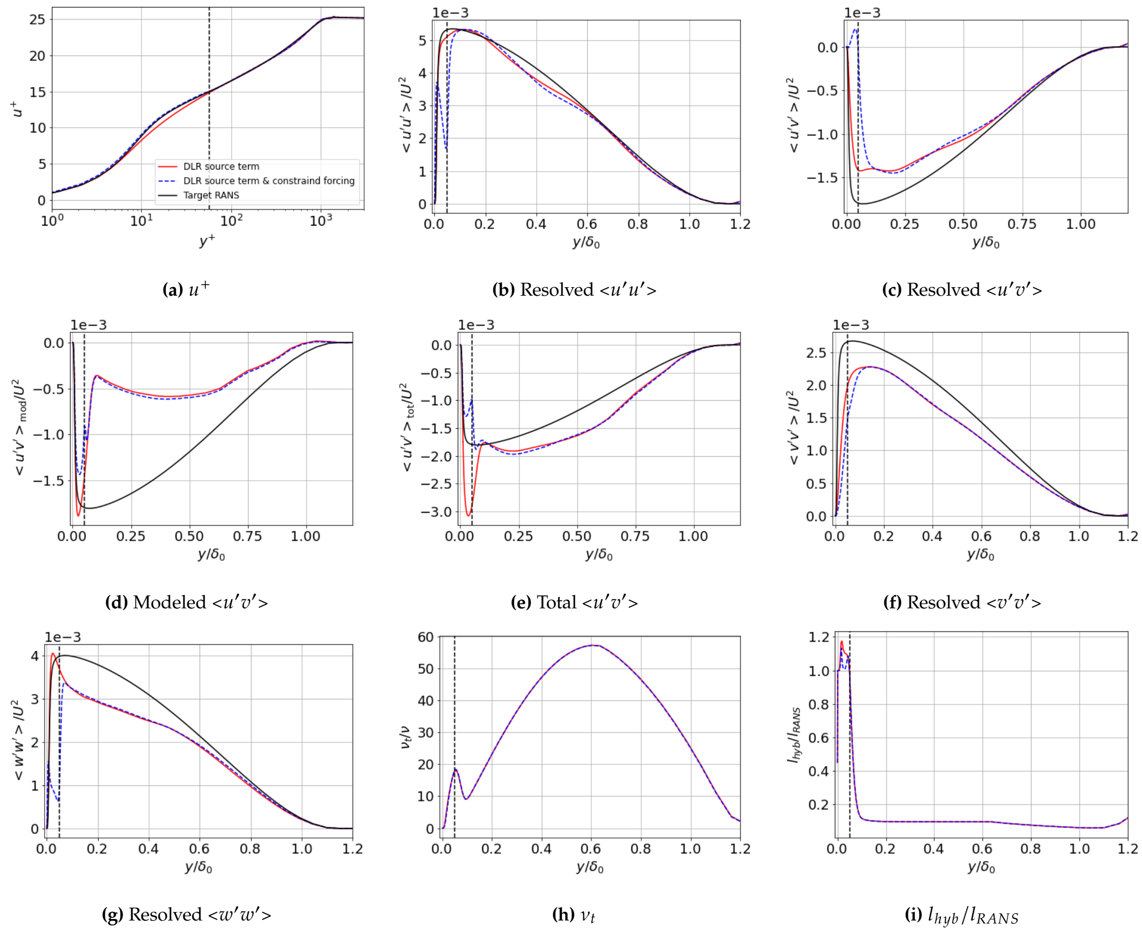

(a) u^+ (b) Resolved $<u'u'>$ (c) Resolved $<u'v'>$

(d) Modeled $<u'v'>$ (e) Total $<u'v'>$ (f) Resolved $<v'v'>$

(g) Resolved $<w'w'>$ (h) ν_t (i) l_{hyb}/l_{RANS}

Figure 8.2: Results of the DLR source term and constrained forcing for the flat plate case at the interface (x = 0)

Figure 8.3. There is no observable difference between using the constrained forcing and the standard interface forcing. So, the influence of not injecting synthetic turbulence in the near-wall region is local, and the flow manages to produce resolved turbulence in a normal manner downstream of the interface.

Therefore, when using the constrained forcing, one can avoid the undesirable effects of injecting synthetic turbulence in the RANS-treated region without negatively impacting the development of turbulence downstream of the interface.

Of high interest are the skin friction coefficient and pressure fluctuations, presented in Figure 8.4. The large peak in C_f at the interface was significantly reduced when using the constrained forcing, as shown in Figure 8.4a. Furthermore, the sudden decrease in C_f preceding the interface is no longer present. These two effects can be attributed to less disturbed velocity gradients in the near wall region when the constrained forcing is used. This is depicted in Figure 8.5, where the use of constrained forcing results in much less distributed velocity gradients. Such disturbed velocity gradients with a constant ν at the wall lead to the disturbances observed in the skin friction coefficient.

Regarding the spurious noise, the spike in the pressure fluctuations is reduced to a fourth of its typical value when the constrained forcing is used. This is because the near-wall RANS region is not disturbed with injected synthetic turbulence when the constrained forcing is used. These results are encouraging as they address the two issues associated with the sudden onset of turbulence, without hindering the turbulence development downstream of the interface.

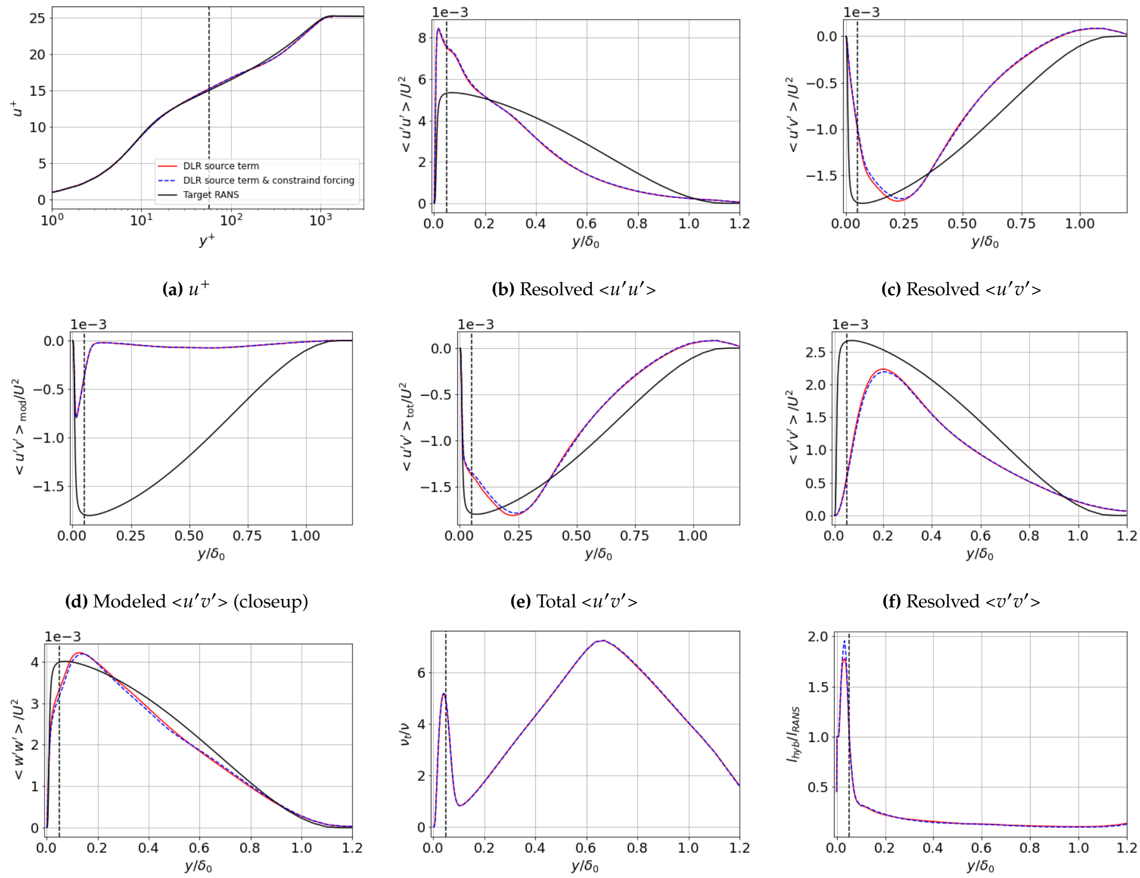

(a) u^+ **(b)** Resolved $<u'u'>$ **(c)** Resolved $<u'v'>$

(d) Modeled $<u'v'>$ (closeup) **(e)** Total $<u'v'>$ **(f)** Resolved $<v'v'>$

(g) Resolved $<w'w'>$ **(h)** ν_t **(i)** l_{hyb}/l_{RANS}

Figure 8.3: Results of the DLR source term and constrained forcing for the flat plate case at $x = 3\delta_0$

The constrained forcing was also used in the rounded step case. The constrained forcing was combined with both the interface and the volumetric forcing of the DLR source term, denoted DLR source term and DLR volumetric, respectively, in Figure 8.6. The result of the DLR source term are shown at the interface, whereas the results of the volumetric DLR are shown at the middle of the forcing region, which has a size of 0.5 δ_0. This makes the comparison unfair towards the interface forcing. Nonetheless, the purpose is not compared the interface forcing and the volumetric forcing, but merely to observe the behavior of the constrained forcing when combined with the volumetric forcing.

It can be seen the velocity profile at the interface is better captured by the volumetric forcing, whereas

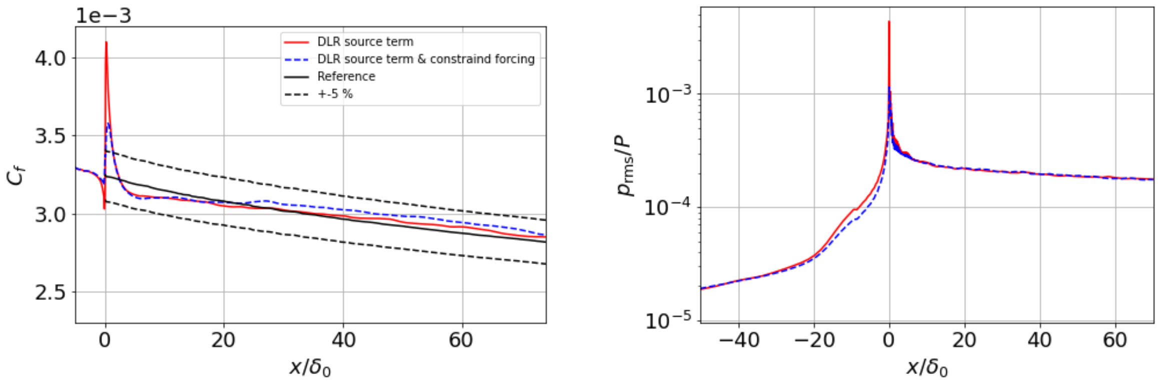

(a) C_f **(b)** Pressure fluctuations

Figure 8.4: Friction coefficient and pressure fluctuations for the flat plate case using The DLR source term and constrained forcing

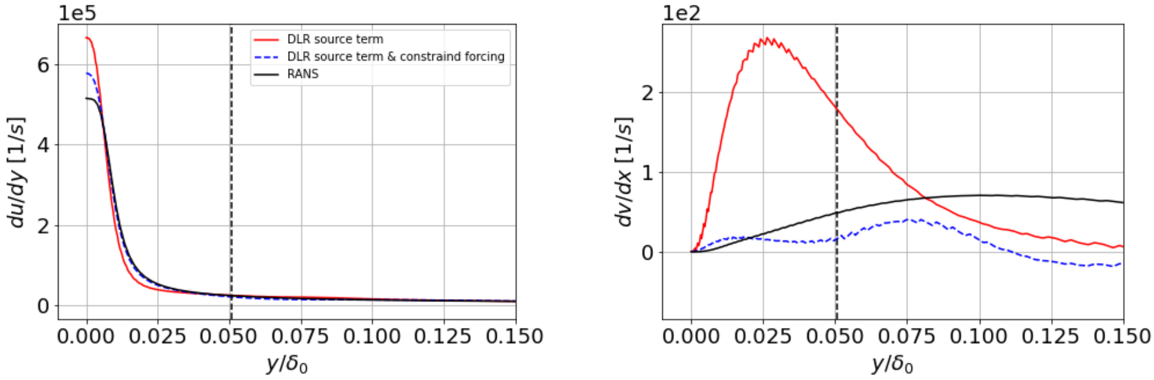

(a) du/dy **(b)** dv/dx

Figure 8.5: Velocity gradients for the flat plate at $x = 0.25\ \delta_0$ using the DLR source term and constrained forcing

the interface forcing deviates from the LES profile even when the constrained forcing is used as shown Figure 8.6a. Recall that the results of the volumetric forcing are more downstream compared to those of the interface forcing. The difference in the velocity profiles is related to this reason. When the interface forcing is combined with the constrained forcing, there is a lack of resolved stresses in the near-wall region, which is expected, and depicted in Figure 8.6c and Figure 8.6d. This is mostly the case when volumetric forcing is combined with constrained forcing, except for the resolved spanwise Reynolds stress, shown in Figure 8.6h, which exhibits large magnitudes in the near-wall region. This behavior is not expected, as no synthetic turbulence forcing was performed in this region. Nonetheless, these large magnitudes vanish rapidly downstream of the forcing region. Figure 8.6f shows that using the constrained forcing results in a smaller overestimation of the total turbulent shear stress for both the interface and the volumetric forcing, thanks to less resolved turbulence in the RANS region.

The results of the constrained forcing around the rounded step are shown in Figure 8.7. The different forcing approaches show very similar results. It is encouraging to see that the constrained forcing does not hinder the development of turbulence in any form. In fact, constrained forcing results show a better agreement with the LES data compared to their respective standard DLR forcing. This can be observed especially downstream of the rounded step in the resolved Reynolds stresses, shown in Figure 8.7d, Figure 8.7g, and Figure 8.7h.

Finally, the friction and pressure coefficients are shown in Figure 8.8. The peak in C_f is significantly reduced when the constrained forcing is combined with interface forcing. However, such a result is not achieved with volumetric forcing, which is another unexpected behavior appearing when combining the volumetric DLR source term with the constrained forcing. Nonetheless, the skin friction computed with the constrained forcing converges with that of its respective standard forcing rapidly downstream

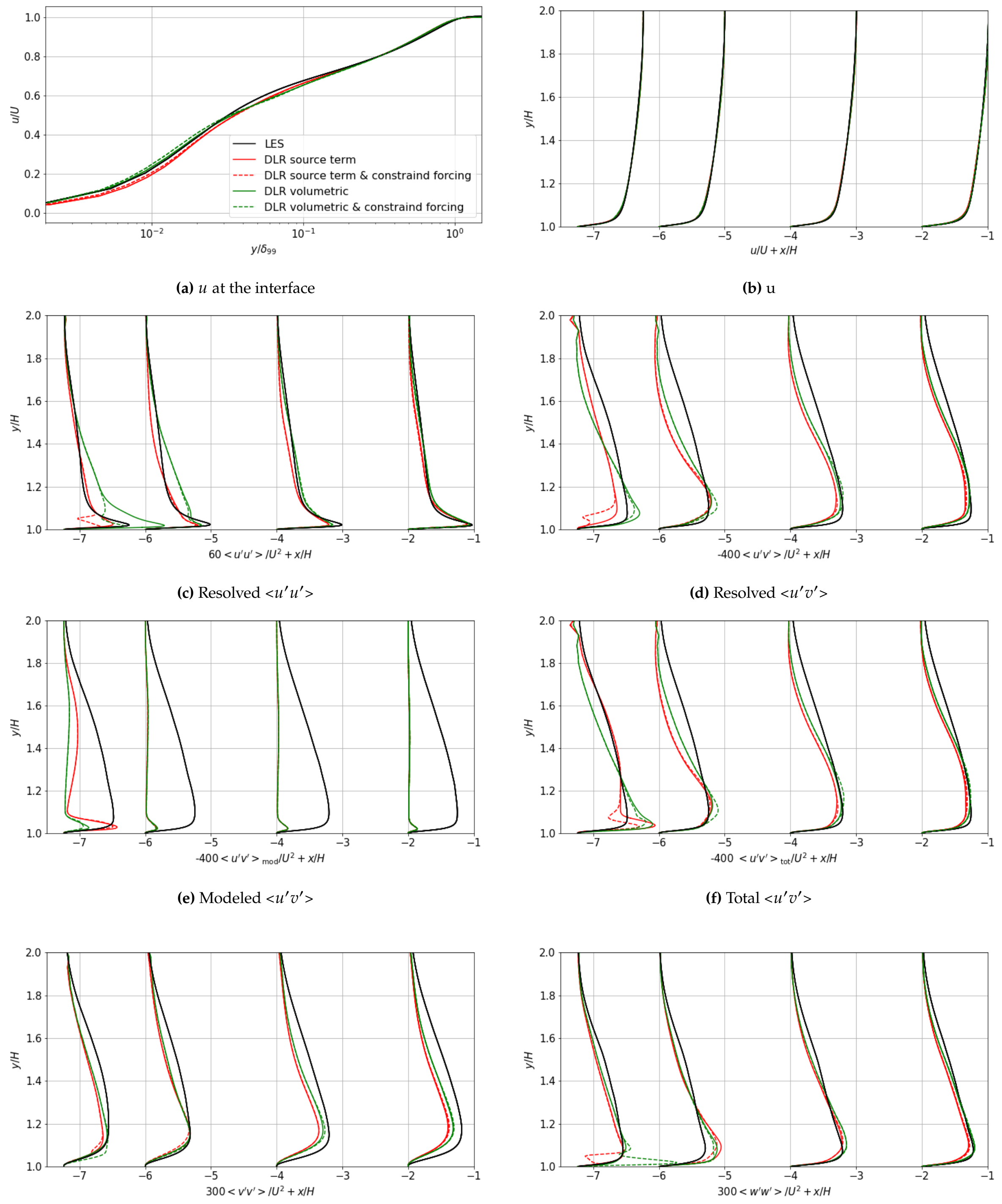

(a) u at the interface

(b) u

(c) Resolved $<u'u'>$

(d) Resolved $<u'v'>$

(e) Modeled $<u'v'>$

(f) Total $<u'v'>$

(g) Resolved $<v'v'>$

(h) Resolved $<w'w'>$

Figure 8.6: Results of the constrained forcing combined with both the interface and the volumetric forcing of the DLR source term for the rounded step case. The results are shown at the upstream region.

of the interface/forcing region. That is to say, no negative effects of the constrained forcing are observed downstream of the interface. Regarding the pressure coefficient, the results of the different forcing methods agree to a large extent, as shown in Figure 8.8b.

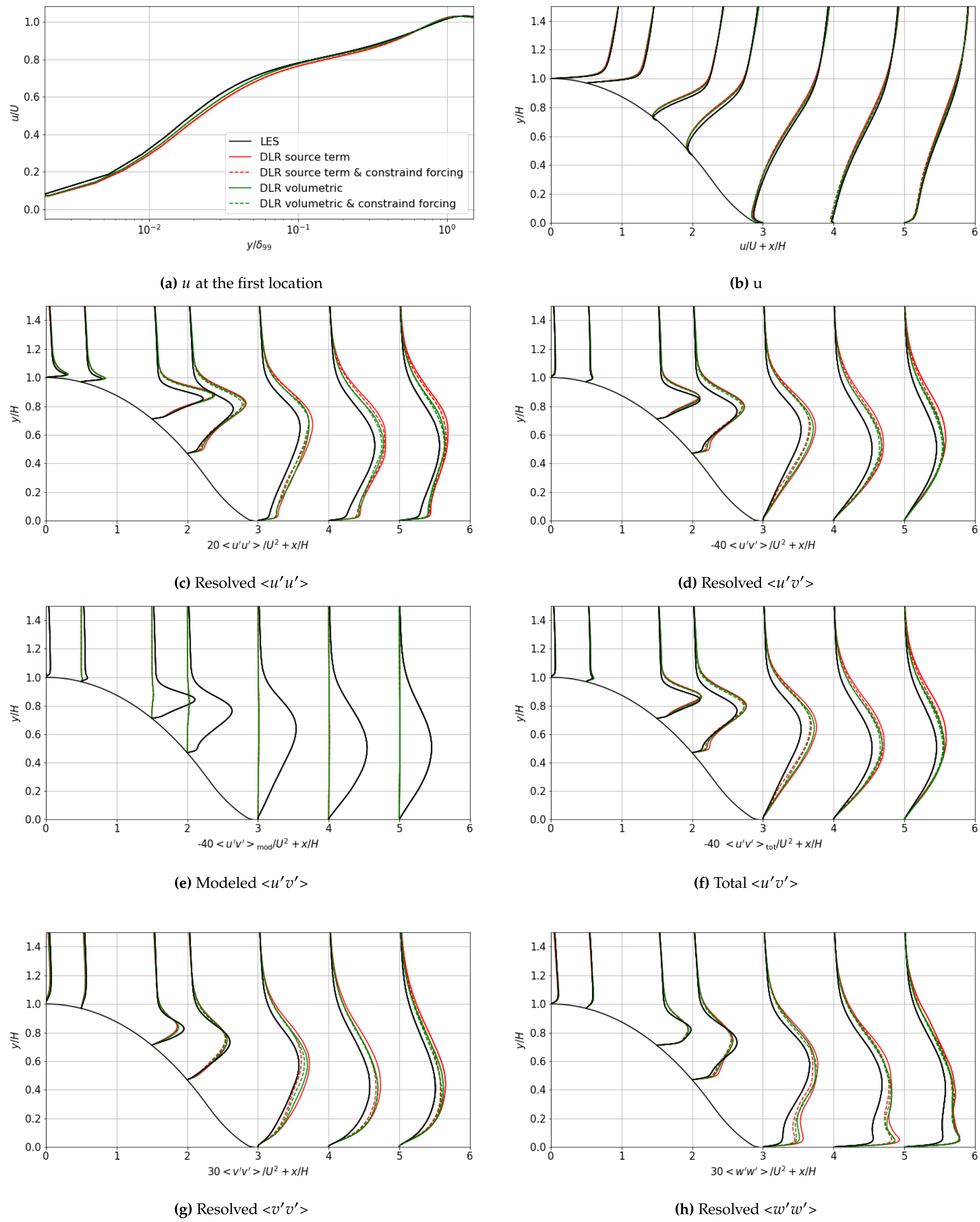

(a) u at the first location

(b) u

(c) Resolved $<u'u'>$

(d) Resolved $<u'v'>$

(e) Modeled $<u'v'>$

(f) Total $<u'v'>$

(g) Resolved $<v'v'>$

(h) Resolved $<w'w'>$

Figure 8.7: Results of the constrained forcing combined with both the interface and the volumetric forcing of the DLR source term for the rounded step case. The results are shown at the curved step region

8.3.2. Results of dynamic forcing

In this subsection, the results of the dynamic forcing applied to the flat plate test case are presented. The dynamic forcing was applied along with the volumetric DLR forcing to selectively increase the production term of specific resolved Reynolds stresses that are consistently underestimated. The results of the dynamic forcing at the middle of the forcing region are shown in Figure 8.9. Since the mean of the

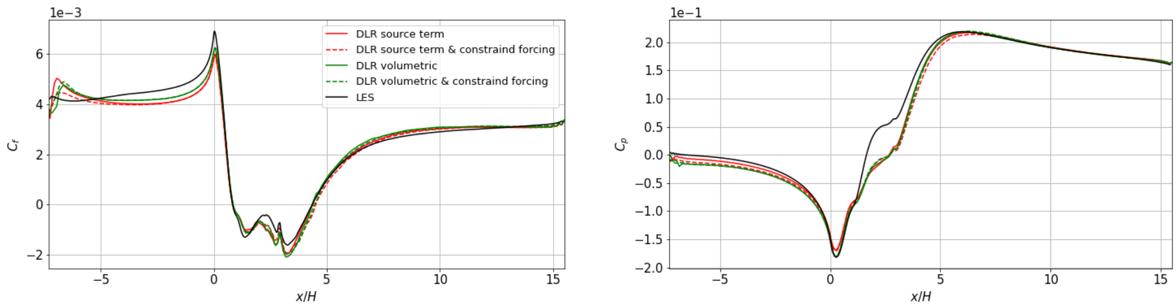

(a) C_f **(b)** C_p

Figure 8.8: Skin friction and pressure coefficients using the constrained forcing combined with both the interface and the volumetric forcing of the DLR source term for the rounded step case.

dynamic forcing term is zero, it does not alter the velocity profile, as shown in Figure 8.9a. Furthermore, the dynamic forcing results in a significant increase in the wall-normal stress, and a slight increase in the turbulent shear stress, depicted in Figure 8.9f and Figure 8.9c, respectively. The larger increase in the wall-normal stress compared to the turbulent shear stress is a direct consequence of the proportional controller in Equation 8.9, which considers only wall-normal stress. Note that, the dynamic forcing doesn't increase the streamwise Reynolds stress, and barely increases the spanwise stress, as depicted in Figure 8.9b and Figure 8.9g. This is to be expected, as the dynamic forcing term used in this work is intended to increase the production term of only the wall-normal stress and the turbulent shear stress.

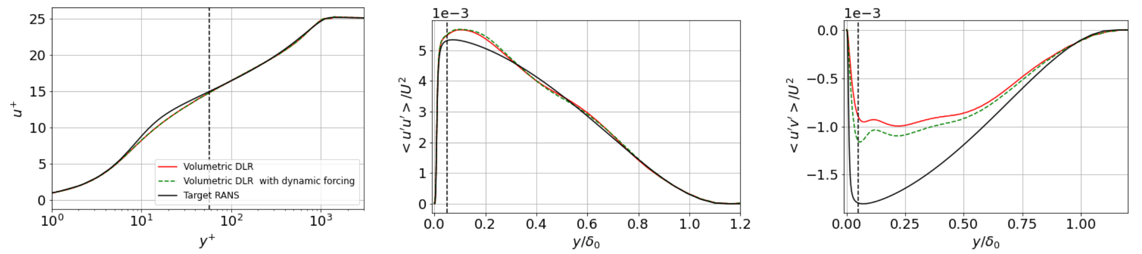

(a) u^+ **(b)** Resolved $<u'u'>$ **(c)** Resolved $<u'v'>$

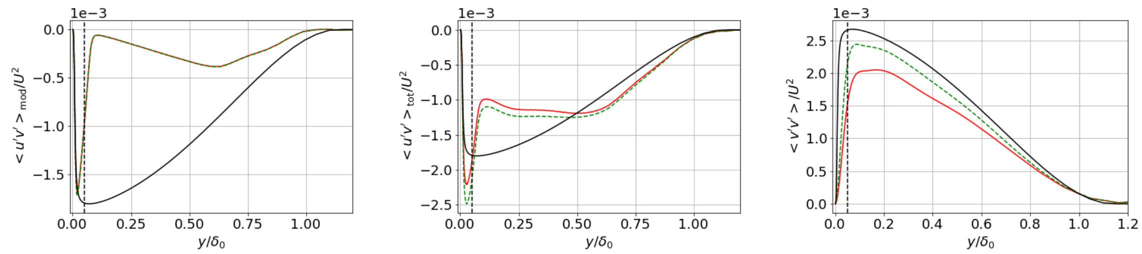

(d) Modeled $<u'v'>$ **(e)** Total $<u'v'>$ **(f)** Resolved $<v'v'>$

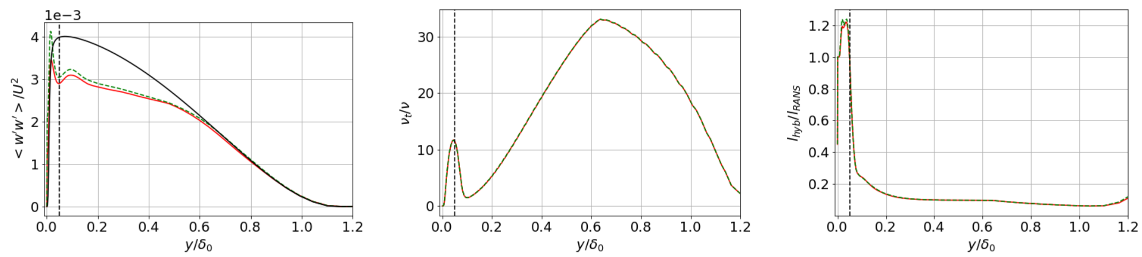

(g) Resolved $<w'w'>$ **(h)** ν_t **(i)** l_{hyb}/l_{RANS}

Figure 8.9: Results of the volumetric DLR source term combined with the dynamic forcing for the flat plate case at $x = 0.25$. The forcing region size $= 0.5\delta_0$

Figure 8.10 shows the results of the dynamic forcing at a distance of $3\delta_0$ downstream of the forcing region. Similar to the results at the forcing region, the velocity profile, streamwise and spanwise stress are barely influenced by the dynamic forcing, which is desirable. The wall-normal stress and the turbulent shear stress show larger amplitudes when dynamic forcing is used. So, the additional dynamic forcing term selectively increases the production of the intended resolved stresses, and its impact remains present downstream of the forcing region. This is exactly what was intended by using dynamic forcing, however, whether this behavior is beneficial or not remains unclear. The increase in the turbulent shear stress, caused by the dynamic forcing, appears to overestimate the target stress. However, recall that these target stresses are not very accurate since they are reconstructed from a RANS solution. More accurate reference data is needed to reach a clear conclusion.

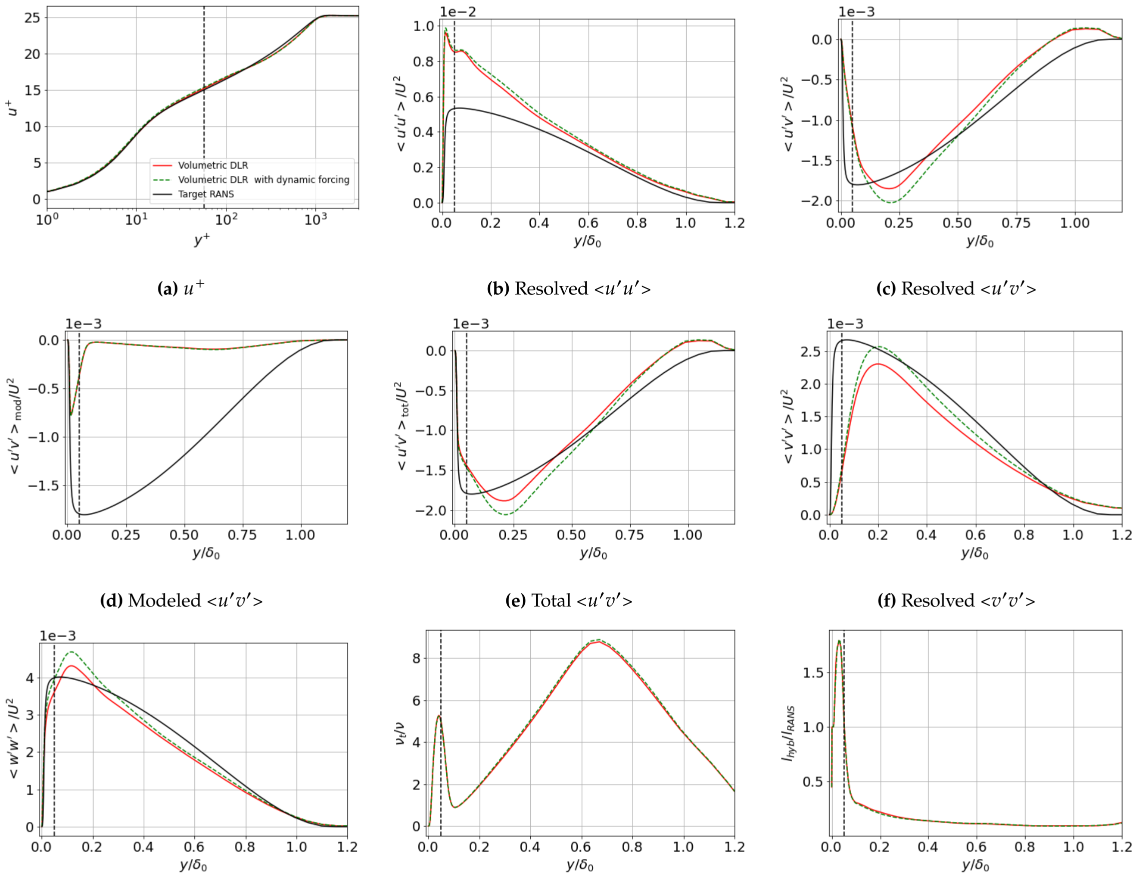

(a) u^+ **(b)** Resolved $<u'u'>$ **(c)** Resolved $<u'v'>$

(d) Modeled $<u'v'>$ **(e)** Total $<u'v'>$ **(f)** Resolved $<v'v'>$

(g) Resolved $<w'w'>$ **(h)** ν_t **(i)** l_{hyb}/l_{RANS}

Figure 8.10: Results of dynamic forcing for the flat plate case at $x = 3\delta_0$

The mean surface quantities are shown in Figure 8.11. Since the dynamic forcing term introduces additional synthetic velocities near the wall, it results in a spike in the skin friction shown in Figure 8.11a. This can possibly be mitigated by combining the dynamic forcing with the constrained forcing. however, this is not explored in this work due to time constraints. Furthermore, the pressure fluctuations result shows the typical peak with both computations, which can also be reduced using constrain forcing as discussed in subsection 8.3.1. Except for the increased peak value in C_f, the dynamic forcing has no negative impact on the mean surface quantities. .

In this chapter, two modifications to the synthetic turbulence forcing were proposed. The first is to limit the synthetic turbulence forcing to the LES region, which was referred to as the constrained forcing. This is a more physically sound approach, as the near-wall RANS region contains sufficient eddy viscosity to fully model the Reynolds stresses. Combining the constrained forcing with the DLR source term showed a better estimation of the total shear stress as a result of not superimposing resolved stress to already existing modeled stress. Furthermore, using the constrained forcing resulted in a

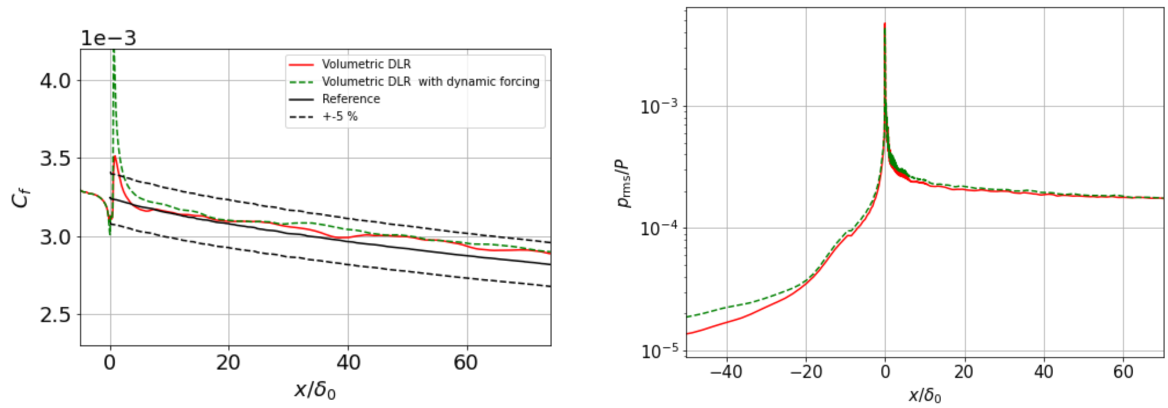

(a) C_f

(b) Pressure fluctuations

Figure 8.11: Skin friction coefficient and pressure fluctuations for the flat plate case using the volumetric DLR source term combined with dynamic forcing

significant decrease in the peak observed in both C_f and the pressure fluctuations at the interface.

The second modification is to use an additional forcing term that proportionally increases the production of selective resolved Reynolds stresses. To achieve this, the dynamic forcing of [32] was implemented in DLR-TAU and used together with the volumetric DLR source term. Indeed, the dynamic forcing increased the resolved turbulent shear stress and spanwise resolved stress, which otherwise suffered from a deficit in and downstream of the forcing region. However, it is not clear if such increase downstream of the forcing region is desirable. Due to the lack of accurate reference results downstream of the forcing region, no solid conclusions can be made. Furthermore, using dynamic forcing showed C_f peak, typically observed in interface forcing. This can be attributed to increasing the amplitudes of the synthetic velocities in the near-wall region. It is expected that such peak can be significantly reduced when combining dynamic forcing with constrained forcing. Finally, the interaction between the dynamic forcing and the DLR volumetric source term was not studied. It is important to investigate the effect each has on the other since both of them are applied simultaneously to momentum equations.

9

WMLES capabilities of $\sigma-$DDES and $\tilde{\Delta}_\omega$

In this chapter, $\sigma-$DDES and $\tilde{\Delta}_\omega$ are used as (embedded) wall-modeled LES (WMLES) methods. The analysis in this chapter can be divided into two aspects. The first concerns assessing the WMLES capabilities of combining $\sigma-$DDES with $\tilde{\Delta}_\omega$, reported in [21]. To evaluate this, $\sigma-$DDES and $\tilde{\Delta}_\omega$ are applied in the periodic channel flow test case, detailed in subsection 4.2.3. In this case, the shielding of DDES is maintained, similar to the original publication. The second aspect addresses the use of $\sigma-$DDES with $\tilde{\Delta}_\omega$ in an embedded WMLES manner. To achieve this, synthetic turbulence is injected and the shielding function is either deactivated completely or modified. This was evaluated using the flat plate and the rounded step test cases. The first and the second aspect are presented in section 9.1 and section 9.2, respectively.

9.1. WMLES capabilities of $\sigma-$DDES with $\tilde{\Delta}_\omega$

It is reported that combining $\sigma-$DDES with $\tilde{\Delta}_\omega$ has WMLES capabilities [21], however, no sufficient results were provided in the original publication. These WMLES capabilities were evaluated in this work using the periodic channel flow test case. To obtain an unsteady solution, the STG was used to inject synthetic turbulence for only half a domain flow-through (0.5 CTU) while using the WMLES branch of IDDES. Then, the injection of synthetic turbulence was deactivated, and the solution was computed using the WMLES branch of IDDES for another 30 CTU, in order to obtain a well-developed turbulent channel flow. This well-develop turbulent flow was used as the initial solution for the $\sigma-$DDES with $\tilde{\Delta}_\omega$. With this initial solution, $\sigma-$DDES with $\tilde{\Delta}_\omega$ were used to compute the solution for another 50 CTU and then the solution was time-averaged. The goal is to observe whether $\sigma-$DDES with $\tilde{\Delta}_\omega$ will drive the well-developed turbulent initial solution to a RANS-like flow, or it will maintain its unsteady nature.

A comparison between IDDES and $\sigma-$DDES with $\tilde{\Delta}_\omega$ is shown in Figure 9.1. First, the velocity profile shows no significant log-layer mismatch (LLM) with $\sigma-$DDES, an issue typical of DDES [18]. In fact, the velocity profile of $\sigma-$DDES is smoother than that of IDDES as shown in Figure 9.1a. This could be attributed to a less abrupt RANS-LES interface with $\sigma-$DDES, as shown in Figure 9.1i. Furthermore, $\sigma-$DDES shows some resolved turbulence content, but only in the outer part of the boundary layer. The lack of resolved turbulence content in the inner part of the boundary layer when using $\sigma-$DDES is a result of the large turbulent viscosity levels in that region, as shown in Figure 9.1h.

Figure 9.2 shows the Q-criterion for both the IDDES and $\sigma-$DDES computations. The impact of modeling the majority of the boundary layer in the case of $\sigma-$DDES is evident from the lack of turbulent structures close to the wall. In fact, with $\sigma-$DDES, turbulent structures can be seen only in the core of the channel. On the other hand, IDDES results show resolved turbulent structures even very close to the wall.

It is debatable whether or not the behavior obtained by $\sigma-$DDES is considered a WMLES capability. Even though the $\sigma-$DDES velocity profile did not exhibit large LLM that standard SA-DDES suffers from, it is hard to classify this as a WMLES capability given the absence of resolved turbulent content in the inner boundary layer. With $\sigma-$DDES, the RANS layer is much larger than with IDDES, so the accuracy of computations is more dependent on the RANS model. This could negatively affect the flow prediction of challenging flows (e.g. APG) that are sensitive to the accuracy of the solution in the near-wall region.

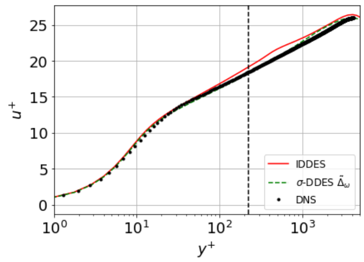

(a) u^+

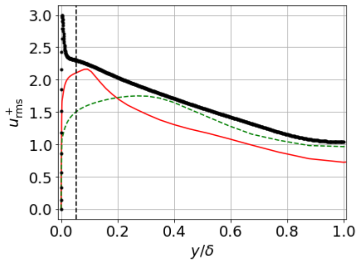

(b) Resolved $<u'u'>$

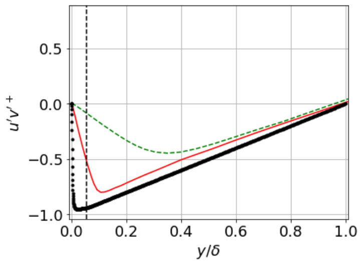

(c) Resolved $<u'v'>$

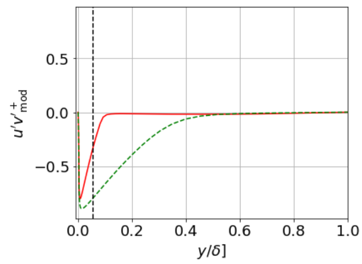

(d) Modeled $<u'v'>$

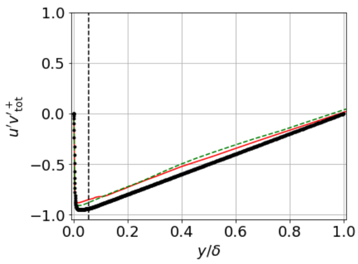

(e) Total $<u'v'>$

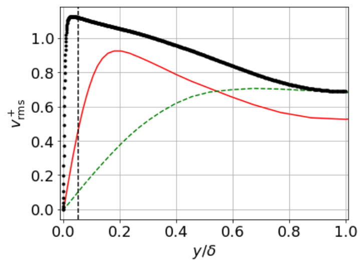

(f) Resolved $<v'v'>$

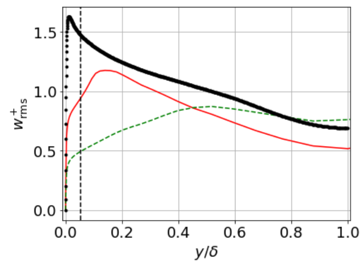

(g) Resolved $<w'w'>$

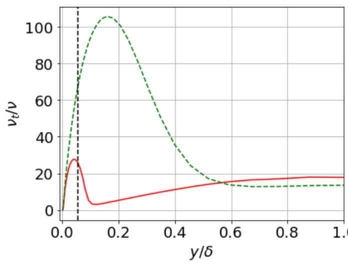

(h) ν_t

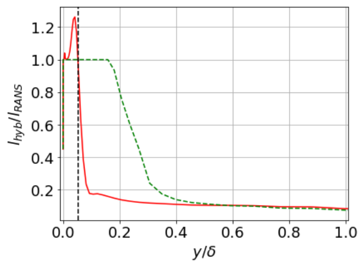

(i) l_{hyb}/l_{RANS}

Figure 9.1: Results comparing IDDES and σ−DDES with $\tilde{\Delta}_\omega$ for the channel flow case

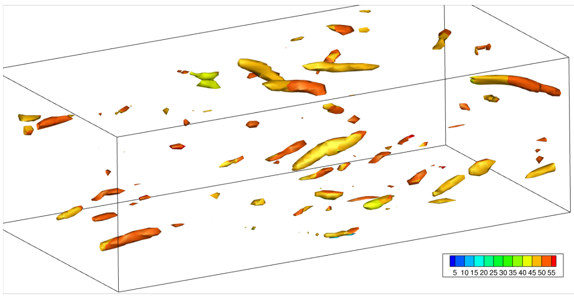

(a) σ−DDES with $\tilde{\Delta}_\omega$

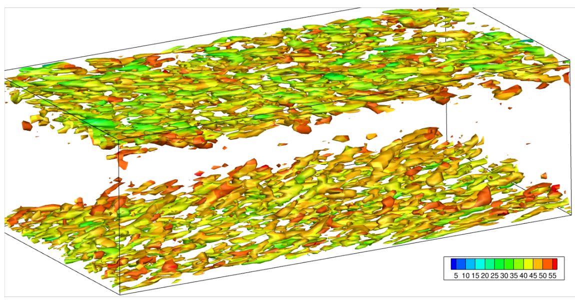

(b) WMLES branch of IDDES

Figure 9.2: Iso-surfaces of Q-criterion ($Q = 0.5U^2/\delta$), colored by the streamwise velocity for the channel flow

9.2. Embedded WMLES use of σ−DDES with $\tilde{\Delta}_\omega$

To further assess the WMLES capabilities of σ−DDES with $\tilde{\Delta}_\omega$, the combination is used along with synthetic turbulence in an embedded WMLES manner. To this end, two test cases were studied, namely, the flat plate test case and the rounded step test case. The hypothesis is that the development of the turbulence could be enhanced due to decreased levels of SGS viscosity (where appropriate), resulting in smaller adaptation lengths. This hypothesis is tested in this section.

First, the flat plate case is addressed. Given the behavior of the shielding function f_d in attached boundary layers, the shielding function was deactivated in one computation and the modified shielding function $f_{d_{\text{visc}}}$ was used in another computation. Recall, the modified shielding function $f_{d_{\text{visc}}}$ considers only the laminar viscosity ν and is defined in Equation 3.8. As shown in subsection 3.3.1, $f_{d_{\text{visc}}}$ is active only in the very near-wall region, so its shielding is barely existent. When the shielding function is deactivated, the switching from RANS to LES within the boundary layer solely depends on the grid. The original STG was used to provide synthetic turbulence at the interface. For a fair comparison, a standard IDDES computation was run with the original STG.

The results of using σ−DDES with $\tilde{\Delta}_\omega$ in an embedded WMLES manner for the flat plat are now discussed. The results of all computations at the interface were very similar and thus kept to the appendix Appendix A. The results at a distance of $3\delta_0$ downstream of the interface are of more interest and thus presented here in Figure 9.3. First, it was observed that the results of NTS-STG are in better agreement with the target RANS values, in terms of both the mean velocity profile and the resolved stresses. More importantly, using σ−DDES with $\tilde{\Delta}_\omega$ in an embedded WMLES setup resulted in large deviations in both the velocity profile and resolved stresses. Contrary to expectations, using σ−DDES with $\tilde{\Delta}_\omega$ in an embedded WMLES manner shows much less resolved turbulence compared to IDDES. Furthermore, σ−DDES with $\tilde{\Delta}_\omega$ exhibit significant deviations in the velocity profile with respect to the target RANS, as shown in Figure 9.3a.

The main issue with using σ−DDES with $\tilde{\Delta}_\omega$ as an embedded WMLES approach is the excessive reduction of eddy viscosity in the near-wall region. The eddy viscosity in the near-wall region of σ−DDES with $\tilde{\Delta}_\omega$ is lower than that produced by IDDES, as shown in Figure 9.3h. This is caused by a combination of insufficient near-wall shielding as a result of deactivating f_d or using $f_{d_{\text{visc}}}$, and the low turbulent viscosity levels produced by the σ model itself in such stable flow. A more appropriate near-wall shielding is that used by IDDES, where the length scale is deliberately increased near the RANS-LES interface in the boundary layer to avoid excessive reduction of modeled stresses. Otherwise, such excessive decrease in eddy viscosity, and hence decreased modeled stresses, typically leads to LLM.

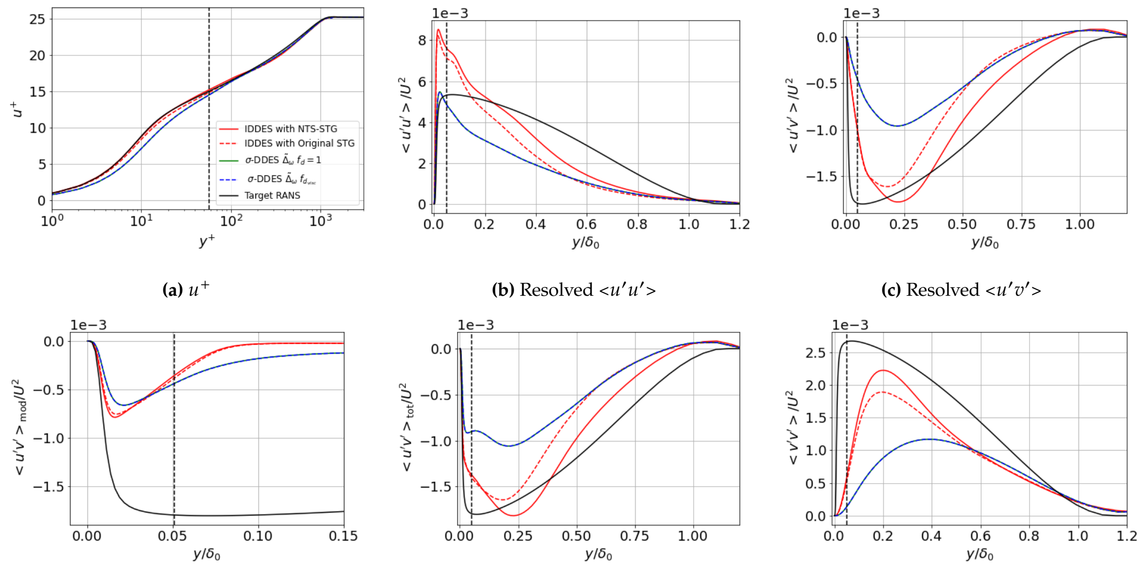

(a) u^+ **(b)** Resolved $<u'u'>$ **(c)** Resolved $<u'v'>$

(d) Modeled $<u'v'>$ **(e)** Total $<u'v'>$ **(f)** Resolved $<v'v'>$

Figure 9.3: Results of using σ-DDES with $\tilde{\Delta}_\omega$ in an embedded WMLES manner for the flat plate case at $x = 3\delta_0$

The mean surface quantities of these computations are shown in Figure 9.4. Figure 9.4a shows a significant drop in C_f downstream of the interface. This can be attributed to insufficient levels of eddy viscosity in the near-wall region, depicted in Figure 9.3h, and discussed in the previous paragraph.

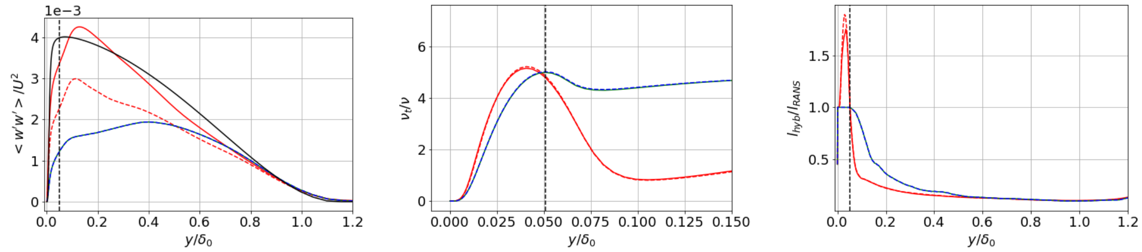

(g) Resolved $<w'w'>$ **(h)** ν_t **(i)** l_{hyb}/l_{RANS}

Figure 9.3: Results of using σ-DDES with $\tilde{\Delta}_{\omega}$ in an embedded WMLES manner for the flat plate case at $x = 3\delta_0$ (continued from previous page)

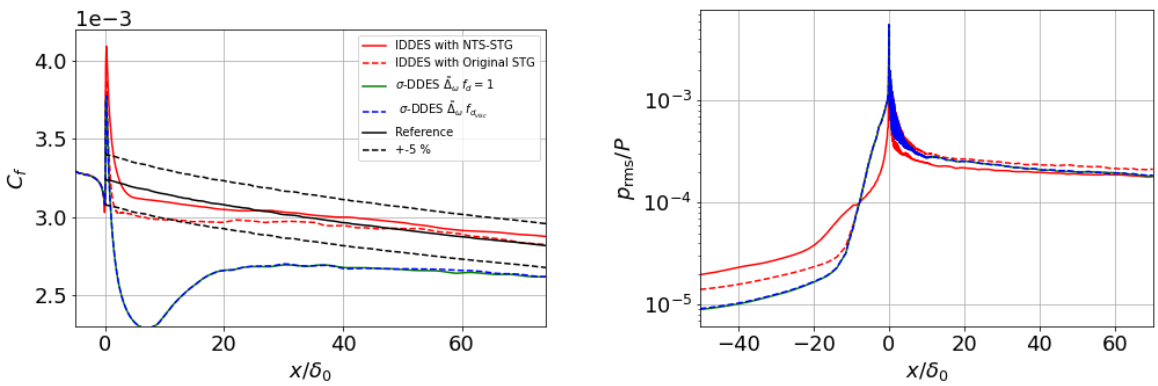

(a) C_f **(b)** Pressure fluctuations

Figure 9.4: Results of using σ-DDES with $\tilde{\Delta}_{\omega}$ in an embedded WMLES manner for the flat plate case at $x = 3\delta_0$

A similar analysis was performed using the rounded step case. Similar behavior to that encountered in the flat plate case is observed, as depicted in Figure 9.5. Using σ-DDES with $\tilde{\Delta}_{\omega}$ in an embedded WMLES manner does not accelerate the development of the synthetic turbulence into resolve one, but rather the opposite. It shows mostly lower resolved stress compared to IDDES, as shown in Figure 9.5d, Figure 9.5g, and Figure 9.5h. Furthermore, similar low levels of eddy viscosity are observed in the near-wall region when using σ-DDES with $\tilde{\Delta}_{\omega}$, as shown in Figure 9.6e.

The results of these computations in the separated flow region are shown in Figure 9.6. Using σ-DDES with $\tilde{\Delta}_{\omega}$ shows larger deviations from the reference LES data in terms of the velocity profiles and resolved stresses. Nevertheless, the results are comparable to those obtained with IDDES to a large extent. One can attribute the improved results of σ-DDES with $\tilde{\Delta}_{\omega}$ in the separated flow region to the correct turbulent viscosity levels, as shown in Figure 9.6e. It is evident that in the separated flow region, the near-wall region no longer suffers from the excessive decrease in turbulent viscosity experienced in the upstream region, as depicted in Figure 9.5e. This is because the eddy viscosity produced by the $\sigma-$ model is sufficiently large in the separated flow region, unlike the upstream attached flow region. Furthermore, since the flow is separated, the lack of sufficient shielding, experienced in the upstream region when deactivating f_d or using $f_{d_{\text{visc}}}$, is no longer a concern.

The friction and pressure coefficients are shown in Figure 9.7. A drop in C_f, similar to that experienced in the flat plat case, is present when using σ-DDES with $\tilde{\Delta}_{\omega}$. As discussed earlier, this is due to the insufficient turbulent viscosity in the near-wall region of the upstream attached boundary layer. However, in the downstream separated flow region, σ-DDES with $\tilde{\Delta}_{\omega}$ produce the appropriate levels of turbulent viscosity. As a result, the combined models produce results that are very comparable to those of IDDES (with NTS-STG). The pressure coefficient produced by σ-DDES with $\tilde{\Delta}_{\omega}$ is comparable to that resulting from IDDES.

In this chapter, the WMLES capabilities of σ-DDES with $\tilde{\Delta}_{\omega}$ were assessed. In the periodic channel test case, the combination did not show a significant LLM that is typical of DDES. However, σ-DDES

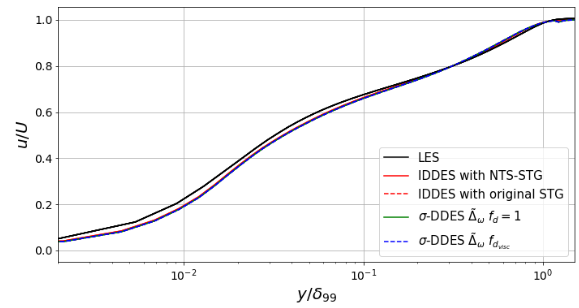

(a) u at the interface

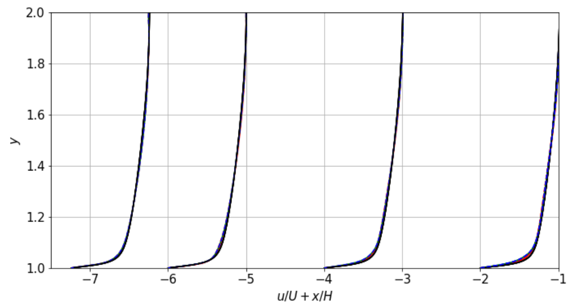

(b) u

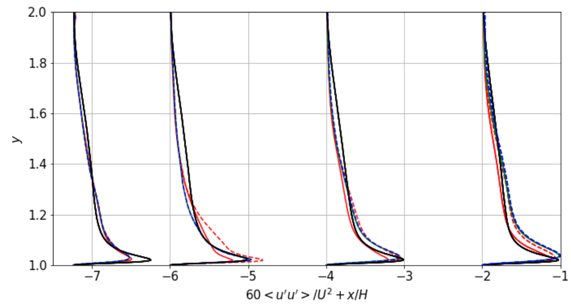

(c) Resolved $<u'u'>$

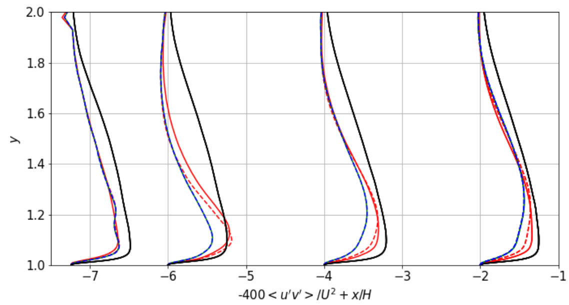

(d) Resolved $<u'v'>$

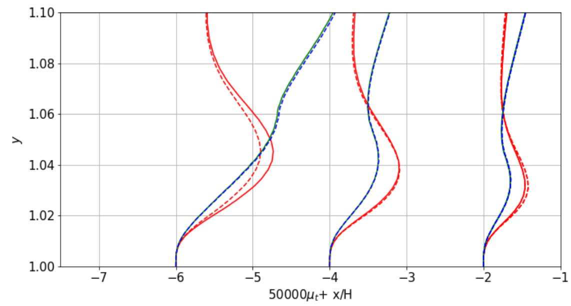

(e) ν_t (zoomed-in)

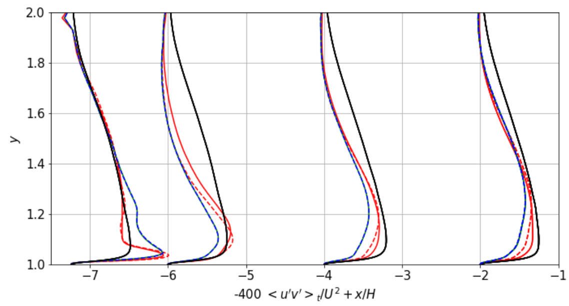

(f) Total $<u'v'>$

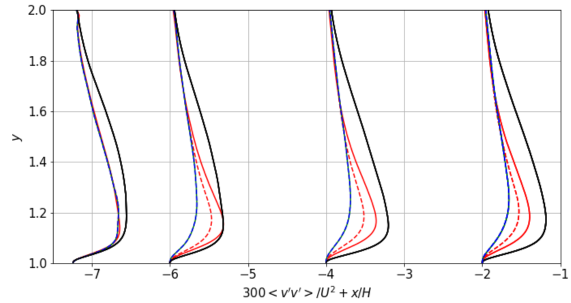

(g) Resolved $<v'v'>$

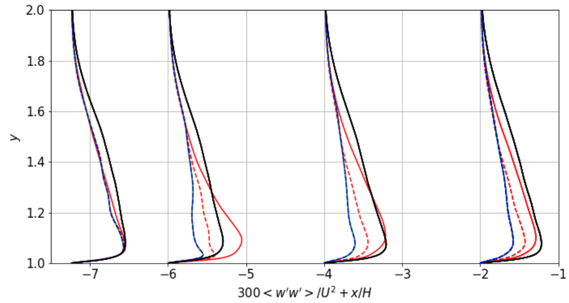

(h) Resolved $<w'w'>$

Figure 9.5: Results of using σ-DDES with $\tilde{\Delta}_\omega$ in an embedded WMLES manner for the rounded step

with $\tilde{\Delta}_\omega$ modeled the majority of the boundary layer, which results in coherent structures appearing only in the core of the channel. Regarding the use of σ-DDES with $\tilde{\Delta}_\omega$ in an embedded WMLES manner, it was found this use is troublesome. This is mainly due to excessively decreased levels of eddy viscosity in the near-wall region. This excess decrease in eddy viscosity is due to the insufficient shielding of the near-wall region as a result of deactivating the shielding function, combined with the low eddy

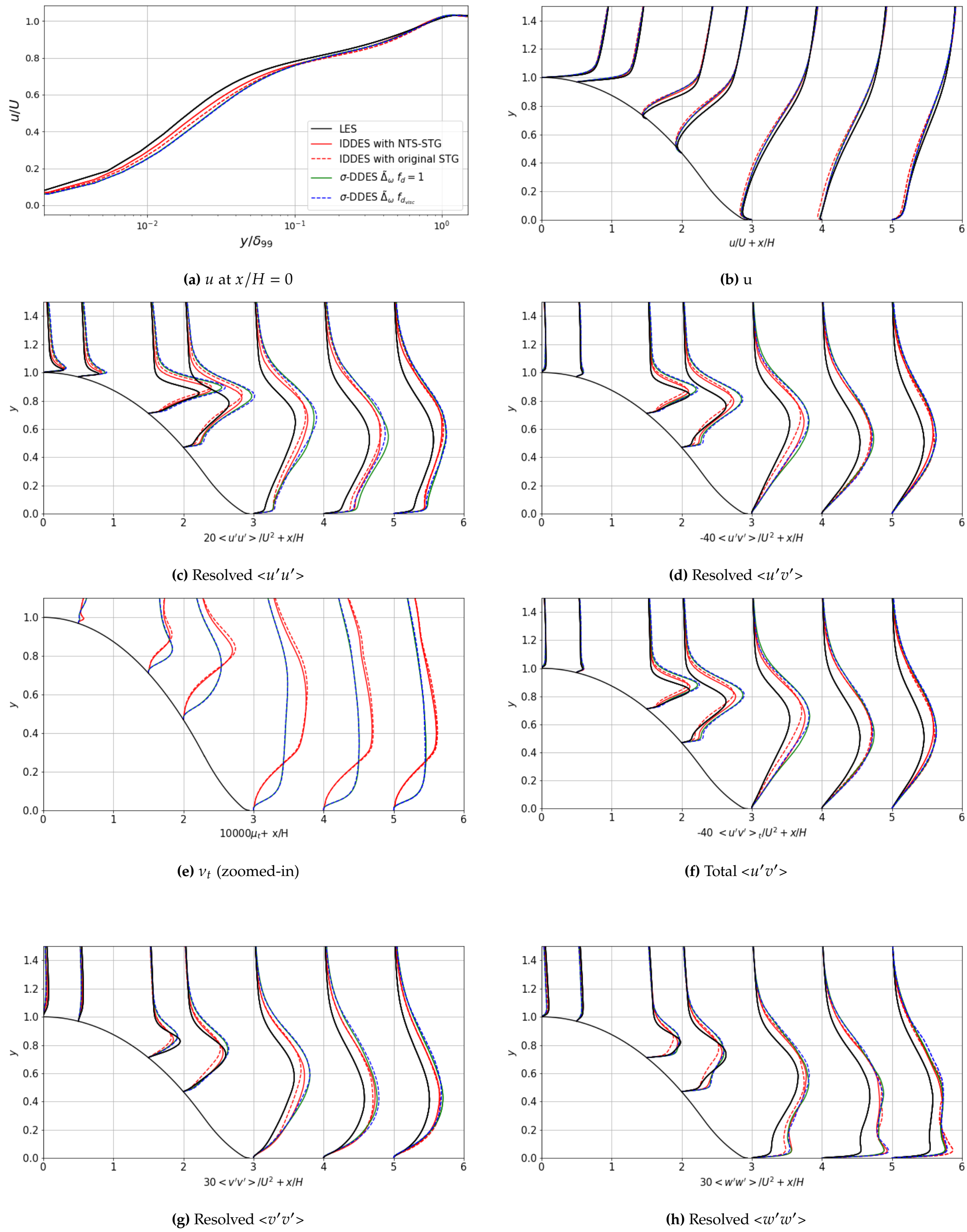

(a) u at $x/H = 0$

(b) u

(c) Resolved $<u'u'>$

(d) Resolved $<u'v'>$

(e) ν_t (zoomed-in)

(f) Total $<u'v'>$

(g) Resolved $<v'v'>$

(h) Resolved $<w'w'>$

Figure 9.6: Results of using σ-DDES with $\tilde{\Delta}_\omega$ in an embedded WMLES manner for the rounded step

viscosity levels produced by the σ-model.

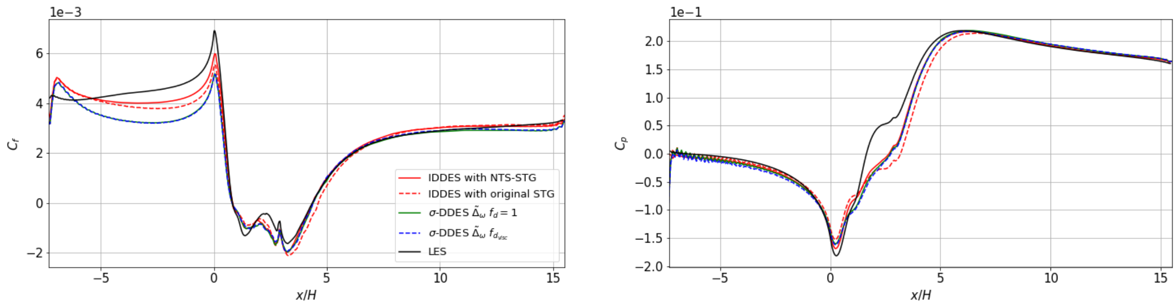

(a) C_f **(b)** C_p

Figure 9.7: Skin friction and pressure coefficient using σ-DDES with $\tilde{\Delta}_\omega$ in an embedded WMLES manner.

10
Conclusion and Recommendations

The grey area problem remains an extensively studied area of research in hybrid RANS-LES methods. In this thesis, zonal grey area mitigation approaches were evaluated, some of which were improved. The work on zonal methods focused on analyzing the quality of the synthetic turbulence and its forcing methods. In this work, the STG of [12] and a slightly modified variant, the NTS-STG of [13], were considered. Regarding the synthetic forcing methods, the DLR source term proposed by Probst [14] as well as the VSTG source term proposed by Shur et al. [15] were evaluated. The research activities followed a systemic step-wise approach, where the sources of error were identified and eliminated one at a time. This prevented accumulating different sources of error, and thus allowed for a fair assessment of each source of error.

Regarding synthetic turbulence, two important aspects of the synthetic turbulence generators, the STG and the NTS-STG, were studied. These are the macro-scale velocity and the cut-off frequency. It was found that using instantaneous macro-scale velocity leads to temporal decay in the quality of the synthetic turbulence, due to the lack of proper auto-correlation. On the other hand, using a mean macro-scale velocity ensures a consistent quality of synthetic turbulence that does not deteriorate with time. Furthermore, it was found that using the correct definition of the cut-off frequency improves the skin friction prediction, as a result of the correct mode amplitude distribution.

Secondly, an assessment of the STG input parameters that impact the statistics of the synthetic turbulence was performed. The first parameter is the set of random numbers used to determine the direction and phase shifts of various modes, while the second is the target Reynolds stresses, which can be either reconstructed from a RANS computation or provided by DNS or LES. It was found that the use of the selection procedures in [16] mitigates large bias errors that otherwise may arise if a random realization is used. The impact of such large bias errors is not limited to the forcing region, but can also have persistent effects downstream of the forcing region. Moreover, it was found that even when inaccurate RANS Reynolds stresses were used, the flow was still able to adapt to the correct Reynolds stress levels. However, this adaptation length can be significantly larger when compared to using more accurate target Reynolds stresses obtained from DNS or LES. The impact of these two factors on velocity profiles and skin friction was found to be minimal, as seen in the rounded step test case.

An assessment of different synthetic turbulence forcing strategies was carried out using the DLR source term and the VSTG source term, where the underlying RANS model, the use of an additional sink term to further decrease the eddy viscosity, and the size of the forcing region were varied. The DLR source term showed better agreement with the reference data in terms of the velocity profile, resolved stresses, and skin friction coefficient. However, it exhibited significantly larger spurious noise, indicated by a large peak in pressure fluctuations, as seen in the flat plate test case. Furthermore, the DLR interface forcing showed a peak in C_f at the interface, due to disturbed velocity gradients in the near wall region.

Motivated by these shortcomings, two modifications were proposed. The first is the constrained forcing, which aims to achieve a more accurate estimation of the total turbulent shear stress by avoiding superimposing resolved stresses to the already existing modeled stresses in the near-wall region. This was achieved by limiting the injection of the synthetic turbulence to the LES-treated region of the boundary layer. With the constrained forcing, a better estimation of the total shear stress was achieved.

Furthermore, using the constrained forcing significantly reduced the peak in both C_f and the pressure fluctuations. This is a result of not disturbing the velocity gradients in the near-wall region by not injecting synthetic turbulence in that region.

The second proposed modification aims at treating the deficit in some resolved stresses, observed in and downstream of the forcing region. To achieve this, the dynamic forcing of [32] was implemented in DLR-TAU and used as an additional source term together with the volumetric DLR source term. The use of dynamic forcing slightly increased the resolved turbulent shear stress and significantly increased the spanwise resolved stress, deceasing the deficit in both resolved stresses. It remains unclear whether the increase in these resolved stresses downstream of the forcing region is desirable. Due to the lack of accurate reference data downstream of the forcing region, this could not be concluded.

With the aforementioned work, a faster transition from RANS to LES in embedded WMLES methods was achieved. This resulted in a faster adaptation in terms of both the skin friction coefficient and the Reynolds stresses. Therefore, the presented work limited the negative impact associated with the grey area problem. As a result, this allows for a more accurate flow prediction in challenging separated flows at much lower computational cost compared to pure LES.

In addition, σ-DDES with $\tilde{\Delta}_\omega$ were used in an embedded WMLES manner together with synthetic turbulence. The premise was that the lower levels of turbulent viscosity produced by the $\sigma-$ model could facilitate the development of turbulence and hence decrease the adaptation lengths. This work revealed that this is not the case. The notion that merely decreasing the turbulent viscosity would result in shorter adaptation length has been proven flawed. Using σ-DDES with $\tilde{\Delta}_\omega$ in an embedded WMLES manner resulted in excessively decreased turbulent viscosity in the near-wall region. This has been shown to be problematic, as it makes the flow prone to the log-layer mismatch problem. As a result, a sudden decrease in C_f of approximately 25% was observed immediately downstream of the interface.

Recommendations and future work

Even though the selection procedures resulted in small bias errors with respect to the target Reynolds stresses, the skin friction coefficient is not considered when choosing the random number set. Therefore, there is no guarantee that the selected set will produce sufficiently accurate C_f. It is worth investigating criteria that take into account the skin friction coefficient.

Even though the dynamic forcing partially reduces the deficit in some resolved Reynolds stresses, it resulted in a large peak in C_f. Combining both dynamic forcing and constrained forcing could show improvement with regard to this issue. Furthermore, the interaction between the DLR source term and the dynamic forcing was not investigated. It is important to analyze such possible interactions to ensure that none of the source terms negatively affects the other. Lastly, it could be instructive to explore the dynamic forcing of [33] since its proportional controller is based on the turbulent shear stress, as opposed to the wall-normal stress used in [32]. As a result, the former is expected to better treat the deficit in the turbulent shear stress, which is arguably the most important Reynolds stresses component in the considered types of flow.

The use of σ-DDES with $\tilde{\Delta}_\omega$ in an embedded WMLES manner was shown to be troublesome. This is mainly due to an excessive decrease in eddy viscosity in the near-wall region. Using an alternative shielding function that ensures appropriate near-wall treatment could produce better results. The functions f_B and f_e that are used in the IDDES formulation are good candidates for such applications. This is because these functions ensure sufficient eddy velocity near the RANS-LES interface in the boundary layer by increasing the length scale in that region. This may prevent such excessive decrease in eddy viscosity in the near-wall RANS region.

References

[1] A. Probst and S. Melber-Wilkending. "Numerical and modeling investigations of the high-lift CRM configuration using hybrid RANS/LES". In: *AIAA AVIATION 2022 Forum*. DOI: 10.2514/6.2022-3590.

[2] P. R. Spalart. "Comments on the feasibility of LES for wings, and on a hybrid RANS/LES approach". In: *Proceedings of first AFOSR international conference on DNS/LES*. Greyden Press. 1997.

[3] M. L. Shur, P. R. Spalart, M. K. Strelets, and A. K. Travin. "An enhanced version of DES with rapid transition from RANS to LES in separated flows". In: *Flow, Turbulence and Combustion* 95.4 (2015), pp. 709–737. DOI: 10.1007/s10494-015-9618-0.

[4] C. Mockett et al. "Two non-zonal approaches to accelerate RANS to LES transition of free shear layers in DES". In: *Progress in hybrid RANS-LES modelling*. Springer, 2015, pp. 187–201.

[5] N. Chauvet, S. Deck, and L. Jacquin. "Zonal detached eddy simulation of a controlled propulsive jet". In: *AIAA Journal* 45.10 (2007), pp. 2458–2473. DOI: 10.2514/1.28562.

[6] S. Deck. "Recent improvements in the zonal detached eddy simulation (ZDES) formulation". In: *Theoretical and Computational Fluid Dynamics* 26.6 (2011), pp. 523–550. DOI: 10.1007/s00162-011-0240-z.

[7] F. Nicoud, H. B. Toda, O. Cabrit, S. Bose, and J. Lee. "Using singular values to build a subgrid-scale model for large eddy simulations". In: *Physics of Fluids* 23.8 (2011), p. 085106. DOI: 10.1063/1.3623274.

[8] S. Deck. "Recent improvements in the zonal detached eddy simulation (ZDES) formulation". In: *Theoretical and Computational Fluid Dynamics* 26 (2012), pp. 523–550.

[9] A. E. Perry and I. Marušić. "A wall-wake model for the turbulence structure of boundary layers. Part 1. Extension of the attached eddy hypothesis". In: *Journal of Fluid Mechanics* 298 (1995), pp. 361–388. DOI: 10.1017/S0022112095003351.

[10] A. Probst et al. "Evaluation of grey area mitigation tools within zonal and non-zonal RANS-LES approaches in flows with pressure induced separation". In: *International Journal of Heat and Fluid Flow* 68 (2017), pp. 237–247. ISSN: 0142-727X. DOI: https://doi.org/10.1016/j.ijheatfluidflow.2017.08.008. URL: https://www.sciencedirect.com/science/article/pii/S0142727X17302783.

[11] N. Jarrin, S. Benhamadouche, D. Laurence, and R. Prosser. "A synthetic-eddy-method for generating inflow conditions for large-eddy simulations". In: *International Journal of Heat and Fluid Flow* 27.4 (2006). Special Issue of The Fourth International Symposium on Turbulence and Shear Flow Phenomena - 2005, pp. 585–593. ISSN: 0142-727X. DOI: https://doi.org/10.1016/j.ijheatfluidflow.2006.02.006.

[12] D. Y. Adamian, M. K. Strelets, and A. K. Travin. "An efficient method of synthetic turbulence generation at LES inflow in zonal RANS–LES approaches to computation of turbulent flows". In: *Matematicheskoe modelirovanie* 23.7 (2011), pp. 3–19.

[13] M. L. Shur, P. R. Spalart, M. K. Strelets, and A. K. Travin. "Synthetic turbulence generators for RANS-LES interfaces in zonal simulations of aerodynamic and aeroacoustic problems". In: *Flow, turbulence and combustion* 93.1 (2014), pp. 63–92.

[14] A. Probst. "Implementation and assessment of the Synthetic-Eddy Method in an unstructured compressible flow solver". In: (2018), pp. 91–101.

[15] M. Shur et al. "Improved embedded approaches". In: *Go4Hybrid: Grey Area Mitigation for Hybrid RANS-LES Methods*. Springer, 2018, pp. 51–87.

[16] J. Patterson, R. Balin, and K. Jansen. "Assessing and improving the accuracy of synthetic turbulence generation". In: *Journal of Fluid Mechanics* 906 (2021).

[17] C. Mockett. *A comprehensive study of detached eddy simulation*. Univerlagtuberlin, 2009.

[18] P. R. Spalart, S. Deck, M. L. Shur, K. D. Squires, M. K. Strelets, and A. Travin. "A new version of detached-eddy simulation, resistant to ambiguous grid densities". In: *Theoretical and Computational Fluid Dynamics* 20.3 (2006), pp. 181–195. DOI: 10.1007/s00162-006-0015-0.

[19] M. L. Shur, P. R. Spalart, M. K. Strelets, and A. K. Travin. "A hybrid RANS-LES approach with delayed-DES and wall-modelled LES capabilities". In: *International journal of heat and fluid flow* 29.6 (2008), pp. 1638–1649.

[20] P. R. Spalart. "Detached-eddy simulation". In: *Annual Review of Fluid Mechanics* 41.1 (2009), pp. 181–202. DOI: 10.1146/annurev.fluid.010908.165130.

[21] M. Fuchs, C. Mockett, J. Sesterhenn, and F. Thiele. "Recent results with grey-area improved DDES for a wide range of flows". In: *Progress in Hybrid RANS-LES Modelling: Papers Contributed to the 6th Symposium on Hybrid RANS-LES Methods, 26-28 September 2016, Strasbourg, France 6*. Springer. 2018, pp. 195–206.

[22] A. Probst and P. Ströer. "Comparative Assessment of Synthetic Turbulence Methods in an Unstructured Compressible Flow Solver". In: *Progress in Hybrid RANS-LES Modelling*. Springer, 2020, pp. 193–202.

[23] R. Laraufie and S. Deck. "Assessment of Reynolds stresses tensor reconstruction methods for synthetic turbulent inflow conditions. Application to hybrid RANS/LES methods". In: *International journal of heat and fluid flow* 42 (2013), pp. 68–78.

[24] H. M. Nagib, K. A. Chauhan, and P. A. Monkewitz. "Approach to an asymptotic state for zero pressure gradient turbulent boundary layers". In: *Philosophical Transactions of the Royal Society A: Mathematical, Physical and Engineering Sciences* 365.1852 (2007), pp. 755–770.

[25] Y. Bentaleb, S. Lardeau, and M. A. Leschziner. "Large-eddy simulation of turbulent boundary layer separation from a rounded step". In: *Journal of Turbulence* 13 (2012), N4.

[26] C. Froh. "Implementierung und Erprobung einer Vortex-Methode für skalen-auflösende Simulationen mit dem DLR-TAU Code". In: *Diplomarbeit, TU Dresden* (2012).

[27] A. Lozano-Durán and J. Jiménez. "Effect of the computational domain on direct simulations of turbulent channels up to $Re_\tau = 4200$". In: *Physics of Fluids* 26.1 (2014), p. 011702.

[28] A. Probst, J. Löwe, S. Reuß, T. Knopp, and R. Kessler. "Scale-resolving simulations with a low-dissipation low-dispersion second-order scheme for unstructured flow solvers". In: *AIAA Journal* 54.10 (2016), pp. 2972–2987.

[29] D. Schwamborn, A. Gardner, H. von Geyr, A. Krumbein, H. Lu deke, and A. Sturmer. "Development of the TAU-Code for aerospace applications". In: (50th NAL International Conference on Aerospace Science and Technology 2008).

[30] J. Löwe, A. Probst, T. Knopp, and R. Kessler. "Low-dissipation low-dispersion second-order scheme for unstructured finite volume flow solvers". In: *AIAA Journal* 54.10 (2016), pp. 2961–2971.

[31] R. H. Kraichnan. "Diffusion by a random velocity field". In: *The physics of fluids* 13.1 (1970), pp. 22–31.

[32] R. Laraufie, S. Deck, and P. Sagaut. "A dynamic forcing method for unsteady turbulent inflow conditions". In: *Journal of Computational Physics* 230.23 (2011), pp. 8647–8663.

[33] A. Spille-Kohoff and H.-J. Kaltenbach. "Generation of turbulent inflow data with a prescribed shear-stress profile". In: (2001).

[34] M. Pamiès, P.-E. Weiss, E. Garnier, S. Deck, and P. Sagaut. "Generation of synthetic turbulent inflow data for large eddy simulation of spatially evolving wall-bounded flows". In: *Physics of fluids* 21.4 (2009), p. 045103.

A
Additional Results

Figure A.1 shows the results of the VSTG source term with different forcing region sizes for the flat plate case at $x = 1\delta_0$. The forcing region sizes are $1\delta_0$ and $2\delta_0$.

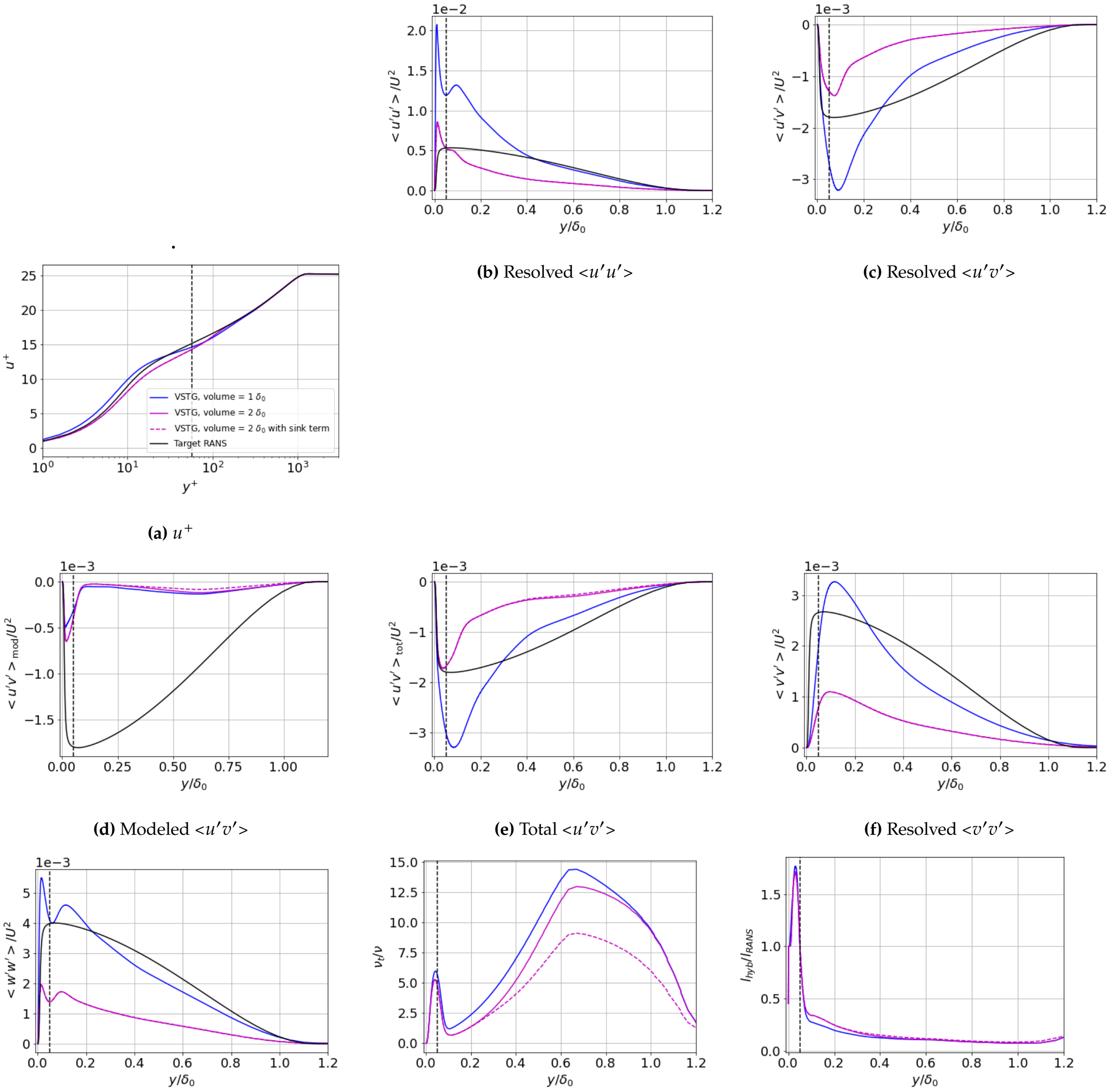

(a) u^+

(b) Resolved $<u'u'>$

(c) Resolved $<u'v'>$

(d) Modeled $<u'v'>$

(e) Total $<u'v'>$

(f) Resolved $<v'v'>$

(g) Resolved $<w'w'>$

(h) ν_t

(i) l_{hyb}/l_{RANS}

Figure A.1: Results of the VSTG forcing with different forcing region sizes for the flat plate case at $x = 1\delta_0$. The forcing region sizes are $1\delta_0$ and $2\delta_0$.

Figure A.2 shows the results of using σ-DDES with $\tilde{\Delta}_\omega$ in an embedded WMLES manner for the flat plate case at the interface ($x = 0$).

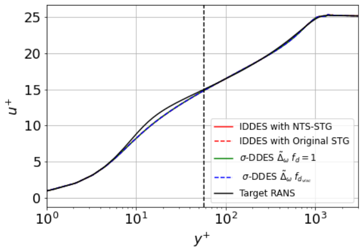

(a) u^+

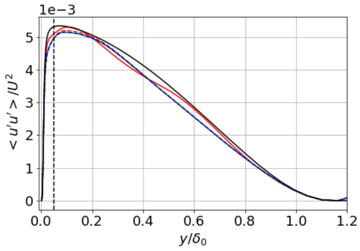

(b) Resolved $<u'u'>$

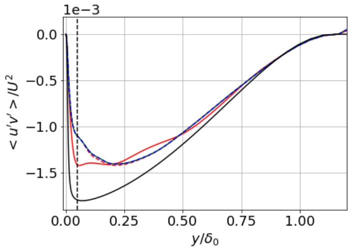

(c) Resolved $<u'v'>$

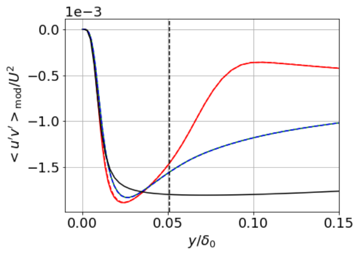

(d) Modeled $<u'v'>$

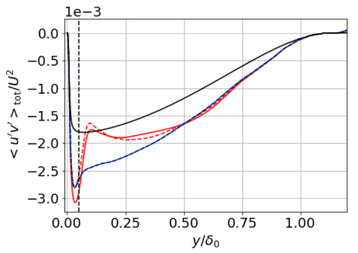

(e) Total $<u'v'>$

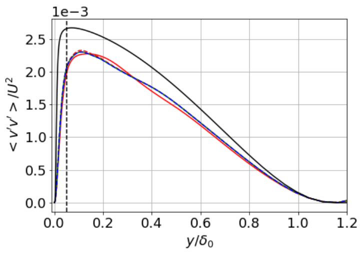

(f) Resolved $<v'v'>$

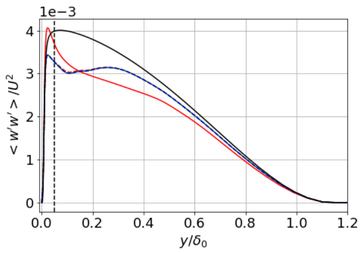

(g) Resolved $<w'w'>$

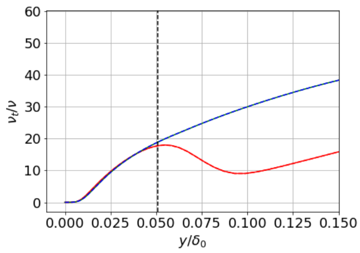

(h) ν_t

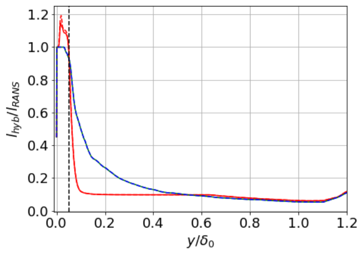

(i) l_{hyb}/l_{RANS}

Figure A.2: Results of using σ-DDES with $\tilde{\Delta}_\omega$ in an embedded WMLES manner for the flat plate case at the interface ($x = 0$)